NNT : 2016SACLE057

THESE DE DOCTORAT
DE
L'UNIVERSITE PARIS-SACLAY
PREPAREE A
L'UNIVERSITE EVRY VAL D'ESSONNE

ECOLE DOCTORALE N° 571
2MIB Sciences chimiques : molécules, matériaux, instrumentation et biosystèmes

Spécialité de doctorat : Chimie

Par

M. Sacha ABADIE

Vibrational excitation of molecules in the gas phase or embedded in matrices by *ab initio* molecular dynamics

Thèse présentée et soutenue à Evry, le 14 Décembre 2016 :

Composition du Jury :

M. Grégoire Gilles	Directeur de recherche à l'Université d'Orsay Paris Sud	Président
Mme. Sulpizi Marialore	Professeur à l'Université de Mainz	Rapporteure
M. Borgis Daniel	Directeur de recherche à l'Ecole Normale Supérieure	Rapporteur
Mme. Ingrosso Francesca	Maitre de conférences à l'Université de Lorraine	Examinatrice
Mme. Gaigeot Marie-Pierre	Fonction et établissement d'exercice	Directeur de thèse
M. Spezia Riccardo	Chargé de recherche à l'Université d'Evry	Co-directeur de thèse

Contents

Chapter 1

Introduction

Vibrational spectroscopy (Infrared and Raman) has been recognized for long as a fundamental tool for the characterization and understanding of the structure and dynamics of molecules isolated and in their environment. The typical way is to do static harmonic calculation with geometry optimisation, and from the Hessian matrix calculate the vibrational harmonic frequencies. Nevertheless in the case of solvation, or low frequency modes which are highly anharmonic, the static picture is not usually sufficient. Molecular dynamics (MD) simulations are a natural way to calculate vibrational spectra, including anharmonicities and vibrational couplings. Within the past two decade, DFT-based MD were successfully applied to floppy peptides [1], to ionic clusters [2] in the gas phase at finite temperatures, to solutes immersed in liquids [3], or to solid-liquid [4] and liquid-air [5, 6] interfaces, to name a few. The method is especially crucial in the gas phase of interest in the investigations achieved in my PhD.

In this context, we perform classical trajectories (i.e. classical nuclei) within the electronic DFT framework, which are computationally feasible for polyatomic systems composed by tens/hundreds of atoms (typically for systems in the gas phase, liquid phase, solids and interfaces between solids and liquids). On the other hand, a complete quantum treatment (i.e. quantum nuclei) is often impractical beyond 5-10 atoms. However, real systems follow quantum mechanics and classical mechanics, by construction, fails to describe quantum effects such as tunneling, non-adiabatic potential (i.e. surface crossings), and conservation of zero-point energy (ZPE) in the vibrational modes [7, 8].

Various studies have pointed out that ZPE can be a source in particular of serious error

in simulations of realistic systems. Quantum mechanically each internal molecular mode must contain an amount of energy at least equal to its ZPE, but classical mechanics may allow vibrational energy to flow freely between all or a subset of the modes and, hence, does not preserve any ZPE constraint [7]. This is of course an error inherent in classical mechanics. Consequently, no matter how accurately one can assign the ZPE to each normal mode of a molecule initially, after a certain number of steps the energies in these modes may fluctuate. The energy fluctuation between modes for a multimode Hamiltonian is caused by the mode-mode coupling. If there was only one mode in the Hamiltonian, then the mode energy would be conserved. In the case of separable (uncoupled) modes, the energies for these modes would be conserved as well. Any coupling terms between the modes in the Hamiltonian cause energy transfer between them. Without any control of the coupling term, it is possible for one mode to transfer its energy to other modes and to loose energy less than its ZPE [8]. Independently, Bowman and co-workers [9] and Miller and co-workers [10] proposed methods to constrain the ZPE by changing the sign of the momentum when the energy of any mode reaches the ZPE. This method did prevent energy from going below the ZPE, however since the momentum change occurs instantaneously, it is equivalent to an infinite impulse that is too abrupt, and can cause discontinuity in the classical correlation functions that we need to calculate for spectroscopy. Another method has been proposed by Bowman and co-workers [11] to constrain the ZPE by smoothly eliminating the coupling terms in the Hamiltonian as the energy of any mode falls below a specified value. These can again be problematic in our special context of vibrational spectroscopy and time-dependent correlation functions.

In a simple picture the ZPE leakage means that the initial ZPE provided in the vibrational modes of the investigated system might not be staying as such. In other words, we start a trajectory with the proper amount of energy in the vibrational modes of the molecular system, but as the trajectory is accumulated with classical nuclei afterwards, there is no warranty that this amount of energy will stay within the vibrational modes. In particular, it seems well-recognized that there might be a leakage of energy from high energy modes (typically N-H or O-H stretchings in the 3000-4000 cm^{-1} domain) towards low energy modes (typically below 1000 cm^{-1}), presumably most of the time towards inter-molecular modes. Some high-frequency modes thus loose energy while low-frequency modes gain energy. This is an issue we will face and investigate in our systems of interest.
Although the purpose of my thesis is not to deal with Zero Point Energy leakage, we will discuss it when presenting our results, and we will see how it might affect our conclusions.

What my PhD is focused on is the vibrational excitation of one given molecule, and the subsequent dynamics that occurs. The absorption of a photon in the infrared region with the proper wavelength excites a molecule vibrationally. This can initiate conformational isomerization or chemical reactions especially of gas phase molecules. Once deposited into the initially excited vibrational states, the radiation energy is transferred to other modes by intramolecular vibrational redistribution (IVR, if the molecule is in the gas phase) and the initially vibrationally excited molecule can relax back to its vibrational ground-state or can relax to another conformer which isomerization pathway has been energetically (and entropically) opened through the initial energy absorption. Of course, if the excited molecule is surrounded by other molecules, e.g. in a gas phase complex or surrounded by solvent as in liquids or in matrices, the intramolecular vibrational redistribution is complemented by intermolecular vibrational redistribution. Classical trajectory simulations are widely used [12] to study a wide variety of chemical processes including unimolecular [13], bimolecular reactions [14], intramolecular vibrational energy redistribution (IVR) [15, 16]. Pathways for intramolecular and intermolecular vibrational energy redistribution may be investigated [17, 18]. The control of chemical reactions or intramolecular processes by activating specific bonds/vibrational modes in a molecule have been studied for years by Bowman *et al.* [8, 11, 19, 20, 21, 22, 23]. My work has therefore focused on developing and assessing two ways of putting energy within chosen/given vibrational modes: a purely classical method and a quantum method (Wigner excitation). Then, we run classical molecular dynamics (for the nuclei) in the framework of the electronic DFT representation for the calculations of the forces applying to the nuclei. From these trajectories, we want to follow in time the processes of redistribution of the energy, especially following the quantum number of each mode of the system with time. This is a challenge, as we proceed with classical nuclei for which such quantum numbers do not exist by construction. We have developed a method base on VDOS (Vibrational Density of States) to allow us to define such quantum numbers and follow their evolution with time. We will see that the issue of ZPE leakage mentioned earlier will be present when we analyse such data. So, in this thesis, we want to know if we can selectively excite a vibrational mode (or combined modes) in a molecule inducing a chemical process (for instance isomerisation) and follow the dynamics of de-excitation of this mode by intra/inter vibrational relaxation (IVR).

During this thesis, the introduction of vibrational excitation in normal modes for two different prototypical examples has been studied: in condensed phase illustrated with a molecule of Formic Acid (FA) embedded in an argon matrix and in gas phase illustrated with the

$(Cl^{-}...NMA)Ar$ cluster. In both cases, we are interested in the "correct" preparation of initial conditions for DFT-MD dynamics (classical nuclei), and in following the evolution with time of the energy in the normal modes of the molecules illustrated by the evolution of the quantum number n_i of given normal modes.

The manuscript of the thesis is organized as follows :

- chapter 2: basis of the theoretical methods used (DFT and VDOS);
- chapter 3: presentation of the normal mode sampling of initial conditions;
- chapter 4: description of the theoretical methods to follow quantum number evolution;
- chapter 5: study of vibrational dynamics of Formic Acid embedded in an argon matrix;
- chapter 6: study of vibrational dynamics of $(Cl^{-}...NMA)Ar$ clusters.

Chapter 2

DFT-based Molecular Dynamics

2.1 General quantum mechanics for chemical systems

In physical chemistry, two different approaches can be used in order to describe the time evolution of a system, and the selection of one or another is based on the size of the system and on the properties of interest: classical mechanics is generally used for large systems, while quantum mechanics is preferred for smaller systems, instead. Classical mechanics is based on the resolution of the Newton equation of motion, that connects the acceleration, a, the mass m and the forces $\mathbf{F}$ acting over a particle:

$$\mathbf{F} = m\mathbf{a} \tag{2.1}$$

On the other hand, time dependent Schrödinger equation (TDSE) must be solved to have the time evolution of the system under study. The TDSE is

$$\boxed{\hat{H}\Psi(\mathbf{r},t) = i\hbar\frac{\partial}{\partial t}\Psi(\mathbf{r},t)} \tag{2.2}$$

where $\mathbf{r}$, corresponds to the coordinates of the particles, t is the time, $\hbar$ is Planck constant divided by 2π, and $\hat{H}$ is the Hamiltonian operator defined as

$$\hat{H} = \hat{T} + \hat{V} \tag{2.3}$$

where $\hat{T}$ is the kinetic energy operator that in quantum mechanics is

$$\hat{T} = -\frac{\hbar^2}{2m}\nabla^2 \tag{2.4}$$

where

$$\nabla^2 = \left(\frac{\partial^2}{\partial x_i^2} + \frac{\partial^2}{\partial y_i^2} + \frac{\partial^2}{\partial z_i^2}\right) \tag{2.5}$$

and $\hat{V}$ is the potential energy operator, that in its general formulation depends on the coordinates, $\mathbf{r}$, and the time t:

$$\hat{V} = V(\mathbf{r}, t) \tag{2.6}$$

If $\hat{H}$ is time independent, i.e. $\hat{V} = V(\mathbf{r})$, $\Psi(\mathbf{r}, t)$ can be factorized as

$$\Psi(\mathbf{r}, t) = \psi(\mathbf{r})\chi(t) \tag{2.7}$$

Where $\psi(\mathbf{r})$ depends only on positions and $\chi(t)$ has the time evolution. Thus, the Time Dependent Schrödinger Equation can be splitted into two equations:

$$i\hbar\frac{d\chi}{dt} = E\chi \tag{2.8}$$

and

$$\boxed{\hat{H}\psi = E\psi} \tag{2.9}$$

This last equation is the Time-independent Schrödinger equation(TISE). In the following we will consider a system composed of N electrons and N_n nuclei as illustrated in figure 2.1.

2.2 Born-Oppenheimer approximation

In a molecular system, there are variables changing fast and others changing slowly, which makes us intuitively think that the behavior of fast variables may be not significatively influenced by the velocity in the change of the slow ones. This decoupling between fast and slow

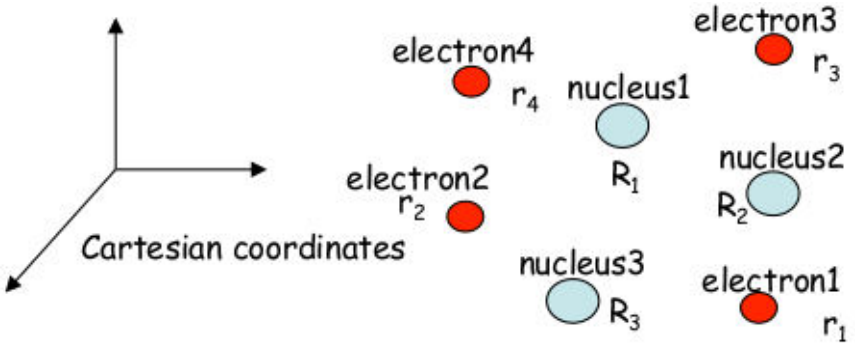

Figure 2.1: Schematic representation of the system composed of N electrons ($\vec{r_i}$) and N_n nuclei ($\vec{R_i}$)

.

variables is at the basis of the Born-Oppenheimer approximation (BOA).[24] Since the nuclear mass is at least 1,840 times bigger than the electron mass, the velocity of the electron is about 1,000 times the velocity of the nuclei. As such, it is convenient to decouple these two motions. The decoupling of nuclei velocities from electrons velocities allows to address the resolution in the following way: The dynamical evolution of the nuclear system is restricted to a single electronic potential energy surface (PES). The nuclei are "clamped" or fixed, and for them, integration of the classical equations of motion is done, advancing them by a small time increment $\triangle$t to a new configuration. Repeating the process results in the dynamical evolution of the system on the so-called Born-Oppenheimer PES. Then, the motion of the electrons in the fixed nuclear environment is determined by TISE. The resulting electron distribution causes a field acting on the nuclei, so the nuclei motion is governed by the interaction potential energy between the electrons and the nuclei. For stable molecules, the equilibrium positions of the nuclei are those in which the forces over each nucleus due to the total field are zero under real conditions. The nuclei will not remain in their equilibrium positions and this fact will cause the occurrence of restoring forces which linearly depends, at a first approximation, on the individual nuclear displacements. In classical mechanics, a restoring linear force causes an harmonic oscillation in the case of a simple particle. For a polyatomic molecule, the motion of the nuclei under the influence of the restoring forces can be described in terms of simultaneous normal vibrations. The quantum solution of this problem consists in the independent quantization of each normal mode. The BOA has been fundamental to calculations in molec-

ular spectroscopy and molecular dynamics since the early days of quantum mechanics. This is despite well-established fact that it is not valid in particular cases like the conical intersections that give rise to strong nonadiabatic effects caused by singular nonadiabatic coupling terms[25].
In a molecular system the total Hamiltonian is

$$\begin{aligned} \hat{H} &= \hat{K}_n + \hat{K}_e + \hat{V}_{en} + \hat{V}_{nn} + \hat{V}_{en} \\ &= \hat{K}_n + \hat{H}_e + (\hat{V}_{nn}) \end{aligned} \tag{2.10}$$

Where $\hat{K}_n$ is the kinetic energy operator of the nuclei, $\hat{K}_e$ is the kinetic energy operator of the electrons, $\hat{V}_{en}$ is the electron-nucleus interaction, $\hat{V}_{nn}$ is the nuclei-nuclei interaction and $\hat{V}_{ee}$ is the potential repulsion between electrons. $\hat{H}_e = \hat{K}_e + \hat{V}_{en} + \hat{V}_{en}$ is the "electronic hamiltonian".

In practice, when the BOA holds, one can solve the TISE for the electronic part described by $\hat{H}_e$, and use the Newton equations of motion for the nuclei. Thus, the problem for a molecular system is splitted into two parts [26]:

$$\begin{cases} \text{for the electrons} & \hat{H}_e\psi_0 = E_0\psi_0 \\ \text{for the nuclei} & -\nabla_i \min_{\Psi 0}\{\langle\Psi_0|\hat{H}_e|\Psi_0\rangle\} = M_I \frac{\partial^2}{\partial t^2}\mathbf{R}_I(t). \end{cases} \tag{2.11}$$

The zero subscripts in the electronic equation represent the ground state and $\hat{H}_e$ is the electronic Hamiltonian that we will discuss in details in the next section. On the other hand, in the equation for the nuclear motion, M_I is the mass of the I nucleus, $\frac{\partial^2}{\partial t^2}\mathbf{R}_I(t)$ is the second derivative of the I position $\mathbf{R}$.

2.3 Principles of Density Functional Therory

One ingenious solution to the solution of the electronic structure problem is represented by Density Functional Theory (DFT) ([27, 28]). DFT has nowdays become the most used approach for the description of the electronic structure properties of materials thanks to a favorable compromise between computational cost and accuracy. DFT has his foundation in

the famous Hohenberg-Kohn (HK) theorems that assume that the external potential V_{ext} is univocally determined by the electronic density, besides a trivial additive constant. In DFT, one replaces the $''N''$-electron wave function $\Psi(\vec{r}_1, \vec{r}_2, \cdots \vec{r}_N)$ and the associated Schrödinger equation by a simpler electron density, $\rho(\vec{r})$. Calling N the number of electrons, we have the following expression for the electron density:

$$\rho(\vec{r}_1) = N \int \cdots \int_2^N |\Psi|^2 \, d\vec{r}_1 d\vec{r}_2 \cdots d\vec{r}_N \tag{2.12}$$

where

$$\int \rho(\vec{r}) d\vec{r} = N \tag{2.13}$$

The orthonormalisation of the wavefunction provides:

$$\int d\vec{r}_1 d\vec{r}_2 \cdots d\vec{r}_N \, |\Psi(\vec{r}_1, \vec{r}_2, \cdots, \vec{r}_N)|^2 = 1 \tag{2.14}$$

The Schrödinger equation has to be rewritten in terms of the density $\rho(\vec{r})$ and once this is done the total energy of the system becomes a **functional** $E[\rho]$ of the density. The total energy of $''N''$-electron system now reads as:

$$E[\rho] = \int d^3\vec{r} \rho(\vec{r}) V_{ext}(\vec{r}) + F_{HK}[\rho] \tag{2.15}$$

with

$$F_{HK}[\rho] = T[\rho] + V_{ee}[\rho] \tag{2.16}$$

$$T[\rho] = \langle \Psi[\rho] | \hat{T} | \Psi[\rho] \rangle \tag{2.17}$$

$$V_{ee}[\rho] = \langle \Psi[\rho] | \hat{V}_{ee} | \Psi[\rho] \rangle \tag{2.18}$$

Unfortunately $F_{HK}[\rho]$ is not known and one has to make approximations for it. The problem arises from V_{ee} term and the transition from the wavefunction-based expression of V_{ee} to the density-based expression. The calculation of the electron-electron V_{ee} interaction indeed leads to two separate terms:

$$\begin{aligned} V_{ee} &= \frac{1}{2} \sum_i^N \sum_{j \neq i}^N \langle \Psi | \frac{1}{|\vec{r}_i - \vec{r}_j|} | \Psi \rangle \\ &= \frac{1}{2} \int \int \frac{\rho(\vec{r}) \rho(\vec{r}')}{|\vec{r} - \vec{r}'|} d\vec{r} d\vec{r}' + \frac{1}{2} \int \int \frac{\rho(\vec{r}) \rho(\vec{r}')}{|\vec{r} - \vec{r}'|} \left[g\left(\vec{r}, \vec{r}'\right) - 1 \right] d\vec{r} d\vec{r}' \end{aligned} \tag{2.19}$$

The first term corresponds to the classical electrostatic interaction energy, also called "Hartree term". The second term is the **exchange-correlation** energy term. $g(\vec{r},\vec{r}')$ is a two-body direct correlation function that takes into account the fact that the presence of an electron at $\vec{r}$ discourages a second electron from being located at a position $\vec{r}'$ too close to $\vec{r}$. Because of the Coulomb repulsion, this means that the probability of finding two electrons in the same region is reduced with respect to the probability of finding them at infinite distance. The exact expression of this second term is unknown for inhomogeneous electron gas, i.e all systems we are interested in. Several approximations have been devised in order to go beyond the homogeneous electron gas limit: this is where DFT starts to be "non exact". Taking into account this result, we can now write:

$$E[\rho] = T[\rho] + \int d^3\vec{r}\,\rho(\vec{r})V_{ext}(\vec{r}) + \int\int \frac{\rho(\vec{r})\rho(\vec{r}')}{|\vec{r}-\vec{r}'|}d\vec{r}d\vec{p}' + E_{xc}[\rho] \tag{2.20}$$

where one recognizes the kinetic energy functional, the external interaction energy functional, the classical Coulomb/Hartree energy functional, and the exchange-correlation functional (where we have summarized the seconnd term in eq. 2.19 into one “unknown term” called $E_{xc}[\rho]$ for exchange-correlation).

Exchange-correlation functionals

The simplest way of treating exchange and correlation in the Kohn-Sham formalism is to approximate the real system by an homogeneous electron gas. This allows the definition of the exchange-correlation energy functional per electron E_{xc}, such that:

$$E_{xc}^{LDA}[\rho] = \int \rho(\vec{r})\epsilon_{xc}(\rho)d\vec{r} \tag{2.21}$$

where $E_{xc}^{LDA}[\rho]$ corresponds to the Exchange-Correlation (XC) functional in the Local Density Approximation (LDA). The XC energy functional is further decomposed for convenience into exchange $E_x[\rho]$ and correlation $E_c[\rho]$ contributions: $E_{xc}[\rho] = E_x[\rho] + E_c[\rho]$. Considering only closed-shell systems, which will be the case almost always throughout this chapter (and our applications), the exchange part is known from Dirac's work as:

$$E_x^{LDA}[\rho] = -\frac{3}{4}\left(\frac{3}{\pi}\right)^{1/3}\int \rho(\vec{r})^{4/3}d\vec{r} \tag{2.22}$$

Only expressions for the exchange density are known exactly, leading to numerous different approximations for ϵ_c. To that end, analytic functions are fitted and an example is given in equations below:

$$\begin{aligned} e_c^{hom}[\rho] &= \frac{\gamma_c}{1+\beta_1\sqrt{r_s}+\beta_2 r_s},\ r_s > 1 \\ e_c^{hom}[\rho] &= Alnr_s + B + Cr_s lnr_s + Dr_s,\ r_s \leq 1 \\ r_s &= \left(\frac{3}{4\pi\rho}\right)^{1/3} \end{aligned} \tag{2.23}$$

with $\gamma_c = -0.1423$, $\beta_1 = 1.0529$, $\beta_2 = 0.3334$, A=0.0311,B=-0.048,C=0.0020,D=-0.0116.

In LDA, the only information of the density at point $\vec{r}$ is relevant (local information), but every real system has a spatially varying density $\rho(\vec{r})$ because of inhomogeneities (i.e. we are not in an homogeneous electron gas). Based on the analogy with a Taylor expansion of a function, we can calculate gradient corrections for functionals. An obvious approach to improve the LDA is to include such gradient corrections, by making the Exchange-Correlation energy (E_{XC}) a functional of the density and its gradient: if one stops the development to the first gradient (derivative), one gets the Generalized Gradient Approximation (GGA). In our work, we used a popular GGA functional: the BLYP functional ([29, 30]). The exchange and correlation energies are written:

$$\epsilon_x^{B88} = \epsilon_x^{LDA}\left(1 - \frac{\beta}{2^{1/3}A_x}\frac{x^2}{1+6x\beta sinh^{-1}(x)}\right) \tag{2.24}$$

where $x = 2^{1/3}\frac{|\nabla\rho(\vec{r})|}{\rho(\vec{r})^{4/3}}$, $A_x = (3/4)(3/\pi)^{1/3}$, and $\beta = 0.0042$

$$\epsilon_c^{LYP} = -\frac{a}{1+d\rho^{-1/3}}\ \rho + b\rho^{-2/3}\left[C_F\rho^{5/3} - 2t_W + \frac{1}{9}\left(t_W + \frac{1}{2}\nabla^2\rho\right)\right]e^{-}c\rho^{-1/3}$$

with
$t_W = \frac{1}{8}\frac{|\nabla\rho|^2}{\rho} - \frac{1}{8}\nabla^2\rho$, $C_F = 3/10(3\pi^2)^{2/3}$, $a = 0.04918$, $b = 0.132$, $c = 0.2533$ $d = 0.349$

and $E_{XC}^{BLYP}[\rho] = \int \rho(\vec{r})(\epsilon_x^{B88} + \epsilon_c^{LYP})d\vec{r}$.

However, it has been shown that dispersion forces are poorly described by GGA functionals. Different empirical corrections have been proposed to improve the structural properties

without raising the computational cost and which have become now a routinely choice. In particular among such empirical approaches, we would like to mention the Grimme corrections ([31]) which we have used in all our applications to both matrix and gas phase environments.

Dispersion corrections

Intermolecular interactions represent key quantities when real compounds of chemical and biological interest are concerned. In fact one of the main challenge of theoretical chemistry consists in calculating as accurately as possible such energies. Nevertheless, some contributions, namely the **dispersion**, appear to be much harder to describe than, for instance, electrostatic and exchange parts. Indeed, dispersion originates from quantum fluctuations of the charge distribution, generating instantaneous dipoles that interfere attractively according the well-known $-\frac{C_6}{R^6}$ law for the energy, where R represents the intermolecular distance and C_6 a specific coefficient of the system [32]. Electronic correlation can describe the static part of the dispersion energy as it breaks the spherical symmetry of the charge distribution because of various electronic excitations towards virtual orbitals. At the lowest level, Hartree-Fock (HF) theory puts each electron in a mean field representing the effects of all other electrons, which prevents dispersion to be treated this way. Electronic correlation must be included either through special functionals that take this effect directly into account or van der Walls corrections in DFT or through post-HF methods. Let us stress that the two important requirements are numerical accuracy and speed of calculation. Indeed, we have to deal with chemical accuracy around 1 kcal/mol or 2 mHa, which is extremely small.
Standard DFT, with LDA or GGA is unable to take dispersion into account properly because it arises from long-range electronic correlations, whereas DFT can only treat correlation at short distances (≈1 Å, corresponding to overlapping charge densities). However several breakthrough have become popular in the last few years and are described below.

Semi-empirical vdW corrections to DFT functionals are the most popular approach. The dispersion energy is an additional term to the Kohn-Sham energy made mostly of pairwise interactions and it does not depend on electron densities but on atomic coordinates [33]:

$$E_{disp}^{DFT-D} = -\sum_{AB}\sum_{n=6,8,10,\ldots} s_n \frac{C_n^{AB}}{R_{AB}^5} f_{damp}(R_{AB}) \tag{2.25}$$

where C_n^{AB} are the isotropic nth-order dispersion coefficients for the pair of atoms A and B, located at a distance R_{AB}; s_n is a global scaling factor depending on the repulsive behavior of

the functional used; f_{damp} is a damping function to avoid singularities for small interatomic distances as well as double-counting effects at intermediate distances.
Grimme and co-workers first opted for C_6 terms only [32]. In the D2 version, the C_6^{AB} coefficients come from the expression of single atom coefficients (C_6^A for instance). These atomic C_6^A coefficients are derived from atomic ionization potentials I_p^A and static dipole polarizabilities α^A obtained at the PBE0 level: $C_6^A = 0.05 N I_p^A \alpha^A$, where a value of N is associated to each row in the periodic table (2, 10, 18, 36 and 54 for the first five rows). This approach represents a choice for a consistent evaluation of the C_6^A coefficients over a large part of the periodic table. These coefficients can be used in combination to other functionals, not only PBE0.
The damping function has the form:

$$f_{damp}^{D2}(R_{AB}) = \frac{1}{1 + exp^{-d(R_{AB}/R_r - 1)}} \tag{2.26}$$

where R_r corresponds to the sum of atomic vdW radii and d is an adjustable parameter for corrections at intermediate distances.
Grimme augmented and refined his DFT-D method in the D3 version [34]. First, the C_6^{AB} dispersion coefficients are now derived from Time-Dependent DFT calculations starting from the Casimir-Polder formula including the averaged dipole polarizability α^A at imaginary frequency ω:

$$C_6^{AB} = \frac{3}{\pi} \int_0^\infty \alpha^A(i\omega)\alpha^B(i\omega) d\omega \tag{2.27}$$

which was further modified to work with reference molecules instead of free atoms for consistent treatment of dispersion implying molecules. Going further, dependence in local coordination was inserted, allowing a more flexible treatment of system-dependent information like hybridization states of atoms in molecules. Then, higher order pairwise C_8^{AB} coefficients, i.e. dispersion with decay in R^{-8}, were added and recursively computed using the C_6^{AB} values and multipole-type expectation values derived from atomic densities. Finally, **3-body terms** of the energy derived from third-order perturbation theory can be added to the Kohn-Sham energy even though they only account for a few percents of the total dispersion energy.

$$E^{ABC} = \frac{C_9^{ABC}(3cos\theta_a cos\theta_b cos\theta_c + 1)}{(R_{ab}R_{bc}R_{ca})^3} \tag{2.28}$$

where θ_i are internal angles of the ABC triangle and C_9^{ABC} is a constant that can be approximated by $-\sqrt{C_6^{AB}C_6^{AC}C_6^{BC}}$.
Grimme D2 and D3 dispersion corrections in DFT-MD simulations are the most widely used

strategies to correct standard DFT functionals because of their simplicity and broad range of applications, from molecules to condensed phases, and because of their low computational cost [33]. Normally, due to additional terms, the D3 version should be clearly more expensive than the D2 version, but in our work the computational cost is not too much increased such that we have decided to use this version (D3) for our dynamics.

2.4 Born-Oppenheimer molecular dynamics

We finally turn to the description of the molecular dynamics approach. In the electronic representation, one of the most popular DFT-MD approach is the Born-Oppenheimer Molecular Dynamics (BOMD). In BOMD we first optimize the wavefunction at fixed nuclei positions to have the minimum energy (ground state) for the given nuclei configuration ($E_0 = E_0[\vec{R}]$) at time t : $\Psi_0(\vec{r}_1, \ldots, \vec{r}_N; \left\{\vec{R}_I(t)\right\})$.

We then get the forces from the Hellmann-Feynman theorem ([35, 36])) as written in equation 2.29 (here I is one of the N_n nuclei of the system):

$$\vec{F}_I(t) = -\frac{\partial E_0}{\partial \vec{R}_I} = -\left.\frac{\partial E}{\partial \vec{R}_I}\right|_{\phi_i=\phi_i^0} = -\int d^3\vec{r}\,\frac{\partial V_{ext}(\vec{r}, \vec{R}(t))}{\partial \vec{R}_I}\rho(\vec{r}) \tag{2.29}$$

since only V_{ext} depends explicitly on the nuclei positions. In this case the wave-function is calculated on a grid. $\vec{R}_I$ represents the nuclear (cartesian) coordinates, $\vec{r}$ represents the electronic (cartesian) coordinates and E_0 is the ground state electronic energy (assuming no coupling with excited states). Ψ_0 is the associated ground-state electronic wave function (as we have seen before) and it is expressed as a linear combination of atomic orbital ϕ_i. More importantly, considering non interacting electrons allows for the introduction of one-electron wave-functions, $\phi_i(\vec{r})$ with $i = i, N$ (spinorbitals, i.e. spatial and spin coordinates taken into account). This means that the electronic structure problem will be no longer treated through density only but with a "dual approach" implying both electronic density and one-electron orbitals.
The nuclear configuration is propagated $\vec{R}(t) \rightarrow \vec{R}(t + \delta t)$ by solving Newton's equations of motion with the Velocity Verlet algorithm (equation 2.30):

$$\begin{aligned} \vec{R_I}(t+\delta t) &= \vec{R_I}(t) + \delta t\, \vec{v_I}(t) + \frac{\delta t^2}{2M_I}\vec{F_i}(t) \\ \vec{v_I}(t+\delta t) &= \vec{v_I}(t) + \frac{\delta t}{2M_i}\left[\vec{F_I}(t) + \vec{F_I}(t+\delta t)\right] \end{aligned} \tag{2.30}$$

where $\vec{F_I}$(t) and $\vec{F_I}$(t+δt) are forces on the nuclei from equation 2.29, M_I are the nuclei masses and δt is the time-step (0.4 fs in our application).

To sum up, our methodology consists in DFT-based molecular dynamics simulations, performed within the Born-Oppenheimer (BOMD) framework [37, 38]. In our dynamics, the nuclei are treated classically and the electrons quantum mechanically within the DFT formalism. Dynamics consist in solving Newton's equations of motion at finite temperature, with the forces that act on the nuclei deriving from the Kohn-Sham energy. In BOMD the Schrödinger equation for the electronic configuration of the system is solved at each time step of the dynamics (i.e. at each new configuration of the nuclei). We have previously said that the nuclear configuration is propagated by solving Newton's equations of motion, so we have to defined initial conditions ($\vec{R_I}(0)$,$\vec{v_I}(0)$) for our DFT-MD trajectories. This will be presented in chapter 3.

2.5 Dual GPW representation in CP2K

All our DFT-based molecular dynamics simulations are done with the CP2K package [37]. In CP2K, calculations can be performed for system size up to hundreds or thousand atoms [39]. For large systems, strong computational limitations come from the treatment of the Hartree energy and the orthogonalization of the wave functions as they do not scale linearly with the number of atoms. One solution consists in a mixed approach including Gaussian basis set and plane waves as implemented in CP2K [40]. A dual representation of the density is applied: one in the real space expanded on a contracted Gaussian basis set ans one in the reciprocal space expanded on a plane-wave basis set, both spaces being linked by the efficient Fast Fourrier Transform (FFT). This giving rise to the dual GPW representation.

Plane-Waves

The reciprocal lattice is a construction of all wave vectors $\vec{G}$ that give plane waves and it is generally used for condensed matter physics. Plane-Waves (PW) of the form $\exp(i\vec{G}.\vec{r})$ are particularly well suited for calculations requiring periodic boundary conditions, meaning that they make several integrals easier to handle because of their intrinsic periodicity.
The size of a plane-wave basis set is defined by imposing an energy cutoff, i.e. a single parameter. Let $\phi_{\vec{G}}(\vec{r})$ be a basis set element. It is an eigenvector of the kinetic energy operator:

$$-\frac{1}{2}\nabla^2\phi_{\vec{G}}(\vec{r}) = \frac{1}{2}\|\vec{G}\|^2\phi_{\vec{G}}(\vec{r}) \tag{2.31}$$

The basis set elements are selected according to:

$$E_{kin} = \frac{1}{2}\|\vec{G}\|^2 < E_{kin}^{cut} \tag{2.32}$$

where E_{kin}^{cut} represents the kinetic cutoff such that the $\vec{G}$ vectors of the basis set are all points on a regular mesh within a sphere radius of $G_{max} = \sqrt{2E_{kin}^{cut}}$. This cutoff provides the real space grid spacing h: $E_{kin}^{cut} = \frac{\pi}{2h^2}$ [40]. The number of PW basis set elements, N_{PW}, can be estimated from the ratio between the volume of the sphere radius G_{max} and the volume associated with one $\vec{G}$ vector $\frac{(2\pi)^3}{\Omega}$, Ω being the volume of the whole cell:

$$\frac{(2\pi)^3}{\Omega}N_{PW} = \frac{4}{3}\pi G_{max}^3 \tag{2.33}$$

The kinetic energy cutoff is related to another energy cutoff associated to the electron density. Indeed, expanding the electron density into the Kohn-Sham orbitals $\phi_i(\vec{r})$, written as combination of PW basis set, we have:

$$\begin{aligned}
\rho(\vec{r}) &= \sum_i |\phi_i(\vec{r})|^2 && (2.34)\\
&= \frac{1}{\Omega}\sum_i\sum_{\vec{G},\vec{G'}} c_i^*(\vec{G'})c_i(\vec{G})e^{i(\vec{G}-\vec{G'}).\vec{r}} && (2.35)\\
&= \frac{1}{\Omega}\sum_{\|\vec{G}\|<2G_{max}} \tilde{n}(\vec{G})e^{i\vec{G}.\vec{r}} && (2.36)
\end{aligned}$$

From this equation and the double summation, one gets a new maximum for $\|\vec{G}\|$, i.e. $2G_{max}$. Since G_{max} was previously defined as $G_{max} = \sqrt{2E_{kin}^{cut}}$, we get $2G_{max} = \sqrt{2 \times 4E_{kin}^{cut}}$ and the

new density cutoff finally corresponds to $4E_{kin}^{cut}$.

In CP2K, the density cutoff is expressed in Rydberg. In the work presented here we use a cutoff energy value of 340 Ry. This corresponds to a kinetic energy threshold of 85 Ry. Such a density cutoff for a cubic simulation box of 10.74 $Å^3$ (this corresponds to the size of the box of the argon matrix, see chapter 5) provides 5.10^7 plane waves, i.e. working with plane-waves requires a very large number of basis set elements.
Plane-waves have some drawbacks: they are present even if the space is empty of electrons and nuclei and core electrons are difficult to represent [39]. Indeed, close to the nucleus, the electronic wavefunction shows quick oscillations.

Pseudopotentials

The description of the density by plane-wave basis set needs the use of **pseudopotentials** (the cut-off energy for core electrons is too high), so that the plane waves are only used to describe the valence charge density. Indeed, pseudo potentials aim at reducing the size of the plane wave basis set by replacing core electrons by approximated potentials and considering together these electrons and the nuclei as a rigid non-polarisable ionic cores. They have to accurately represent long-range interactions after a given value of a cutoff radius and their construction must give nodeless valence wavefunctions orthogonal to the core states. It is assumed that non significant overlap between core and valence electrons occurs.
In CP2K, the core electrons are treated with the GTH (Goedecker-Tetter-Hutter) pseudopotentials ([41, 42]).

Gaussian basis set

Gaussian basis sets are very popular because they provide simple analytical expressions for several energetic contributions. However, one Gaussian-type orbital ($r^l Y_{l,m}(\theta,\phi)\exp(-\alpha r^2)$, where $Y_{l,m}(\theta,\phi)$ are spherical Harmonics) fails at reproducing the correct asymptotic behavior given by Slater-Type Orbitals ($r^l Y_{l,m}(\theta,\phi)\exp(-\zeta r)$, STO). One STO function is thus expressed as a linear combination of Gaussian Type Orbitals (GTO's) called primitive Gaussian functions. These orbitals are non-orthogonal, i.e. they can overlap, which may cause basis-set superposition error (BSSE) in interaction energy calculation for atoms close enough in space.
In CP2K, several gaussian basis sets are available, especially for the first two rows of the periodic classification, with increasing numbers of primitive Gaussian functions to reach a better description of the pseudoatomic wavefunction. In the GPW (Gaussian Plane Wave)

approach, only the valence electrons need a description, the core electrons being included in the pseudopotentials. For instance, for oxygen atom 4 primitive functions are used at the double-ζ valence (or DZV level), 5 at the triple-ζ valence (TZV), and 6 at quadruple-ζ valence (QZV level). These basis-sets can be compared with the all-electron (core+valence) Gaussian basis sets: for instance, the valence part of 6-311G*, i.e. 311G*, corresponds to TZVP basis set. If polarisation functions are added, the basis sets are accordingly modified: DZVP, TZVP, TZV2P (where 2 indicates the number of polarisation functions) etc. Augmentation is made possible by adding diffuse functions which can be important in gas phase studies. For condensed phase, Hütter and VandeVondele have built Molecular OPTimized (MOLOPT) Gaussian basis sets [43]. These compact basis sets include smooth primitive Gaussian functions, reducing BSSE. Moreover, the MOLOPT basis sets avoid linear dependencies between basis functions, ensuring that the overlap matrix is well conditioned. This is particularly important when Cholesky decomposition is applied since linear dependencies cause it to fail. In the GPW implementation [40], several grids are used to perform numerical calculations. The value of the exponent α of a Gaussian function is related to a given grid and the number of grid points is exponent-independent. The larger the exponent, the more contracted the Gaussian function: a thin grid is required for an accurate description. The exponent is chosen to $\alpha = 1$ for the finest grid.

Dual GPW representation

The total electronic energy can be divided into four terms which will be treated either in real space with Gaussian functions or in the Fourier space with plane-wave expansion according to their nature. This is the core of the dual GPW representation as implemented in CP2K/Quickstep [40]. As previously shown in equation 2.20, the Kohn-Sham DFT energy expression (as employed within the GPW framework) is defined as:

$$E[\rho] = T[\rho] + E_{en}[\rho] + E_H[\rho] + E_{xc}[\rho] + E_{nn} \tag{2.37}$$

where $T[\rho]$ is the electronic kinetic energy, $E_{en}[\rho]$ is the electronic interaction with the ionic cores, $E_H[\rho]$ is the electronic Hartree energy, $E_{xc}[\rho]$ is the exchange-correlation energy and E_{nn} is the interaction energies of the ionic cores.
The kinetic energy $T[\rho] = \sum_{\mu\nu} P^{\mu\nu} \langle \chi_\mu(\vec{r}) \left| -\frac{1}{2}\nabla^2 \right| \chi_\nu(\vec{r}) \rangle$ is computed using the Gaussian basis set elements $\chi_\mu(\vec{r})$ and $\chi_\nu(\vec{r})$. $P^{\mu\nu}$ is an element of the density matrix used for moving from the Kohn-Sham orbital ϕ_i basis functions to the Gaussian decomposition.

Combining the local part of the $E_{en}[\rho]$, the Hartree energy $E_H[\rho]$ for the valence electron and the nuclei/nuclei interaction E_{nn} provides the electrostatic energy. The short-range terms of the full electrostatic energy will be treated in real space whereas the long-range one will be evaluated in the Fourier space.
Finally the exchange-correlation energy $E_{xc}[\rho]$ is discretized in real space; density gradients are approximated numerically on the grid and the exchange-correlation energy per particle as well as its derivatives are evaluated on each grid point. This allows the calculation of the exchange-correlation potential and thus of the final energy contributions after multiplication by Gaussian basis function [40].

2.6 Computational details

In this thesis, two different prototypical examples have been studied: 1) the gas phase illustrated by the $(Cl^-...NMA)Ar$ cluster (NMA is the N-MethylAcetaminde) and 2) the condensed phase with a Formic Acid molecule embedded in an argon matrix.
For both systems, we performed DFT-based Born-Oppenheimer molecular dynamics simulations (BOMD) with CP2K package [37], where the nuclei are treated classically and the electrons quantum mechanically within the DFT (Density Functional Theory) formalism. BLYP functional, [29, 30] including Grimme D3 correction for dispersion [34], combined with Goedecker-Teter-Hutter (GTH) pseudopotentials [41], is used. A hybrid Gaussian and plane wave representation of the electronic wave function is employed with the TZV2PX Gaussian basis set from the MOLOPT database and a plane wave density cut-off of 340 Ry. The choice of the Gaussian basis set and the plane wave energy cut-off was carefully determined through convergence tests. Two cubic cells with a side of 10.7 Å (Formic Acid molecule and 29 argon atoms) and 20 Å (Cl^-...NMA) were chosen. The BOMD dynamics are performed in the micro canonical NVE ensemble with a time-step of 0.4 fs.

We now report the specificities of computational details of the two systems. In the case of Formic Acid molecule in argon matrix Periodic Boundary Conditions (PBC) are applied. 25 independent trajectories have been performed with initial vibrational excitation into two combination modes: the O-H stretching and the O-H wagging. Trajectories have been accumulated for 16 to 40 ps depending on what we are interesting in (IVR, isomerisation, deformation of the matrix).

In the case of $(Cl^{-}...NMA)Ar$ cluster gas phase simulations are performed. Thus, the decoupling technique of Martyna and Tuckerman [44] for eliminating the effect of the periodic images of the charge density is applied. 15 independent trajectories of 12 ps each have been performed with initial vibrational excitation in the N-H stretching motion.

Chapter 3

Normal mode sampling of initial conditions

In our work, one of the main aspect is to define initial conditions for DFT-MD simulations. Indeed, to obtain accurate results from a chemical dynamics simulation, it is paramount that proper initial conditions (i.e. positions and momenta) are chosen for the ensemble of trajectories propagated to compare with experiment. This is particularly relevant since we want to understand what happens after a vibrational excitation. An appropriate sampling of these {Q(0);P(0)} is thus crucial for further analyzing our trajectories. Once the initial conditions set, we will run trajectories and analyze them by following the energy of the normal modes along the dynamics. The two aspects of the present work will be detailed in this chapter and in chapter 4, respectively.

3.1 Hamiltonian of 3N-6 uncoupled harmonic oscillators

Our first goal is to define initial conditions for our trajectories of molecular dynamics which take into account one or several vibrational excitations. We thus have to define coordinates (x,y,z) and velocities (v_x,v_y,v_z) at $t = 0$ of the dynamics corresponding to the perturbation of the vibrational excitations.

In the harmonic approximation, any molecule or molecular system consisting of N atoms can be treated as $3N-6$ uncoupled harmonic oscillators. The Hamiltonian of $3N-6$ uncoupled

harmonic oscillators is:

$$H_{harm} = \frac{1}{2}\sum_{i=1}^{3N-6}\frac{P_{harm,i}^2}{\mu_i} + \frac{1}{2}\sum_{i=1}^{3N-6}\mu_i\omega_i^2 Q_{harm,i}^2 \tag{3.1}$$

where H_{harm} is the sum of the kinetic and potential energies of separable harmonic oscillators, and μ_i is the reduced mass of mode i. $Q_{harm,i}$ is the i^{th} harmonic normal mode, $P_{harm,}$: its associated momentum, and ω_i the mode wave-number. In the literature, it is common to refer to mass-weighted Hamiltonian using mass-weighted coordinates. The mass-weighted coordinates Q_i and momenta P_i are related to the non mass-weighted coordinates $Q_{harm,i}$ and $P_{harm,i}$ by:

$$Q_i = \sqrt{\mu_i}Q_{harm,i} \tag{3.2}$$

$$P_i = \frac{P_{harm,i}}{\sqrt{\mu_i}} \tag{3.3}$$

So, we can re-write the Hamiltonian as:

$$H = \frac{1}{2}\sum_{i=1}^{3N-6}P_i^2 + \frac{1}{2}\sum_{i=1}^{3N-6}\omega_i^2 Q_i^2 \tag{3.4}$$

In quantum mechanic the energy of each harmonic normal mode is:

$$E_i = (n_i + \frac{1}{2})\hbar\omega_i \tag{3.5}$$

where $\hbar$ is the Planck constant, $\frac{1}{2}\hbar\omega_i$ corresponds to the zero-point energy and n_i is the vibrational level (quantum number). The total energy of the $3N-6$ normal modes is $E = \sum_{i=1}^{3N-6}E_i$.

Classically Q_i and P_i evolve in time as:

$$Q_i(t) = \frac{(2E_i)^{(1/2)}}{\omega_i}\cos(\omega_i.t + \phi) \tag{3.6}$$

$$P_i(t) = -(2E_i)^{(1/2)}\sin(\omega_i.t + \phi) \tag{3.7}$$

Since we need initial conditions for the dynamics, it is crucial to know the positions and velocities $Q_i(0)$, $P_i(0)$ at $t = 0$. The equations 3.6 and 3.7 now read:

$$Q_i(0) = \frac{(2E_i)^{(1/2)}}{\omega_i}\cos(\phi) = A_i\cos(2\pi R_i) \tag{3.8}$$

$$P_i(0) = -(2E_i)^{(1/2)} \sin(\phi) = -\omega_i A_i \sin(2\pi R_i) \tag{3.9}$$

where $\phi = 2\pi R_i$ is the phase. In practice, the phase can be directly obtained by choosing R_i which is a random number in the interval [0-1].
A_i is the mass-weighted amplitude of motion defined by:

$$A_i = \frac{(2E_i)^{(1/2)}}{\omega_i} \tag{3.10}$$

The relation between the mass-weighted amplitude A_i and the non-mass weighted amplitude A'_i that will be used later is:

$$A'_i = \frac{A_i}{\sqrt{\mu_i}} \tag{3.11}$$

3.2 Initial conditions sampling

We have considered **three** approaches for modeling the vibrational energy absorption of one or several photons into given vibrational modes by defining the initial conditions (Q_i, P_i) for the dynamics in cartesian coordinates (x,y,z,v_x,v_y,v_z). They are called "Classical sampling", "Wigner quantum sampling" and "Semi-Classical Wigner sampling" and are described below.

1) Classical sampling.
In the classical sampling, the initial conditions for molecular dynamics simulations are positions and velocities (Q_i, P_i) defined by the equations 3.8 and 3.9. In practice, random values for the coordinates Q_i and momenta P_i are chosen by giving each normal mode a random phase $2\pi R_i$ (R_i is a random number chosen in the interval [0-1] so that the phase is in the interval [0-2π]).

2) Wigner Quantum sampling.
The Wigner function, introduced by Wigner in 1932 [45] may be used to select initial coordinates and momenta for trajectory calculations [46]. The Wigner distribution (i.e. density) function $W(\vec{q},\vec{p})$ gives the classical probability density, which reproduces the quantum distributions in positions $\vec{q}$ and momenta $\vec{p}$. Given a quantum mechanical wave function $\Psi(\vec{q})$, the Wigner distribution function is defined as [45]

$$W(\vec{q},\vec{p}) = \frac{1}{(2\pi\hbar)^n} \int d\vec{s} \exp(i\vec{p}\cdot\vec{s}/\hbar)\Psi(\vec{q}-\vec{s}/2)\Psi(\vec{q}+\vec{s}/2) \tag{3.12}$$

where $\vec{s}$ is a spatial variable and N is the number of dimensions. This function satisfies the normalization condition

$$\int\int W(\vec{q},\vec{p})d\vec{q}d\vec{p} = 1 \tag{3.13}$$

and when integrated over the momenta yields to the quantum mechanical coordinate probability distribution $\mid \Psi(\vec{q})\mid^2$:

$$\int W(\vec{q},\vec{p})d\vec{p} = \mid \Psi(\vec{q})\mid^2 \tag{3.14}$$

The equation 3.12 gives the general expression for the Wigner distribution function; for uncoupled harmonic oscillators the Wigner distribution for each Q_i, P_i pair takes the form

$$W^n(Q',P') = (-1)^n(\pi n!)L_n(\rho)\exp(-\rho^2/2) \tag{3.15}$$

where L_n is the nth order Laguerre polynomial and ρ is given by

$$\rho^2 = 2(P'^2 + Q'^2) \tag{3.16}$$

with $Q' = \sqrt{\omega/\hbar}Q$ and $P' = P/\sqrt{\omega\hbar}$.

Then, the Wigner density probability for the vibrational ground state $W^0(Q_i,P_i)$ for the normal mode (Q_i,P_i) is:

$$W^0(Q_i,P_i) = \frac{1}{\pi\hbar}\exp(-\frac{P_i^2}{\hbar\omega_i})\exp(-\frac{\omega_i Q_i^2}{\hbar}) \tag{3.17}$$

To have initial conditions, it is practical to obtain separated probability function for Q and P to sample them. In the case of Q_i, the probability $\mathcal{P}^0(Q_i)$ is the integral of $W^0(Q_i,P_i)$ over

all possible P_i:

$$\begin{aligned}
\mathcal{P}^0(Q_i) = \int_{-\infty}^{\infty} W^0(Q_i, P_i) dP_i &= \frac{1}{\pi\hbar} \int_{-\infty}^{\infty} \exp(-\frac{P_i^2}{\hbar\omega_i}) \exp(-\frac{\omega_i Q_i^2}{\hbar}) dP_i \\
&= \frac{1}{\pi\hbar} \exp(-\frac{\omega_i Q_i^2}{\hbar}) \int_{-\infty}^{\infty} \exp(-\frac{P_i^2}{\hbar\omega_i}) dP_i \\
&= \frac{1}{\pi\hbar} \exp(-\frac{\omega_i Q_i^2}{\hbar}) \sqrt{\hbar\omega_i\pi} \\
&= \sqrt{\frac{\omega_i}{\pi\hbar}} \exp(-\frac{\omega_i Q_i^2}{\hbar}) \qquad (3.18)
\end{aligned}$$

where to solve the integral $\int_{-\infty}^{\infty} \exp(-\frac{P_i^2}{\hbar\omega_i}) dP_i$, we have used the well-known relationship $\int_{-\infty}^{\infty} \exp(-\alpha x^2) = \sqrt{\pi/\alpha}$.

$\mathcal{P}^0(Q_i)$ is not normalized. To obtain a normal probability function we have defined: $\mathcal{P}^{0,max}(Q_i) = max\left[\mathcal{P}^0(Q_i)\right] = \sqrt{\omega_i/\pi\hbar}$ being the maximum of this probability, getting:

$$F^{n=0}(Q_i) = \frac{\mathcal{P}^0(Q_i)}{\mathcal{P}^{0,max}(Q_i)} = \exp(-\frac{\omega_i Q_i^2}{\hbar}) \qquad (3.19)$$

which is the normalized Wigner distribution of the vibrational ground-state ($n_i = 0$) normal mode Q_i.

In the case of P_i, the probability $\mathcal{P}^0(P_i)$ is calculated as the integral over all Q_i:

$$\begin{aligned}
\mathcal{P}^0(P_i) &= \int_{-\infty}^{\infty} W^{n=0}(Q_i, P_i) dQ_i \\
&= \frac{1}{\pi\hbar} \int_{-\infty}^{\infty} \exp(-\frac{P_i^2}{\hbar\omega_i}) \exp(-\frac{\omega_i Q_i^2}{\hbar}) dQ_i \\
&= \frac{1}{\pi\hbar} \exp(-\frac{P_i^2}{\hbar\omega_i}) \int_{-\infty}^{\infty} \exp(-\frac{\omega_i Q_i^2}{\hbar}) dQ_i \\
&= \frac{1}{\pi\hbar} \exp(-\frac{P_i^2}{\hbar\omega_i}) \sqrt{\frac{\pi\hbar}{\omega_i}} \\
&= \sqrt{\frac{1}{\omega_i\pi\hbar}} \exp(-\frac{P_i^2}{\hbar\omega_i}) \qquad (3.20)
\end{aligned}$$

Similarly to Q_i, we define $\mathcal{P}^{0,max}(P_i)$ as the maximum of this probability:

$$F^{n=0}(P_i) = \mathcal{P}^{0,max}(P_i) = max\left[\mathcal{P}(P_i)\right] = \sqrt{\frac{1}{\omega_i \pi \hbar}} \tag{3.21}$$

and

$$\frac{\mathcal{P}^0(P_i)}{\mathcal{P}^{0,max}(P_i)} = \exp(-\frac{P_i^2}{\hbar\omega_i}) \tag{3.22}$$

which is the normalized Wigner distribution of the vibrational ground-state ($n_i = 0$) normal mode P_i.

In the first vibrationally excited state $n_i = 1$, the Wigner density probability $W^1(Q_i, P_i)$ for the normal mode (Q_i, P_i) reads:

$$W^1(Q,P) = \frac{-1}{\pi\hbar}(1 - \frac{2P_i^2}{\hbar\omega_i} - \frac{2\omega_i Q_i^2}{\hbar})\exp(-\frac{P_i^2}{\hbar\omega_i} - \frac{\omega_i Q_i^2}{\hbar}) \tag{3.23}$$

so that the probability $\mathcal{P}^1(Q_i)$ can be written:

$$\begin{aligned}
\mathcal{P}^1(Q_i) &= \int_{-\infty}^{\infty} W^{n=1}(Q_i, P_i) dP_i \\
&= -\frac{1}{\pi\hbar}\int_{-\infty}^{\infty}(1 - \frac{2P_i^2}{\hbar\omega_i} - \frac{2\omega_i Q_i^2}{\hbar})\exp(-\frac{P_i^2}{\hbar\omega_i} - \frac{\omega_i Q_i^2}{\hbar})dP_i \\
&= -\frac{1}{\pi\hbar}\left[(1 - \frac{2\omega_i Q_i^2}{\hbar})\exp(-\frac{\omega_i Q_i^2}{\hbar})\int_{-\infty}^{\infty}\exp(-\frac{P_i^2}{\hbar\omega_i})dP_i - \frac{2}{\hbar\omega_i}\exp(-\frac{\omega_i Q_i^2}{\hbar})\int_{-\infty}^{\infty}P_i^2\exp(-\frac{P_i^2}{\hbar\omega_i})dP_i\right] \\
&= -\frac{1}{\pi\hbar}\left[(1 - \frac{2\omega_i Q_i^2}{\hbar})\exp(-\frac{\omega_i Q_i^2}{\hbar})\sqrt{\pi\hbar\omega_i} - \frac{2}{\hbar\omega_i}\exp(-\frac{\omega_i Q_i^2}{\hbar})\frac{\hbar^{3/2}\omega_i^{3/2}\sqrt{\pi}}{2}\right] \\
&= -\sqrt{\frac{\omega_i}{\pi\hbar}}\left[(1 - \frac{2\omega_i Q_i^2}{\hbar})\exp(-\frac{\omega_i Q_i^2}{\hbar}) - \exp(-\frac{\omega_i Q_i^2}{\hbar})\right] \\
&= -\sqrt{\frac{\omega_i}{\pi\hbar}}\left[-\frac{2\omega_i Q_i^2}{\hbar}\exp(-\frac{\omega_i Q_i^2}{\hbar})\right] \\
&= \frac{2\omega_i^{3/2}}{\hbar^{3/2}\pi^{1/2}}Q_i^2\exp(-\frac{\omega_i Q_i^2}{\hbar})
\end{aligned} \tag{3.24}$$

The following solutions have been used to obtain the integration of $\int_{-\infty}^{\infty} P_i^2\exp(-\frac{P_i^2}{\hbar\omega_i})dP_i$

and $\int_{-\infty}^{\infty} \exp(-\frac{P_i^2}{\hbar\omega_i})dP_i$ respectively:

$$\int_{-\infty}^{\infty} x^2 \exp(-\gamma x^2)dx = \frac{\sqrt{\pi}}{2\gamma^{3/2}} \tag{3.25}$$

and

$$\int_{-\infty}^{\infty} \exp(-\gamma x^2) = \sqrt{\frac{\pi}{\gamma}} \tag{3.26}$$

In order to have the maximum of the function in equation 3.24 we have to calculate the derivative with respect to Q_i. If we define $\alpha = \frac{2\omega_i^{3/2}}{\hbar^{3/2}\pi^{1/2}}$, then $\mathcal{P}^1(Q_i) = \alpha Q_i^2 \exp(-\frac{\omega_i Q_i^2}{\hbar})$, and the derivative is:

$$\frac{d}{dQ_i}\mathcal{P}^1(Q_i) = \alpha\left[2Q_i \exp(-\frac{\omega_i Q_i^2}{\hbar}) - \frac{2Q_i^3\omega_i}{\hbar}\exp(-\frac{\omega_i Q_i^2}{\hbar})\right] = 2Q_i\alpha\left[1 - \frac{\omega_i Q_i^2}{\hbar}\right]\exp(-\frac{\omega_i Q_i^2}{\hbar}) \tag{3.27}$$

The maximum is obtained when $\frac{d}{dQ_i}\mathcal{P}^1(Q_i) = 0$.

There are three solutions: $Q_i = 0$ and $Q_i = \pm\sqrt{\hbar/\omega_i}$, so that the final associated probabilities are:

$$\begin{aligned} \mathcal{P}^1(Q_i = 0) &= 0 \\ \mathcal{P}^{1,max}(Q_i = \pm\sqrt{\hbar/\omega_i}) &= \frac{2}{e}\sqrt{\omega_i/\hbar\pi} \end{aligned} \tag{3.28}$$

where $e = e^1 = 2.718$, and

$$F^{n=1}(Q_i) = \frac{\mathcal{P}^1(Q_i)}{\mathcal{P}^{1,max}(Q_i = \pm\sqrt{\hbar/\omega_i})} = \frac{e\omega_i}{\hbar}Q_i^2\exp(-\frac{\omega_i Q_i^2}{\hbar}) \tag{3.29}$$

is the normalized Wigner distribution for the normal mode Q_i in its first vibrational excited state $n_i = 1$.

Similarly, the normalized Wigner distribution for the momenta P_i at the vibrational level $n = 1$ is :

$$F^{n=1}(P_i) = \frac{\mathcal{P}^1(P_i)}{\mathcal{P}^{1,max}(P_i = \pm\sqrt{\hbar\omega_i})} = \frac{e}{\hbar\omega_i} P_i^2 \exp(-\frac{P_i^2}{\hbar\omega_i}) \tag{3.30}$$

The sampling of coordinates and momenta $\{Q_i;P_i\}$ is done for $n = 0$ with the Box-Muller transform. It allows us to transform uniformly distributed random variables, to a new set of random variables with a Gaussian distribution. For $n = 1$ the initial conditions are selected "manually" by choosing the $\{Q_i;P_i\}$ in the Wigner quantum distribution as starting points of the dynamics.
Nevertheless, we never used a "full quantum" Wigner sampling for practical reasons (i.e. prevent that there is too much energy in the system). The solution is explained below.

3) Semi-Classical Wigner sampling.
We define a semi-classical sampling of the normal mode coordinates (Q_i,P_i) (ground- and 1st excited-state alike) by selecting Q_i through the Wigner distribution of eq 3.19 (vibrational ground-state) and of eq 3.29 (vibrational first excited state), and evaluate the associated normal mode momentum P_i from the energy conservation relation [47]:

$$E_i = \frac{1}{2}P_i^2 + \frac{1}{2}\omega_i^2 Q_i^2 \Rightarrow P_i = \sqrt{2E_i - \omega_i^2 Q_i^2} \tag{3.31}$$

Classical versus Wigner sampling.

We present here one example for formic acid (FA). This system will be treated in the next chapter. The resulting distributions of the normal mode coordinate Q_i for the O-H stretch of Formic Acid (FA) from the classical sampling and the quantum Wigner sampling are typically reported as an exemple in figure 3.1.

As can be observed in figure 3.1 the classical (n=0 to $n = 5$) and Wigner distributions (n=0 and $n = 1$) are by no means equivalent. Here with the quantum sampling, one finds the proper wave-function distribution of the normal modes, with maxima and tails opposite to the maxima and tails obtained with the classical sampling. Classical distribution for normal mode positions are reported for quantum numbers varying from $n = 0$ to $n = 5$ ($n = 0$ in black, $n = 1$ in red, $n = 2$ in blue, $n = 3$ in green, $n = 4$ in pink and $n = 5$ in orange. Wigner distribution for the O-H stretching are plotted in dotted line for $n = 0$ in black and $n = 1$ in red (we have restricted the plot to $n = 0$ and $n = 1$ for Wigner distribution). With this plot, we show, as has been previously reported for instance by Hase et al. [48] and as is well known, that the maxima of the classical distributions (lines in figure 3.1) are found on the extreme

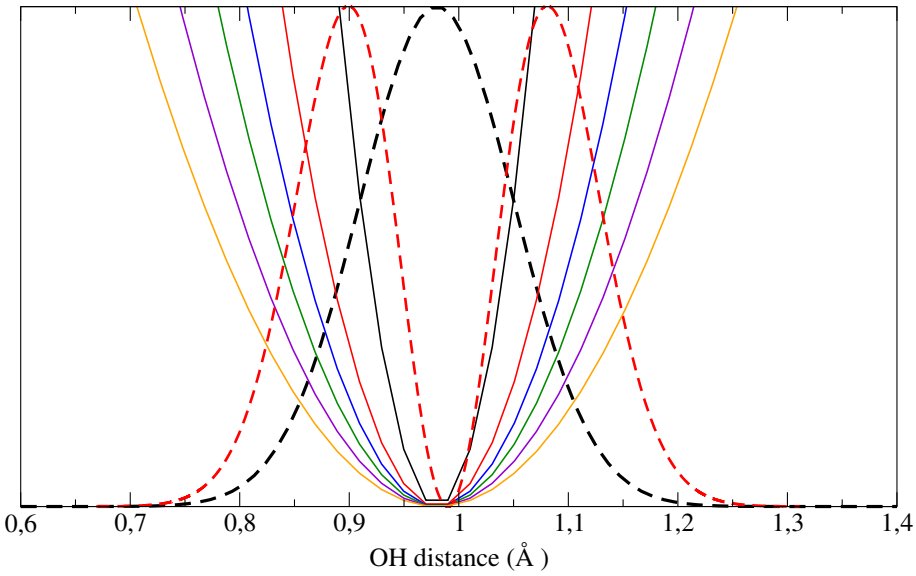

Figure 3.1: O-H stretch in FA molecule: classical distribution for normal mode position for n=0 (black), n=1 (red), n=2 (blue), n=3 (green) n=4 (pink) and n=5 (orange) and Wigner distribution for normal mode position for n=0 (black dotted line) and n=1 (red dotted line).

limit values of the Q_i coordinate while in Wigner distribution the maximum is (for low values of n) closed to the "central" value of Q_i. Here for O-H stretching of FA this "central" value is typically $Q_i = 0.98$ Å and corresponds to the value of the O-H distance in the optimized geometry. The increase of the quantum number n from $n = 0$ to $n = 5$ doesn't change the value of the minimum of probability of the classical distribution always found at $Q_i = 0.98$ Å whereas the extremal values of the distribution are affected by the increase of the quantum number. The quantum Wigner distribution for $n = 0$ shown in the same figure (black dotted line) reveals a totally different behavior. The maximum of the distribution is found at the O-H distance of 0.98 Å and tends to zero for $Q_i = 0.75$ Å and for $Q_i = 1.21$ Å . In figure 3.1 it is also represented the Wigner distribution for positions for $n = 1$. This distribution (in red dotted line) has two maxima located at $Q_i = 0.89$ Å and $Q_i = 1.08$ Å . The minimum of the distribution is the same found for the classical distributions (i.e $Q_i = 0.98$ Å and the tails are found at $Q_i = 0.72$ Å and for $Q_i = 1.24$ Å .
Sun and Hase [46] have shown that for small n the classical and quantum distributions are

very different while for large n values, the quantum and classical distributions become similar (see Fig 3.2).

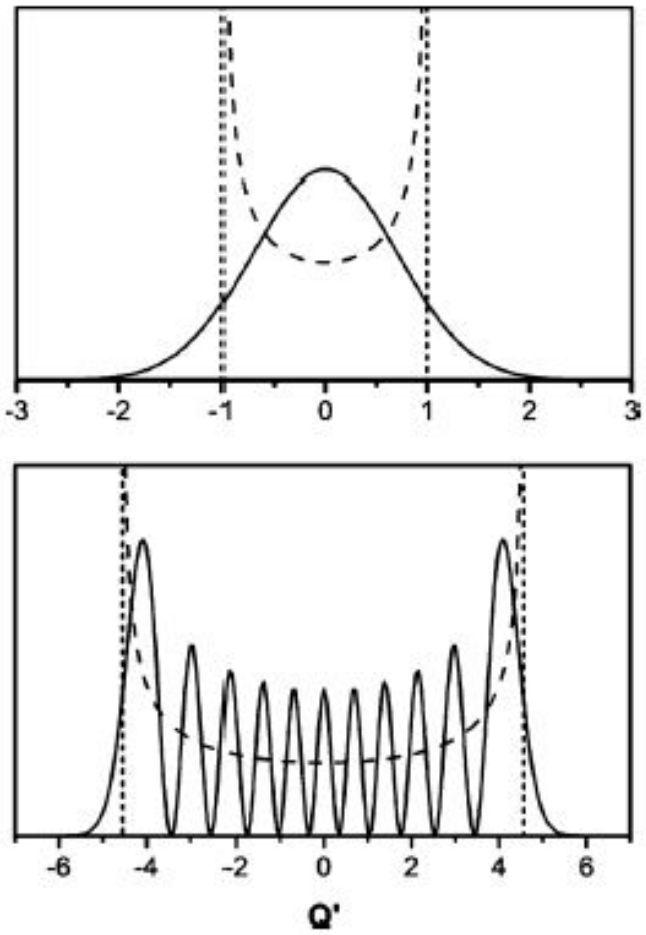

Figure 3.2: Comparison of quantum (solid lines) and classical (dashed lines) probability distributions of the normal mode coordinate Q_i for the quantum states n=0 and n=10 taken from Ref [48].

3.3 Classical turning point and Classically forbidden regions.

The classical turning point problem will be illustrated below with the Formic Acid molecule. The classical representation corresponds to the motion of a harmonic oscillator in terms of its set of normal coordinates and momenta $\{Q_i;\ P_i\}$. The kinetic energy is maximal at the minimum of the potential while the potential energy is maximal at the extremal ends of the potential (the extrema are only defined if E_i is known). This defines the maximal extent, ΔQ_{imax} of oscillation for the classical motion of the oscillator and it is called the "Classical Turning Point". ΔQ_{imax} is defined from the equilibrium distance: ΔQ_{imax} is the gap from the minimum of the classical distribution found at $Q_i = 0.98$ Å . The value of ΔQ_{imax} increases with increasing the quantum number n_i as we can see in figure 3.3.

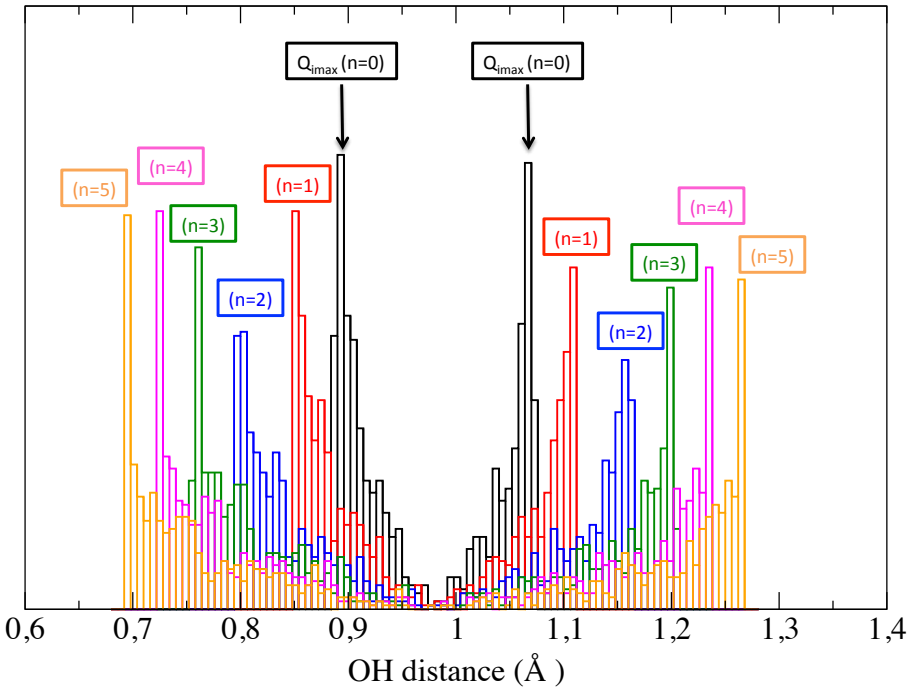

Figure 3.3: Classical distribution for normal mode positions for n=0 (black), n=1 (red), n=2 (blue), n=3 (green) n=4 (pink) and n=5 (orange) and corresponding Classical Turning Point (ΔQ_{imax}).

The classical turning point is obtained by considering that at this particular point the total energy is composed only by potential energy (kinetic energy is zero by definition there).This corresponds to:

$$E_i = (n_i + \frac{1}{2})\hbar\omega_i = \frac{1}{2}\omega_i^2 \Delta Q_{imax}^2 \tag{3.32}$$

and so we can obtain the ΔQ_{imax} value:

$$\Delta Q_{imax} = \pm\sqrt{\frac{(2n_i + 1)\hbar}{\omega_i}} \tag{3.33}$$

By construction, the motion of the oscillator can never go after the turning points in classical mechanics. Table 3.1 gives the value of the classical turning points depending on the quantum number n_i for O-H harmonic oscillator of the Formic Acid extracted from our calculation and compared with the theoretical values from equation 3.33, showing that our classical distributions are correct with a 0.02 Å uncertainty. This explains the fact that there are some non-zero probability also for $\Delta Q > \Delta Q_{imax}$ (see Fig 3.3).

Quantum Number (n_i)	Theoretical ΔQ_{imax} (Å)	ΔQ_{imax} from our code (Å)
n=0	0.09	0.10
n=1	0.16	0.16
n=2	0.21	0.19
n=3	0.25	0.23
n=4	0.28	0.26
n=5	0.31	0.29

Table 3.1: Comparison of the classical turning point (ΔQ_{imax}) between theoretical values from equation 3.33 and values extracted from our code (i.e equation 3.8) for different vibrational excitations (n=0 to n=5) (i.e equation 3.5) for the O-H stretching motion of the Formic Acid.

In the Wigner quantum sampling the distribution of positions Q_i extends into the classically forbidden region and the motion can thus access larger values of Q_i as we can see in the illustration of figure 3.4 for the OH stretching motion of FA molecule. In our selection, the structure will be only chosen into the classical allowed region in order to stay in the most likely part of the Wigner distribution function.

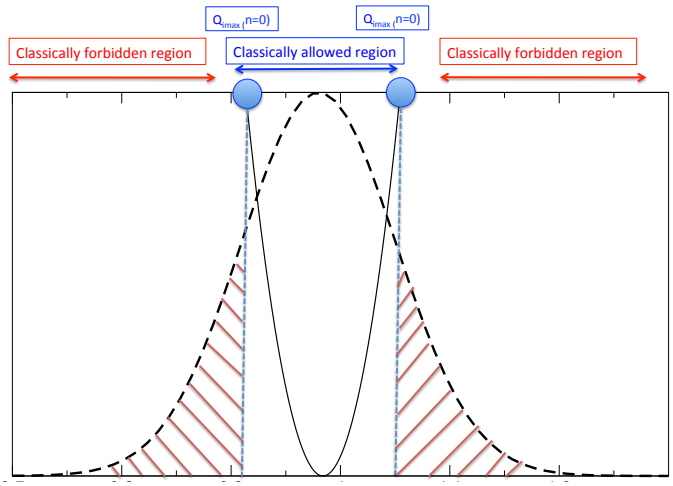

Figure 3.4: Classical and quantum Wigner distributions for normal mode positions for n=0 (classical in black and Wigner in black dashed line). We have highlighted the classical allowed and forbidden regions.

Correcting for spurious harmonic energies.

Our molecular dynamics simulations are in cartesian coordinates and not in normal mode Hamiltonian. This means that anharmonicities are naturally present as well as mode couplings. We can thus introduce a quantity, ΔE, being the difference between the actual energy of each structure and the harmonic energy: $\Delta E = E_{actual} - E_{harm}$. E_{actual} is calculated as the sum of the kinetic and the potential energy after the first step of the DFT-MD and is (slightly) different by construction from the harmonic energy.
Histograms in figure 3.5, represent the energy gap ΔE for 1000 initial conformations (this number gives us a rather good representative statistics) of the $Cl^- \cdots NMA$ complex. We present here the results corresponding to the introduction of the Zero Point Energy (top) and the vibrational excitation $n = 1$ (bottom) in the N-H stretching mode of the $Cl^- \cdots NMA$ complex. In both cases, the quantum semi-classical Wigner distribution are in blue lines whereas the classical distribution are in red.

In practice, our sampling method supplies a set of positions Q_i and momenta P_i for each normal mode depending on the n_i vibrational quantum number in each mode. As described previously in this chapter, in the semi-classical sampling, Q_i are extracted from the Wigner quantum representation, eq 3.19 for n=0 and 3.29 for n=1, and momenta P_i are calculated

from equation 3.31, i.e. $P_i = \sqrt{2E_i - \omega_i^2 Q_i^2}$.
The choice of the initial structures for the dynamics is crucial. After the estimation of the energy gap ΔE, the initial structure for the DFT-MD are chosen carefully in the region which minimize ΔE (i.e. between 2.8 and 3 kcal/mol for $n = 0$ and between 37 and 37.5 kcal/mol for $n = 1$, see in figure 3.5) to be reasonably close to the E_{harm}.

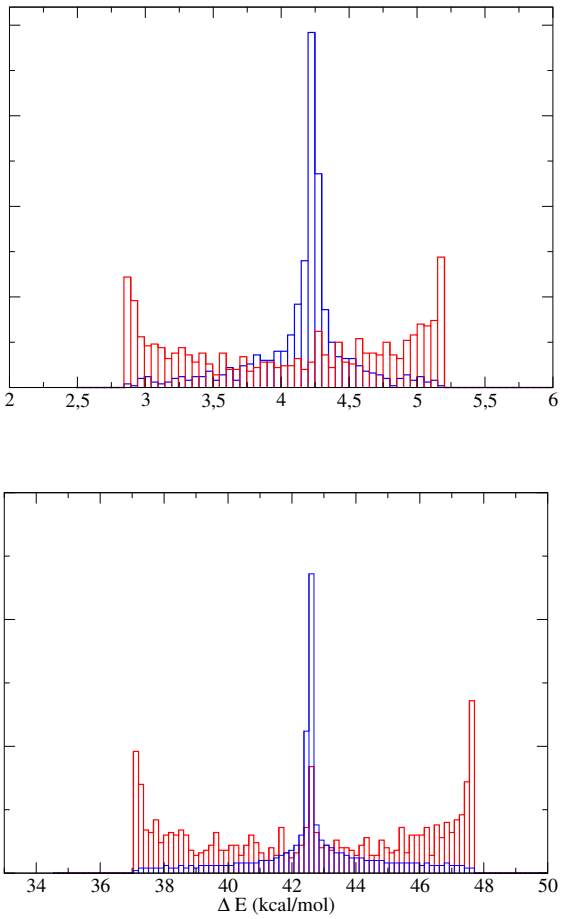

Figure 3.5: Histogram of $\Delta E = E_{actual} - E_{harm}$ for 1000 conformations of the $Cl^- \cdots NMA$ complex. Top: introduction of the ZPE in the N-H stretching mode; bottom: vibrational excitation (n=1) in the N-H stretching mode. The quantum Wigner distribution are in blue lines; the classical distribution are in red.

Chapter 4

Quantum number evolution

Once a molecular dynamics is done in cartesian coordinates, it is useful to follow the evolution of the energies on each subsequent normal modes. This is particularly important for studies related to vibrational activation and energy flow. Previous studies [49, 50, 51] have shown that the analysis of the Instantaneous Normal Modes (INM) is a good tool to monitor the time evolution of the vibrational energy of a molecule in solution after its initial excitation. The INM formalism is based on the fact that, at any instant, each INM is assigned to equilibrium normal modes (ENMs) during the MD simulations. Nevertheless, this procedure is not working very well for molecules in which groups can frequently exchange their position through flat potential energy barrier, as it is the case for the isomerisation of the Formic Acid, for instance. So, we have used two theoretical alternative models to follow the evolution of the quantum number n_i of each mode: a new method based on the study of vibrational density of states (VDOS) compared with a more traditional method based on the study of the amplitude of a specific motion (i.e. distance or angle) of the molecule. First, a short methodology for vibrational spectroscopy and mode assignments is done, then the two methods are detailed and finally compared.

4.1 Theoretical methodology for vibrational spectroscopy and modes assignments

Within Statistical Mechanics and Linear Response Theory (see for instance refs. [52, 53]), an IR spectrum is calculated as the Fourier Transform of the time correlation function of the fluctuating dipole moment vector of the absorbing molecular system as:

$$I(\omega) = \frac{2\pi\beta\omega^2}{3cV} \int_{-\infty}^{\infty} \mathrm{d}t \ \langle \delta\mathbf{M}(t) \cdot \delta\mathbf{M}(0) \rangle \ \exp(i\omega t) \tag{4.1}$$

where $\beta = 1/kT$, T is the temperature, c is the speed of light in vacuum, V is the volume. The angular brackets represent a statistical average of the correlation function, where $\delta\mathbf{M}(t) = \mathbf{M}(t) - < \mathbf{M} >$ with $< \mathbf{M} >$ the time average of $\mathbf{M}(t)$. The calculation in equation 4.1 is done in the absence of an applied external field. For the prefactor in equation 4.1, we have taken here into account an empirical quantum correction factor (multiplying the classical line shape) of the form $\beta\hbar\omega/(1-\exp(-\beta\hbar\omega))$, which provided accurate results on calculated IR intensities ([3, 54, 55]). For more detailed discussions on quantum corrections, see for instance refs. [56, 57, 58, 59].

This is the standard way used in statistical mechanics for calculating the infrared spectrum of molecular assemblies, i.e. isolated molecules, liquids, solutes in the liquid phase, solids, taking into account vibrational anharmonicities and temperature. Molecular dynamics (MD) simulations are adapted for the calculation of the evolution in time of the dipole moment of the system, and therefore its time correlation. The main advantages of the molecular dynamics approach in equation 4.1 for the calculation of infrared spectra (also called dynamical spectra) can be listed as follows.
1) There are no approximations made in equation 4.1 apart from the hypothesis of linear response theory, i.e. a small perturbation from the applied external electric field on the absorbing molecular system. Such condition is always fulfilled in vibrational spectroscopy of interest here.
2) There are no harmonic approximations made, be they on the potential energy surface or on the dipole moment, contrary to static calculations performed in the gas phase community or to Instantaneous Normal Mode Analysis (INM) performed in the condensed phase community.
3) The quality of the potential energy surface is entirely contained in the "*ab-initio*" force field used in the dynamics, calculated in the work presented in this thesis at the DFT/BLYP (+dispersion when needed) level of theory. The good to excellent agreements of the absolute (and relative) positions of the different active bands obtained in different theoretical works (see

for instance dynamical spectra in the gas phase ([60, 61, 62, 2])), in the liquid phase ([3, 63]), and at solid-liquid and liquid-air interfaces, including the SFG spectrum ([4, 64, 6]) shows (though *a posteriori*) that this level of theory is correct.
4) Equation 4.1 gives the whole infrared spectrum of a molecular system in *one single calculation*, i.e. the band positions, the band intensities and the band shapes. There are no approximations applied, in particular the shape and broadening of the vibrational bands result from the underlying dynamics and mode-couplings in the system at a given temperature.

As already emphasized, all studies presented in this thesis employed Born-Oppenheimer dynamics (BOMD). We apply no scaling factor of any kind to the vibrations extracted from the dynamics. The sampling of vibrational anharmonicities, i.e. potential energy surface, dipole anharmonicities, mode couplings, anharmonic modes, being included in our simulations, *by construction*, the application of a scaling factor to the band positions is therefore not required.

An accurate calculation of anharmonic dynamical infrared spectra is one goal to achieve, the assignment of the active bands into individual atomic displacements or vibrational modes is another one. This issue is essential to the understand the underlying molecular structural and dynamical properties. In molecular dynamics simulations, interpretation of the vibrational bands into individual atomic displacements is traditionally and easily done using the vibrational density of states (VDOS) formalism. The VDOS is obtained through the Fourier transform of the atomic velocity auto-correlation function:

$$VDOS(\omega) = \sum_{i=1,N} \int_{-\infty}^{\infty} \langle \mathbf{v_i}(t) \cdot \mathbf{v_i}(0) \rangle \ \exp(i\omega t)\, dt \tag{4.2}$$

where i runs over all atoms of the investigated system. $\mathbf{v_i}(t)$ is the velocity vector of atom i at time t. As in equation 4.1, the angular brackets in equation 4.2 represent a statistical average of the correlation function. The VDOS spectrum provides all vibrational modes of the molecular system. However, only some of these modes will be Infrared or Raman active, so VDOS spectra can by no means directly substitute for IR or Raman spectra.

The VDOS can further be decomposed according to atom types, or to groups of atoms, or to chemical groups of interest, in order to get a detailed assignment of the vibrational bands in terms of individual atomic motions. This is done by restraining the sum over i in equation 4.2 to the atoms of interest only. Such individual signatures are straightforward to interpret in terms of motions for localized vibrational modes that involve only a few atomic groups, typically in the 3000-4000 cm^{-1} domain corresponding to bond stretchings, but the

interpretation of the VDOS becomes more complicated when delocalized vibrations take place through several groups of atoms or when there are couplings between different atomic motions.

Note that other theoretical methods have been developed in order to extract vibrational modes from the dynamics, especially bypassing the limitations of modes delocalization in VDOS assignments, see for instance refs. [1, 65, 66, 67]. Such methods usually provide "effective normal modes", similar to the well-known normal modes obtained by a Hessian diagonalisation in static harmonic calculations, but maintaining a certain degree of mode couplings and temperature effects from the dynamics in the final modes.

4.2 mVDOS

Definition of mVDOS

We have developed an alternative method to the INM to describe the evolution of quantum number n based on the mass vibrational density of states spectrum. This method will be called "$mVDOS$" for short notation.
As we have already seen in the previous section, a VDOS spectrum provides all vibrations of the system. This is a standard method in the dynamical approach to vibrational spectroscopy since it provides all anharmonic modes. We thus want to stick as much as possible to the VDOS methodology in order to extract vibrational quantum numbers from classical (nuclei) trajectories. Such VDOS is calculated in cartesian coordinates. The Fourier transform of the auto-correlation of velocities (VDOS) in cartesian coordinates for N atoms is:

$$I_{vv}(\omega) = \sum_{i=1}^{N} \int e^{-i\omega t} < \vec{v_i}(t)\vec{v_i}(0) > dt \tag{4.3}$$

Note that the unit of such $I_{vv}(\omega)$ is an energy per mass, $I_{vv}(\omega) = \left[\frac{E}{m}\right]$.
To be able to use VDOS to identify a quantum number, one needs a dimension of energy. If we now define :

$$\tilde{I}_{vv}(\omega) = \sum_{i=1}^{N} m_i \int e^{-i\omega t} < \vec{v_i}(t)\vec{v_i}(0) > dt \tag{4.4}$$

coming from the auto-correlation of $\sqrt{m_i}\vec{v_i}(t)$, one then recovers a dimension for $\tilde{I}_{vv}(\omega)$ of energy. This is what will be called afterwards **mVDOS**.

Our goal here is to find a relation between the Fourier Transform (FT) of the auto-correlation time function of the mass-weighted normal mode momentum and the energy of each peak of the mVDOS thanks to the equations 3.4, 3.8, 3.9, 3.10. In mass-weighted coordinates, we can define the auto-correlation time function $C_{P_\alpha P_\alpha}(t)$ of the mass-weighted normal mode momentum P_α (where α indexes a given normal mode) as:

$$\begin{aligned} C_{P_\alpha P_\alpha}(t) &= \langle P_\alpha(t) P_\alpha(0) \rangle \\ &= \omega_\alpha^2 A_\alpha^2 cos(\omega_\alpha t + \psi)\cos(\psi) \end{aligned} \tag{4.5}$$

we can set the phase to zero such that

$$C_{P_\alpha P_\alpha}(t) = \omega_\alpha^2 A_\alpha^2 cos(\omega_\alpha t) \tag{4.6}$$

The Fourier transform of $C_{P_\alpha P_\alpha}(t)$ is:

$$I_{P_\alpha P_\alpha}(\omega) = \omega_\alpha^2 A_\alpha^2 \int e^{-i\omega t} cos(\omega_\alpha t) dt = \omega_\alpha^2 A_\alpha^2 \pi[\delta(\omega - \omega_\alpha) + \delta(\omega + \omega_\alpha)] \tag{4.7}$$

where we use the following definition for Fourier transform:

$$\int e^{-i\omega t} cos(\omega_\alpha t) = \pi[\delta(\omega - \omega_\alpha) + \delta(\omega + \omega_\alpha)] \tag{4.8}$$

such that, $I_{P_\alpha P_\alpha}(\omega)$ has the same dimension of $\omega_\alpha^2 A_\alpha^2$ ($\omega_\alpha^2 A_\alpha^2 = \omega_\alpha^2 . (\frac{\sqrt{2E_\alpha}}{\omega_\alpha})^2 = 2E_\alpha$) which corresponds to an energy.
The spectrum of one normal mode momentum is thus composed of 2 Dirac peaks, located respectively at $\omega = +\omega_\alpha$ and $\omega = -\omega_\alpha$, as schematically shown in figure 4.1 with the blue vertical lines. Each peak has an intensity of $\omega_\alpha^2 A_\alpha^2 \pi$.

When all normal modes are taken into account, the vibrational harmonic spectrum has therefore the following expression:

$$I_{PP}(\omega) = \sum_{\alpha=1}^{3N-6} \omega_\alpha^2 A_\alpha^2 \pi[\delta(\omega - \omega_\alpha) + [\delta(\omega + \omega_\alpha)] \tag{4.9}$$

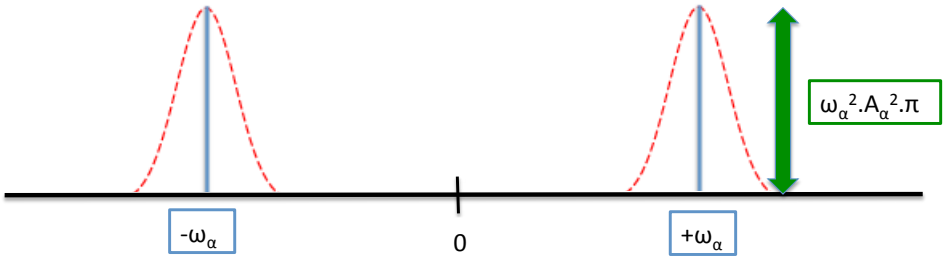

Figure 4.1: Comparison of the harmonic spectrum composed with 2 Dirac peaks (in blue) and the anharmonic spectrum composed of broadened peaks (in dotted red linges) departing from the dirac harmonic peak. Each Dirac peak has an intensity of $\omega_\alpha^2 A_\alpha^2 \pi$.

which is composed of (3N-6) Dirac peaks ($\omega > 0$).

Quantum number from MD

In our dynamics, the motion of the oscillators constituting the modes is not harmonic. A first consequence is the broadening of peaks departing from the dirac harmonic peaks as we can see in the illustrative red dashed lines in figure 4.1. Furthermore, ω_α will be red or blue shifted, due to anharmonicites and mode couplings. Although our dynamics are not harmonic, here we make an assumption that will be our working hypothesis : for one given mode assigned in the mVDOS spectrum, corresponding to one vibrational band, we assume that its integral $I_{vv}(\omega)$ is equal to the intensity $I_{P_\alpha P_\alpha}(\omega)$ of the underlying harmonic mode. This approximation is reasonable for high frequency motions (in our case we will consider $> 3000\ cm^{-1}$) because even if such modes are anharmonic (i.e, O-H, C-H and N-H stretches) they are well localized. Assignment is another problem (here the peak can be easily assigned). From the mVDOS and the Fourrier Transform we obtain the integral of each peak. We also know that in the harmonic approximation, the energy E_ω for each mode ω_α is $E_{\omega_\alpha} = (n_\alpha + \frac{1}{2})\hbar\omega_\alpha$ so:

$$I_{P_\alpha P_\alpha}(\omega) = \omega_\alpha^2 A_\alpha^2 \pi = 2E_{\omega_\alpha}\pi \tag{4.10}$$

The quantum number n_α is obtained from the integral $\tilde{I}^\alpha_{vv}(\omega)$ of the band of the corresponding mode ω_α.

$$2E_{\omega_\alpha}\pi = \tilde{I}^\alpha_{vv}(\omega) = 2\pi(n_\alpha + \frac{1}{2})\hbar\omega_\alpha \tag{4.11}$$

$$n_\alpha = \frac{\tilde{I}^\alpha_{vv}(\omega)}{2\pi\hbar\omega_\alpha} - \frac{1}{2} \tag{4.12}$$

where, now ω_α is the frequency obtained at the center of the vibrational band associated to the mode α, from the anharmonic mVDOS spectrum calculated with the molecular dynamics trajectory. $\tilde{I}^\alpha_{vv}(\omega)$ is the integral of the α vibrational band which was calculated numerically.

Before proceeding, we should pause and discuss the underlying approximation employed in the vibrational quantum number obtained from mVDOS. The mVDOS spectrum contains and reflects the anharmonicities present in simulations in terms of position (ω_α), shape, width and intensity of the bands. The calculation of the integral of the band includes, in fact, the vibrational anharmonicities. Our only hypothesis in this method is the use of the harmonic

expression of the energy E_α and its relation to n_α in the harmonic approximation for a vibrational mode α. This is a reasonable hypothesis and it fits well since we want to follow the evolution of vibrational excitation.
In conclusion, even if the expression of the energy E_α is harmonic, the integral associated to the vibrational band takes into account the anharmonicities arising from the dynamics. The quantum number n_α extracted from the MD contains the anharmonicites of the dynamics and as such can be considered as an effective anharmonic quantum number.

4.3 Extraction of mVDOS

mVDOS have to be calculated in order to extract n_α of each mode. From the definition of the Fourier Transform and the auto-correlation function with time (equations 4.8 and 4.5) we have to define a time window to obtain mVDOS and calculate properly the quantum number n_α. Since we want to follow the evolution of n_α during an MD simulation, this means that we have to find a good time window for which the mVDOS is converged; once this is done, we will divide our full trajectories in subsets and calculate mVDOS and n_α on these sets. The first step is thus to evaluate a correct time window. In figure 4.2 we show the mVDOS spectra calculated for different time window: 25 fs, 50 fs, 100 fs, 250 fs, 500 fs, 1 ps, 2 ps and 5 ps from top left to bottom right.

As we can see in figure 4.2, the mVDOS spectra for time intervals of 25 fs and 50 fs (panels a-b) are not defined al all: one can not distinguish any vibrational band. The 100 fs and 250 fs (panels c-d) spectra show two large bands but are not well defined. The spectrum calculated with a resolution of 500 fs (panel e) shows 4 vibrational bands (i.e the O-H and C-H stretching can now be distinguished). The 1 ps spectrum (panel f) is very similar to the previous spectrum but the vibrational bands are better resolved and one can now distinguish 5 peaks. If we increase the resolution of the mVDOS spectra to 2 ps and 5 ps (panels g-h), one can see that these spectra are not very different from the 1 ps spectrum in terms of position of peaks.
We therefore have chosen a 1 ps time-frames to study the quantum number evolution. This implies that we cannot follow the phenomena occurring under the picosecond time-scale. In our case we are interested in the $Trans - Cis$ isomerisation of the Formic Acid molecule. In chapter 5, we will show that this process can occur in less than one picosecond. Thus, we

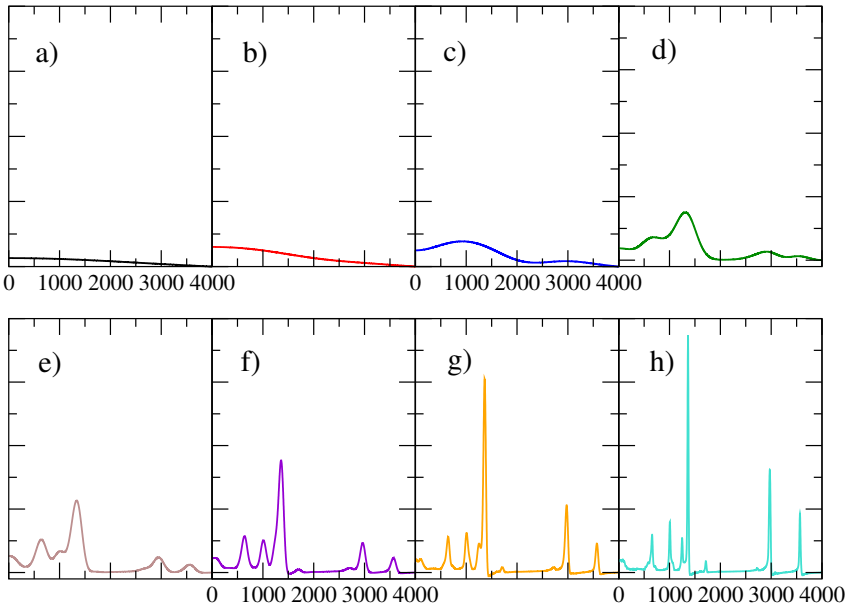

Figure 4.2: Vibrational density of states calculated with mass (mVDOS) for 25 fs (a; in black), 50 fs (b; in red), 100 fs (c; in blue), 250 fs (d; in green), 500 fs (e; in brown), 1 ps (f; in purple), 2 ps (g; in orange) and 5 ps (h; in cyan) dynamics.

need another method to extract the quantum number n_i from our molecular dynamics with a smaller time window. This method is presented in the next section.

4.4 Amplitude method

In this section, a "classical" method to follow the quantum number with a shorter time-window n_i is presented: From equation 3.5, the quantum number n_i is calculated as :

$$n_i = \frac{E_i}{\hbar\omega_i} - \frac{1}{2} \tag{4.13}$$

In the harmonic approximation the mass-weighted amplitude of motion A_i (equation 3.10)

and its non mass-weighted value A'_i are :

$$A'_i = \frac{A_i}{\mu_i} = \frac{(2E_i)^{(1/2)}}{\omega_i \sqrt{\mu_i}} \tag{4.14}$$

where μ_i is the reduced mass of mode i. It can be obtained by Hessian diagonalisation. The reduced mass μ_i for the vibrational mode is calculated with the following expression:

$$\mu_i = \left(\sum_k^{3N} l^2_{CARTk,i} \right)^{-1} \tag{4.15}$$

with $l_{CARTk,i} = \sum_j^{3N} \left(\frac{D_{k,j} L_{j,i}}{\sqrt{m_k}} \right)$. Both D and L are matrices which transforms from mass weighted cartesian coordinates to internal coordinates for N normal modes.
In equation 4.14, the frequency ω_i is calculated with the period (T_i) of the signal. Indeed, $T_i = \frac{2\pi}{\omega_i}$.
We can follow in time A'_i from the dynamics during short period of time ($\approx$ 100 fs) which corresponds approximately to 10 periods of oscillations (that is enough to calculate the average of T_i on this time-scale) as we can see in figure 4.3:

From the amplitude A'_i of mode i, we can deduce the energy E_i of the mode with equation 4.14 and the quantum number n_i with equation 4.13.

4.5 Conclusions

The two methods have pros and cons that we resume in what follows.

1) **Definition of the modes**: mVDOS does not need any definition, while the amplitude needs it. In the mVDOS method the energy flow can be followed even if we do not know anything about the molecular origin of each mode. This is an advantage but also a limitation. If we are interested in mode assignment other techniques are necessary. On the other hand, the amplitude method is quite straightforward from cartesian coordinates dynamics if we deal with well localized stretching modes (for instance C-H and N-H) but we need to know and define geometrically the mode in advance.

2) **Time-window**: In the mVDOS method, the vibrational quantum number can be followed with a 1 ps time window which is a relatively good time window to study the relaxation

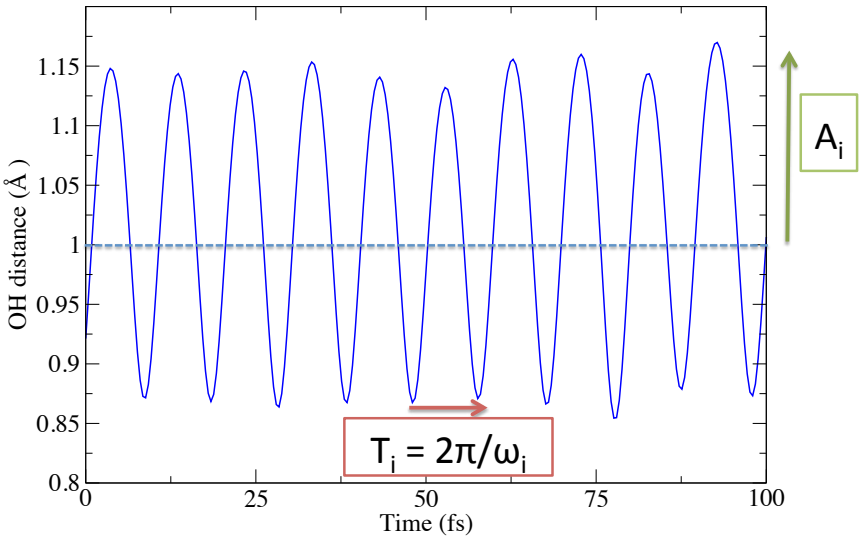

Figure 4.3: Evolution of the O-H distance of the Formic Acid for 100 fs.

of energy in our system. In the amplitude method, the time window is 100 fs. It is efficient to follow the phenomena occurring under the picosecond (i.e $Trans - Cis$ isomerisation of FA).

3) **Weak point**: mVDOS cannot separate the peaks for low frequency modes such as bending or wagging (O-H wagging , C-H wagging and O-C=O bending, for formic acid in the low frequency domain below 1000 cm^{-1}) and so we cannot easily give the correct mode assignment. In the amplitude method, the modes have to be defined geometrically in advance and this cannot be done easily for certain modes.

Chapter 5

Vibrational dynamics of Formic Acid embedded in an argon matrix.

5.1 Introduction

We present here the study of conformational isomerization of a host molecule -a simple carboxylic acid, formic acid (FA)- in a rare-gas matrix. This system provides a simple model to understand the reactivity of biologically relevant molecular systems, where the conformational properties of the carboxylic group play an important role [68, 69, 70, 71]. Small carboxylic acids are frequently used as model compounds to study a variety of chemical phenomena. To have an idea of how exhaustively the Formic Acid molecule has been studied we can do a simple search in the *ISI Web of Knowledge* (http://isi15.isiknowledge.com/) for scientific papers containing the name of one of the studied molecules in the title. This search will give 90 papers a year containing the words formic acid in the title. Simple organic molecules like carboxylic acids are also compounds of astrophysical interest. FA has already been detected in the interstellar medium [72, 73]. One of the theories of formation of life on Earth believes that the known interstellar organic molecules could have been important in prebiotic synthesis once delivered to the early Earth by impact with asteroids and comets. Conformational analysis is also important in this active field of research for the presence in the interstellar space of larger organic molecules. One should know which conformer to look for and how the possible stable geometries of the searched molecules can be characterized spectroscopically [74]. Inter-

estingly, IR-absorption spectroscopy of matrix isolated polyaromatic hydrocarbons has been used by the NASA-Ames Research Group to create a basis set of spectrocopically relevant data to access the presence of this type of molecules in the interstellar space by comparison with astronomic data.

The particular choice of the molecular systems studied takes advantage of the experiments conducted by the group of Prof Rasanen [75, 76, 77] or Fausto *and coll.* [78] at the University of Helsinki in Finland and our theoretical investigations are conducted in collaboration with the group of Prof Benny Gerber (FiDiPro Professor at the Helsinki University at the time of start of this investigation).

Conformational properties of carboxylic acids.

It is widely acknowledged that the carboxylic adopt preferentially a planar geometry, with two stable arrangements differing by internal rotation about the C-O bond, as presented in figure 5.1. Generically, for carboxylic acids, these two stable arrangements can be denoted by trans and cis geometries, for R1-C-O-R2 dihedral angles of 180 and 0 degrees, respectively. Unless specific interactions like intramolecular hydrogen bonding or strong electrostatic interaction between the R groups are active, the conformational ground state exhibits a trans arrangement. An illustrative example of specific interactions stabilizing the cis arrangement can be found in some dicarboxylic acids, where strong intramolecular hydrogen bonds make the cis geometry the conformational ground state. [79, 80, 81, 82, 83] The origins of the energy difference and internal rotational barriers in carboxylic acids have been analyzed to some extent by theoretical studies. The computationally predicted relative energies and energy barriers between the two arrangements are similar for simple carboxylic acids and esters, where the R groups are either hydrogen or small alkyl groups. The cis arrangement is predicted to be higher in energy by 1700-3000 cm^{-1} (20-35 kJ/mol) and the barrier heights lay within the 4300-4600 cm^{-1} (50-55 kJ/mol) range. [84, 85, 86, 87] It is thought that the main reason for the lower energy of the trans arrangement lays in the stabilizing effect of a nearly antiparallel alignment of the C=O and O-R2 bond dipoles and the existence of more relevant steric and electrostatic repulsions between the R groups destabilizing the cis arrangement. The relevance of these two factors can be supported by the lower total dipole moments and the smaller R1-C-O angles for the trans geometry as compared to the cis one [84].

The small molecular size of Formic Acid (FA = $HCOOH$) makes it attractive to computational modeling. FA is particularly interesting because it is the simplest organic acid

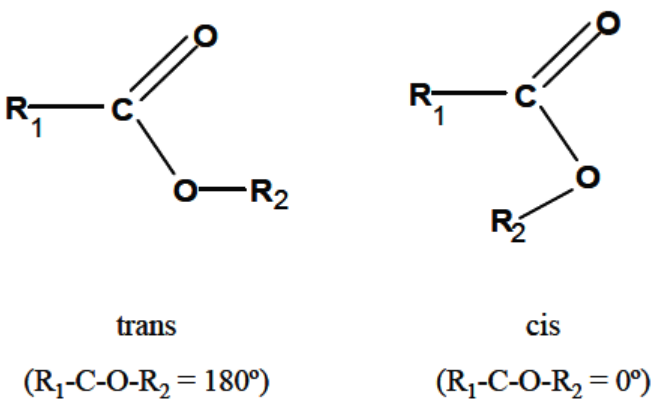

Figure 5.1: Stable arrangements of carboxylic (R2=H for FA) group with respect to rotation around the C-O bond. Labeling of trans/cis isomers

exhibiting rotational isomerism. The calculation of energies, structures and fundamental vibrational modes of the two trans/cis conformers have been reported using fairly sophisticated methods (e. g. Configuration Interaction with Single and Double excitation (CISD) [88] and Moller-Plesset to the forth order (MP4) [89]) with relatively large basis sets. On the other hand, the characterization of the structure of this molecule by experimental methods has not been so successful. The trans conformer has been extensively studied experimentally, but very little is known about the cis conformer. There have been many unsuccessful attempts to detect cis-Formic Acid (see for instance ref [90]). The first unequivocal identification of cis-FA were made by Hockings and Bjarnov using microwave spectroscopy. [91, 92] From these studies a relative energy difference with respect to the *trans*-FA of 1365 cm^{-1} and a barrier height of 4852 cm^{-1} have been estimated. The lack of experimental data on the cis conformer is not surprising, considering that its relatively high conformational energy leads to a Boltzman population ratio at room temperature of Pcis/Ptrans $\simeq 10^{-3}$.

A convenient approach is the investigation isomerization of a host molecule (Formic Acid as our first example) embedded in an inert argon matrix.

Rare-gas matrix isolation.

Matrix isolation is now a well established sampling technique, where the molecules of the compound to be studied (guests) are preserved at very low temperature and concentration

in a solid medium (host). The idea of investigating atoms and molecules in inert cryogenic matrices emerged in the 50's by Pimentel and coworkers. [93] By then, the emphasis was on the spectroscopic investigation of transient species isolated in rare-gas matrices (e. g. Ne, Ar, Kr, Xe). The effective transparency to radiation of rare-gas matrices, going from the far-IR to vacuum-ultraviolet (VUV), combined with the lack of appreciable diffusion of the isolated species at these low working temperatures, suppressing bimolecular reactions, and the relatively weak guest-host interactions, fueled the use of this technique in the study of transient species. Molecules with very short lifetimes in fluid conditions are stable in rare-gas matrices in their ground electronic state and could be studied by a variety of spectroscopic methods. Several reviews and books have been published on the topic showing many interesting applications of matrix-isolation spectroscopy, [94, 95, 96, 97, 98, 99, 100] and also giving the practical details necessary to build a matrix-isolation laboratory from scratch. [101] Soon it was realized that rare-gas solids do not really constitute an inert medium. It is true that on average the perturbations suffered by the trapped species are relatively small, as illustrated by the shift between the matrix vibrational frequencies and the gas phase data (typically of 2 percent), but by no means negligible. These matrix induced shifts can be very significant for vibrational modes with high transition dipole moment. [72, 102]

Vibrational spectroscopy in low-temperature rare-gas matrices is a very commonly used method in the study of conformational isomerization due to the possibility of trapping the less stable conformers by preventing induced isomerisation. The trapping of small molecules in a rare gas matrix (see Fig 5.2) has been simulated with method based on classical molecular dynamics by Crépin *et al.* [103]. The rigidity of the matrix cage has an additional advantage for vibrational spectroscopy, connected with the suppression of rotational motion for most of the molecules (bigger than water). Elimination of the rovibrational structure simplifies the spectra in comparison with gas-phase spectra and makes their interpretation easier when based on commonly available spectral simulation tools.

Summarizing, we want to simulate the vibrational absorption of energy that corresponds to the experimental set-up used by the group of Prof. Markku Räsänen [76, 75, 77, 104] at the University of Helsinki, Finland, i.e, vibrational excitation through combination bands of a Formic Acid (FA) molecule (for instance the combination of the O-H stretch and the C-O-H "skeleton" deformation) embedded in an argon matrix. The host molecule is vibrationnally excited while the argon matrix remains in its ground vibrational state (no vibrational excitation for argon).

In the experiment, formic acid molecules are trapped in an argon matrix at a very low temperature of ∼8 K. Using tunable infrared (IR) radiation, selective excitation of various vibrational modes of the lower-energy *trans* conformer of the FA in the range 7000 to 2900 cm^{-1} is applied. The assumption is that upon such vibrational excitation, the initial *trans* conformer of FA will isomerize into its *cis* conformer, as the vibrational excitation chosen in the experiment is enough to overcome the energy barrier separating these two conformational isomers. The *trans-cis* isomerization quantum yield for the excited modes has been found experimentally. Quantum yields up to 40 % at excitation energies above the isomerisation barrier were obtained. In particular, the quantum yield of isomerization after the excitation of the O-H stretch and the O-H wagging (C-O-H "skeleton" deformation) is found around 21 %.

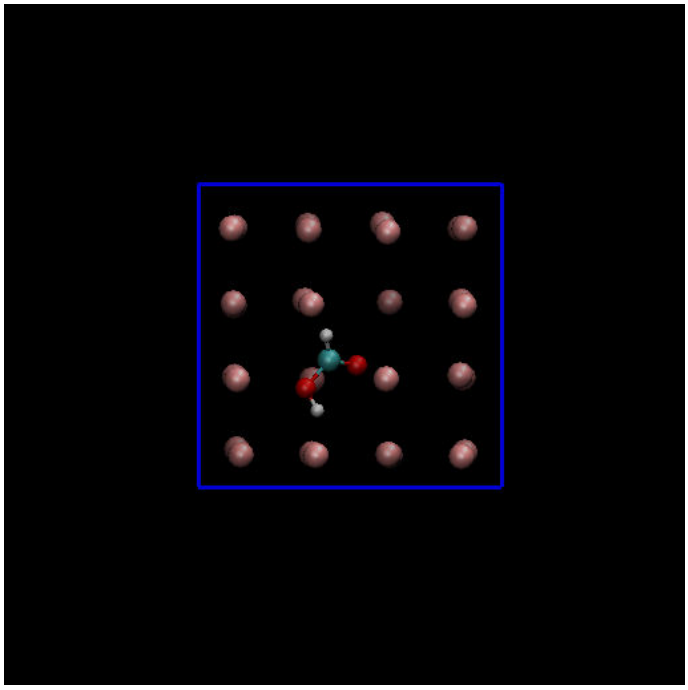

Figure 5.2: Snapshot of trans-Formic Acid (Trans-FA) embedded in an Argon matrix in our DFT-MD set-up. The main cell is presented here and is composed of 29 argon atoms in a cubic cell of 10.74 Å box-length. This volume is compatible with the density of argon at low temperature.

Our questions

Formic Acid is embedded in an argon matrix (it could also be a N_2 matrix, these experiments have been done by the same group in Finland). Combination bands (i.e for instance O-H stretching and wagging) of FA are vibrationally excited, and the isomerization from trans-FA to cis-FA can be observed with a certain efficiency (or yield). The $Trans/Cis$ isomerization depends on the energy provided to the molecule by the vibrational excitation, i.e. whether the energy provided to the FA molecule is above (or not) of the trans-cis isomerization. At least, the energy has to be present in the system (unless tunneling is at play for the isomerization to occur). The fact that yields measured experimentally [75, 76, 77] are not of 100%, even far from it (usually more like 20% for the most efficient isomerization mechanisms), shows that even if the host molecule possesses enough energy, it is not 100% sure that the isomerization between the two conformations will proceed.

The questions we want to address in our theoretical investigation are the following:

- We want to simulate the vibrational absorption of energy that corresponds to the experimental set-up, i.e. vibrational excitation through combination bands (for instance the combination band of the O-H stretch and the C-O-H "skeleton" deformation) of the host Formic Acid molecule. The host molecule is vibrationnally excited while the argon matrix remains in its ground state (i.e. no vibrational excitation for argon).
- Once this is done for the initial conditions, we follow the evolution with time of the whole system, i.e. host FA + surrounding argon marix, by DFT-based molecular dynamics simulations.
- The issues are to understand how the initial vibrational energy deposited within the FA host molecule is redistributed within the host molecule, corresponding to intra-molecular vibrational relaxation and how/if the energy can flow from the host molecule to the surrounding argon matrix, thus corresponding to inter-molecular vibrational relaxation. In this case, we want to measure the amount of energy flow, what are the mechanisms for this flux of energy, what are the modes involved, what are the consequences of the energy flow to the surrounding matrix (heating of the matrix for instance) and what are the time-scales for the energy flow.
- What are the mechanisms for the *trans*-to-*cis* isomerization process of FA conformation in the matrix. One other question is whether the surrounding matrix plays a role in this isomerization, and to characterize this role as precisely as possible.
- Can we compare the isomerisation yield obtained from simulations with the experimental one, as a function of the modes initially excited We will apply DFT-MD simulation using initial

conditions as discussed in the chapter 3 for following the energy flow through the modes.

5.2 DFT-MD and argon-argon dispersion interactions

An important aspect of DFT-MD simulations will be the interaction potential, and a particular care should be devoted to the Ar-Ar interactions. At this end, we have first compared the BLYP-D3 method, used in the dynamics, with respect to higher level quantum chemistry calculations. To that end, the potential energy profile of the Ar$\cdots$Ar dimer (2 body interactions), relative energies of argon tetramers (N-body interactions), and structural properties of an argon matrix have been investigated.

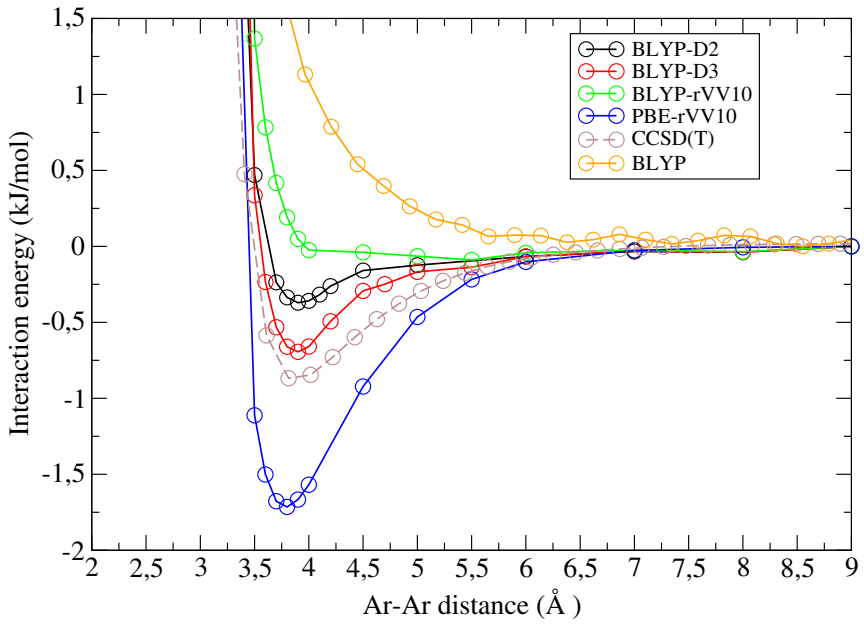

Figure 5.3: Potential energy surfance for the Ar-Ar dimer computed with CCSD(T) (in brown), PBE+rVV10 (in blue), BLYP (in orange), BLYP with D2 correction for dispersion (in black), BLYP with D3 correction for dispersion (in red), and BLYP +rVV10 (in green). The energies are in kJ/mol.

In figure 5.3, the reference potential energy profile of Ar_2 is calculated at the CCSD(T)/aug-

cc-pVTZ level, to which are compared the profiles obtained with the all-electron BLYP-D2 [32], BLYP-D3 [34], and rVV10 (with BLYP), rVV10 (with PBE) [105] representations. DFT calculations are done with the same aug-cc-pVTZ basis set. The well depth for Ar-Ar is very shallow with an energy of only -0.9 kJ/mol at the CCSD(T) level of representation. One can observe that the BLYP-D3 energy profile is in very good agreement with the reference (the well depth is located at -0.8 kJ/mol), while the BLYP-D2 profile underestimates the well depth, and the PBE-rVV10 profile overestimates it. The BLYP-rVV10 profile does not show any clear defined well-depth and the BLYP functional provides a dissociative profil (and thus it will not be further presented). The PBE-rVV10 level of representation overestimates the well depth (-1.75 kJ/mol). The Ar_2 equilibrium distance is obtained at 3.8 Å in all profiles displaying the attraction well. One is thus rather confident in the BLYP-D3 representation to provide the Ar-Ar 2-body interaction rather correctly.

The geometries of four different Ar_4 structures have been subsequently optimized and their relative energies are presented in Table 5.1, in order to test N-body interactions on simple clusters. The geometries of the tetramers are schematically shown in figure 5.4. Relative energies in Table 5.1 are calculated with respect to the 'pyramid' structure which is of lowest energy at all levels of calculation tested here. Calculations are done at CCSD(T)/aug-cc-pVTZ, BLYP, BLYP+D2 and BLYP+D3 levels of representation (all with the aug-cc-pVTZ basis set).

Geometry	CCSD(T)	BLYP-D2	BLYP-D3
square	+0.43	+0.14	+0.29
node	+0.75	+0.27	+0.31
align	+0.77	+0.29	+0.53

Table 5.1: Relative energies of argon tetramers comparing the CCSD(T)/aug-cc-pVTZ reference values with BLYP-D2 and BLYP-D3 representations are presented. The energies are calculated in kJ/mol with respect to the energy of the 'pyramid' structure. See figure 5.4 for geometries.

Relative energies between these structures are extremely tiny, as anticipated, but one can still observe that dispersion is necessary in order to distinguish the energy of each isomer, and the BLYP-D3 relative energies are the closest to the reference CCSD(T) values, although systematically underestimating the reference energies.

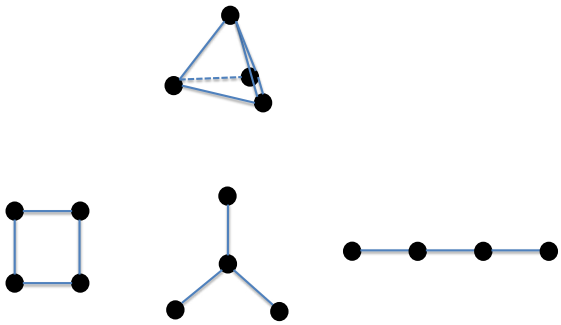

Figure 5.4: Schematic representation of the four Ar_4 tetramer structures investigated for the relative energies presented in Table 5.1. They are called 'pyramid' (top), 'square' (bottom left), 'node' (bottom center), 'align' (bottom right).

The next checking step concerns the representation of an argon matrix, and to that end we have run DFT-MD/BLYP-D3 dynamics of a fcc (face centered cubic) matrix composed of 32 argon atoms (with a cubic length of 10.7 Å) at different temperatures (from 20 to 150 K). Ar-Ar radial pair distribution functions (RDF, g(r)) from simulations for five different temperatures are presented in figure 5.5. The trajectories are systematically started from the 0 K fcc matrix, an equilibration of 4 ps is performed and results are presented on the subsequent 12 ps dynamics (in the NVE ensemble). Note that DZVP-GTH Gaussian basis set from the MOLOPT of the CP2K package database and plane-waves of 340 Ry are used for the DFT-MD trajectories. We have checked that results are not changed when simulating a box of 108 argon atoms.

One can see that the peaks of the g(r) are respectively located at 3.8 Å, 5.3 Å, 6.5 Å and 7.4 Å, which indeed corresponds to an fcc matrix organisation. For the two lower temperatures (20 K and 40 K), the RDFs go to zero in-between successive peaks, which reflects a solid matrix. At 80 and 100 K, one can observe the onset of a more "liquid-like" behavior, as the intensities

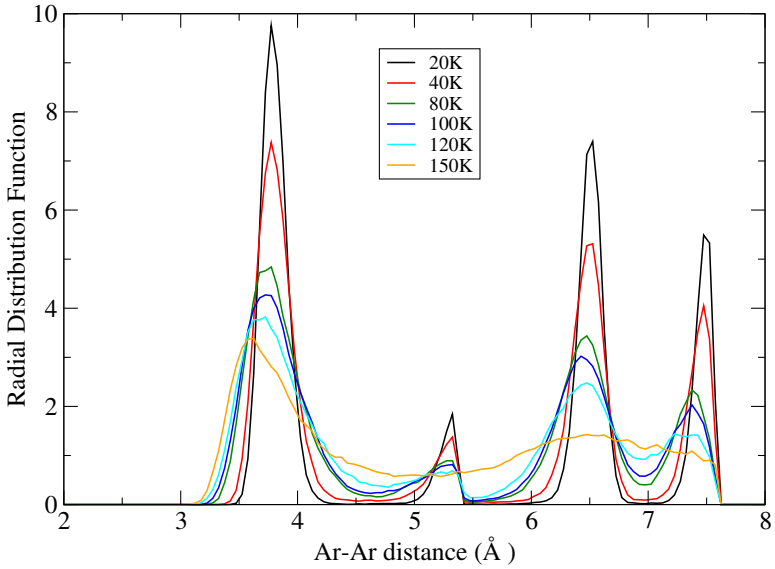

Figure 5.5: Radial pair distribution functions (RDF) of Ar-Ar from DFT-MD/BLYP-D3 simulations of a 32 fcc argon matrix at different temperatures.

of the peaks are decreased and RDFs in-between peaks depart from zero. Note however that the melting temperature of argon is experimentally known at 80 K, while our DFT-MD at 100 K does not fully reflect such melting state, at least using RDF as criterium. The 80 K and 100 K RDFs indeed are not totally representative of a liquid state, they only show the onset of it. When the temperature is varied across 120 K and 150 K, the RDF changes abruptly, the structure of the argon matrix is lost, the long-range order of the RDF becomes faint, showing that the argon system turns into liquid-like disorder.
To substantiate this last statement, one can also extract the Lindemann coefficient [106, 107] from our simulations, defined as follows:

$$\Delta_L(t) = \frac{\sqrt{\sum_j < \Delta r_j^2(t) > /N}}{a'} \tag{5.1}$$

where N is the number of atoms, a' is the most probable non-bonded near-neighbor distance between argon atoms, $\vec{r}_j(t)$ is the position of atom j at time t of the trajectory,

$\Delta r_j^2(t) = \| \vec{r}_j(t) - < \vec{r}_j(t) > \|^2$ is the root mean square (rms) fluctuation in atomic positions, and <> denotes configuration average. In our case, $a' = 3.8$ Å, i.e the equilibrium distance between two argons. The Lindemann coefficient has been calculated between $t = 0$ and t_{max} along the trajectories (with $t_{max} = 1, 2, ...12\ ps$) and the results are plotted in figure 5.6, as a function of time. The results of experiments and simulations have shown that the transition from solid to liquid can be considered to occur when a value of $\Delta_L(t) = 0.15$ is reached [108, 109, 107]. This value is represented by the horizontal dashed line in figure 5.6.

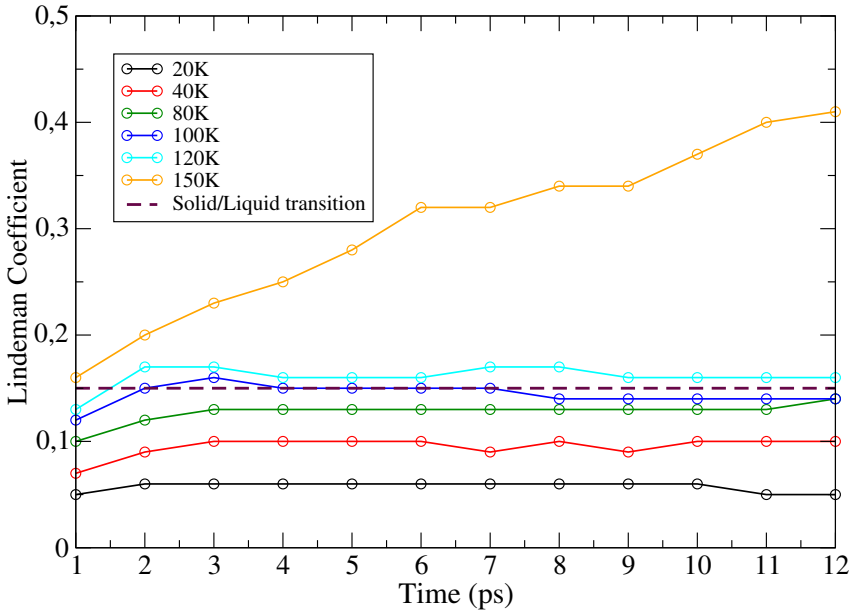

Figure 5.6: Lindemann coefficient of Ar-Ar, calculated as a function of time, from DFT-MD/BLYP-D3 simulations of 32 fcc argon matrix at different temperatures. The horizontal dashed line represents the $\Delta_L(t) = 0.15$ used for the appearance of the solid to liquid transition.

For our argon matrix we see that, at the two lower temperatures (20 K and 40 K), the argon matrix is clearly of solid state nature, while at 80 K and 100 K, the Lindemann coefficient is very close to the one for the solid-liquid transition. At the two higher temperatures (120 K and 150 K), the Lindemann coefficient corresponds to a liquid-like state, which appears after few picoseconds of dynamics. We thus find that the solid-liquid transition for the BLYP-D3

fcc argon matrix is roughly at 100 K.

5.3 Vibrational spectroscopy of Formic Acid

In the previous section, we have shown that the BLYP-D3 calculations give a correct representation for the Ar-Ar 2-body interaction, relative energies between different structures of Ar_4 tetramers and for a matrix. Next step in validating the DFT-MD set-up is to test the BLYP-D3 electronic representation and its ability in producing correct theoretical vibrational spectra for the formic acid (FA) molecule in the gas phase and embedded in the matrix.

In molecular dynamics simulations, interpretation of the infrared active bands into individual atomic displacements is traditionally and easily done using the vibrational density of states (VDOS) formalism (see in chapter 4). The VDOS is obtained through the Fourier transform of the atomic velocity auto-correlation function:

$$VDOS(\omega) = \sum_{i=1,N} \int_{-\infty}^{\infty} \langle \mathbf{v_i}(t) \cdot \mathbf{v_i}(0) \rangle \ \exp(i\omega t)\ dt \tag{5.2}$$

where i runs over all atoms of the investigated system. $\mathbf{v_i}(t)$ is the velocity vector of atom i at time t. The angular brackets in equation 5.2 represent a statistical average of the correlation function. That is the signal that we calculate here, providing all vibrations active in IR or Raman spectroscopies.

Vibrational density of state (VDOS) for the *Trans*-formic acid in the gas phase was obtained at different levels of theory: B97D, BLYP, BLYP-D2 and BLYP-D3. The results are plotted in figure 5.7 where all spectra are presented with the same intensity scale. The trajectories are systematically thermalized during 4 ps and then accumulated in a pure NVE ensemble during 10 ps. The average temperature of these trajectories is 20 K. The experimental frequencies are reported in table 5.2, compared with DFT-MD/BLYP-D3 results to be coherent with the Ar-Ar interactions.

B97D representation fails to reproduce the experimental spectrum for the formic acid in the gas phase since several bands are shifted (by 100 cm^{-1} for the O-H stretching and by 50 cm^{-1} for the C-H stretching), while the BLYP, BLYP-D2 and BLYP-D3 do better as we can see in figure 5.7 especially in the zoomed spectrum in figure 5.8. After comparison of band

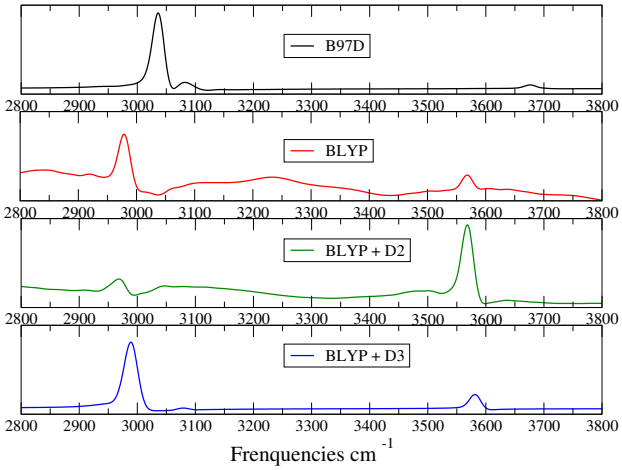

Figure 5.7: Vibrational Density of States (VDOS) of gas phase formic acid (FA) using different electronic representations: B97D (black), BLYP (red), BLYP+D2 (green), BLYP+D3 (blue).

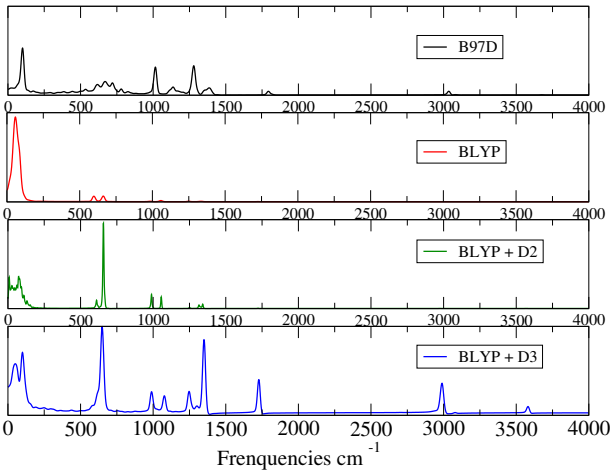

Figure 5.8: This is the same as figure 5.7 zoom in the 2800-3800 cm^{-1} region.

positions with the gas phase experimental data of Bertie et al. [110], we found that BLYP-D3 matches very well with the experimental results, while BLYP and BLYP-D2 functionals fail

to reproduce the experimental data especially for the low frequencies.

Mode assignment	Experiment	DFT-MD/BLYP-D3
O-H stretching	3569	3580
C-H stretching	2942	2988
C=O stretching	1777	1733
C-H bending	1381	1350
O-H bending	1223	1248
C-O stretching	1104	1080
C-H wagging	1033	992
O-H wagging	642	662
O-C=O bending	625	647

Table 5.2: Experimental [110] and DFT-MD/BLYP-D3 (VDOS) frequencies (cm^{-1}) of *Trans*-formic acid calculated at 20 K for 10 ps.

When comparing the VDOS of the gas phase FA with FA embedded in the matrix (shown in figure 5.9), we find that the matrix environment has no significant effect on the position of the vibrational peaks of the formic acid molecule, apart from a 15 cm^{-1} blue shift of the ν(C-H).

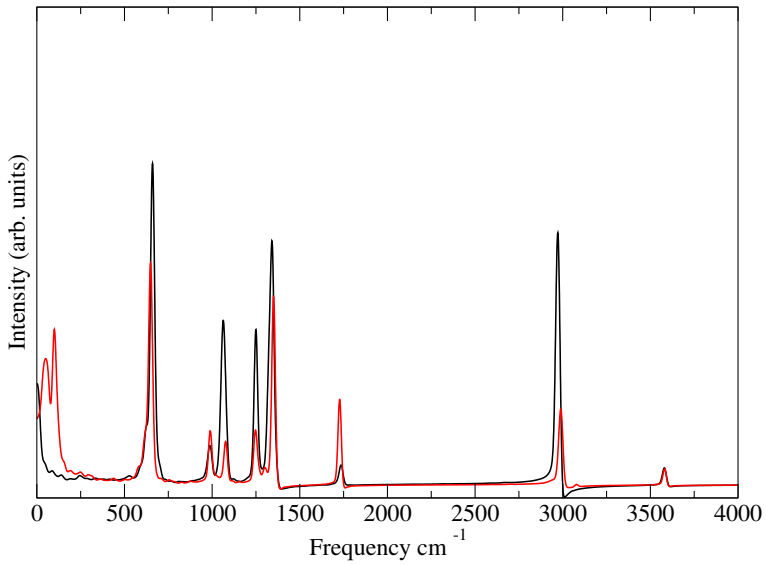

Figure 5.9: Vibrational Density of States (VDOS) of formic acid (FA) molecule in the gas phase (black) and inserted in an argon matrix (red).

5.4 Potential Energy Surface (PES) of the Formic Acid in the gas phase

Before study the isomerisation of FA in the matrix via molecular dynamics simulation, we have studied the isomerisation by state calculations. The potential energy surface (PES) of the formic acid molecule is calculated at BLYP-D3 level of theory and compared with CCSD(T) calculation. The aug-cc-pVTZ basis set is used in both. The BLYP-D3 energies are in very good agreement with the CCSD(T) reference values, which validates once more the BLYP-D3 electronic representation for the system of interest, as shown in figure 5.10.

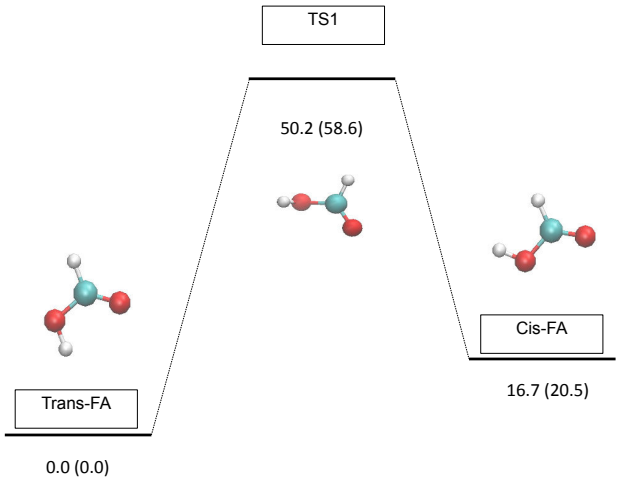

Figure 5.10: Potential Energy Surface (PES) of the formic acid in the gas phase: 2 minima (*Trans* and *Cis*) and 1 transition state between these two minima are represented. The energies are in kJ/mol.

5.5 Dynamics of $Trans/Cis$ isomerisation for the FA molecule embedded in an argon matrix.

We now turn to vibrational excitation and subsequent relaxation dynamics. At the end we have to correctly select the initial conformations for the vibrational excited states of the $Trans$-formic acid (see chapter 3). Once DFT-MD are performed then we follow the $Trans/Cis$ isomerisation via the evolution with time of the OCOH dihedral angle for 16 ps of dynamics. The isomerisation occurs for an angle turning form 0 ($trans$) to 180 (cis) degrees. We have run and analyzed 25 trajectories with different initial vibrational excitation with $n = 1$ in the O-H stretch and C-O-H "skeleton" deformation. All the conformers selected for the trajectories are chosen with an energy above the rotational barrier as represented schematically in figure 5.10.

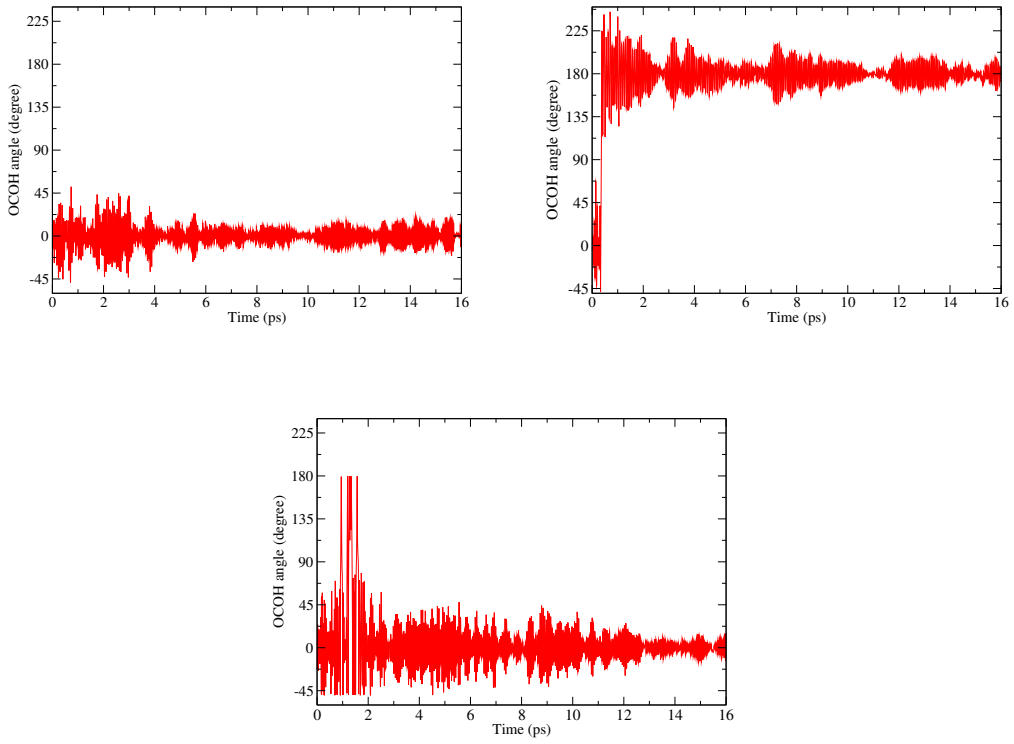

Figure 5.11: Evolution with time of the OCOH angle for three trajectories. Each trajectory of 16 ps dynamics. Top left: no isomerisation for the FA; top right: one single isomerisation; and bottom: several isomerisation.

These trajectories show three different processes, as illustrated in figure 5.11. The isomerisation never occurs for 18 trajectories (denoted hereafter "Case 1"), 2 trajectories show one single $Trans/Cis$ isomerisation (denoted hereafter "Case 2") leading to the *cis* conformer, without any return to the $Trans$ structure and 5 trajectories reveal several Trans/Cis isomerisations (denoted hereafter "Case 3") with a systematic final conformation on the *trans* geometry during our simulation time-scales of 16 ps. We present more detailed analyses in what follows. In the first case (case 1, top left in figure 5.11), the OCOH angle fluctuates between -45° and 45° over time, and is ≈0° on average, which is the signature of the *trans* Formic Acid geometry, with a certain internal energy (≠0 K). The isomerization process does not occur over these types of trajectories.
For the second case (case 2, top right in figure 5.11), the OCOH angle is evolving over 500 fs time scale of dynamics from 0 to ≈180° and stays into the Cis conformation without any return towards a $Trans$ structure for the rest of the 16 ps trajectory.
In the third case (case 3, bottom in figure 5.11), the isomerisation occurs several times between $Trans$ and Cis conformers, and finally trajectories end up into the $Trans$ conformation at the end of the 16 ps. We will see later in the analyses that the conformation has no more enough energy to overcome the $trans - cis$ isomerisation barrier, thus the *trans* conformer being observed.
We find that 7 trajectories over 25, so ≈28% show an isomerisation. The uncertainty is: $\sigma = \sqrt{\frac{P(1-P)}{N_{traj}}}$, if the probability $P = 28\%$, $\sigma = \sqrt{\frac{0.28(1-0.28)}{25}} = 9\%$.
The 28±9% is reasonable comparing with the experimental value of 21% considering the low statistics of the dynamics performed.
In figure 5.11, we can notice that for the first case there is no isomerisation over 16 ps of dynamics. This means that the initial excess energy given by vibrational excitation (n=1) has decreased after few picoseconds and has been redistributed to the matrix such that, there is no sufficient energy in the isomerisation reaction coordinate to overcome the rotational barrier (figure 5.10). We will see with further analyses in this text that this is indeed the case.

We have presented here the results obtained for the conformational dynamics of the FA molecule with three different cases revealed. Our question now is to the understand how the energy (initially contained into the FA molecule) is redistributed into the whole system. To study the energy redistribution to the surrounding argon matrix, it is crucial to know the total energy (potential + kinetic) contained into the formic acid molecule along the dynamics. In

DFT-MD simulations, contrary to classical molecular dynamics, we can not directly know the potential energy of each molecule of the system (only the Kohn-Sham energy of the whole system is known i.e. the solute + the argon matrix). To know the potential energy of the solute molecule we have to calculate the total energy of the FA molecule isolated (i.e with no argon around) during the dynamics (i.e. taking the geometry of FA from the trajectory but removing the argon atoms. The evolution with time of the total energy of the FA solute shows (it will be described later) that over our simulation time-scale the FA internal energy decreases and tend towards an equilibrium value, which is lower than the rotational energy barrier for all cases investigated (case 1, 2 and 3). In 10 ps, whatever the initial excitation energy put in FA, the formic acid molecule has an energy below the energy of the $trans - cis$ isomerisation barrier and thus remains in a given conformation, cis (case 2) or $trans$ (case 1, 3), see in figure 5.11. In case 1 the energy at $t = 0$ is above the rotational barrier, but there is no isomerisation. We will analyze in more details this particular issue.

We want to analyze the vibrational energy transfer between the formic acid molecule and the argon matrix over time. This is what we characterize next as well as its effects on the matrix.

5.6 Effects on the argon matrix

We know study the intermolecular vibrational energy transfers between FA and the argon matrix. To that end, we have followed in time the deformation of the argon matrix with the evolution of the Ar-Ar radial distribution function and the Lindemann coefficient. The Ar-Ar radial distribution functions are calculated every 2 ps of the dynamics for the three different cases (cases 1, 2 and 3) of initial vibrational excitation of the host FA molecule. The results are presented in figure 5.12. During an initial 4 ps,we find that matrix is still organized as a solid, with four different peaks located at 3.8 Å, 5.3 Å, 6.4 Å and 7.4 Å, and a fcc geometry. After 6 ps, the peaks are not as well defined as at the beginning of the simulation, the peaks are broadened and the width of the radial distribution function is not equal to 0. This means that crystalline structure of the matrix is lost. We find that the argon matrix is melting after 6 ps for trajectories with a single or several $trans - cis$ isomerization of FA over time (case 2 and case 3). This nicely shows that some energy is redistributed from FA to the argon matrix (intermolecular vibrational relaxation). In case 1 (i.e. without isomerisation) the redistribution

is not very efficient (less energy is redistributed) in our simulation time-scale since the matrix is maintainted in the fcc geometry after 14 ps of dynamics. In this case, there is not enough energy in the FA molecule to deform the surrounding argon matrix.

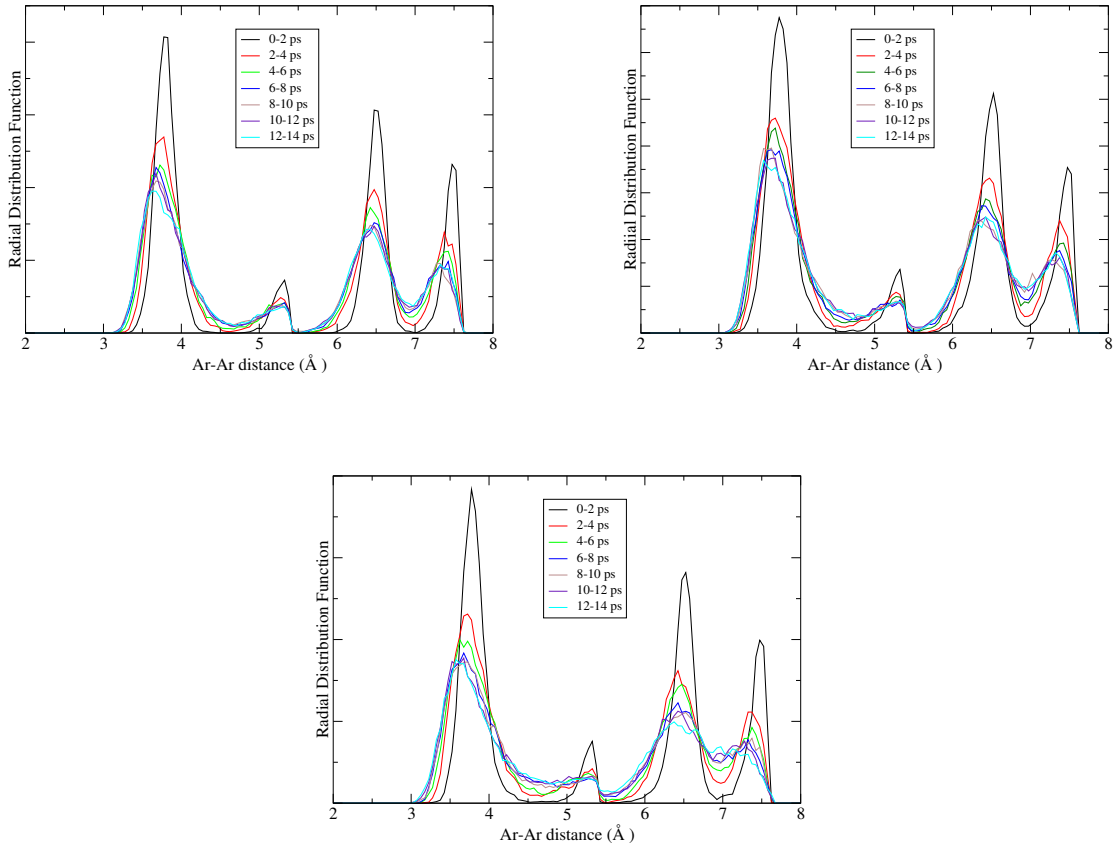

Figure 5.12: Evolution with time of the Ar-Ar radial distribution function calculated each 2 ps of the dynamics for case 1 (top left), case 2 (top right) and case 3 (bottom).

The evolution of the Lindemann coefficient for argon matrix shows similar results in figure 5.13 with same time-scales as the ones previously discusses. We now distinguish two different cases: case 1 is represented with the red line which is an average over the different trajectories without isomerisation of FA and case 2 is represented with the blue line which is an average over the different trajectories with isomerisation(s) of FA (one single or several, see previously case 2 and case 3). The Lindemann coefficient is initially found with a value

of $\Delta_L = 0.1$ which corresponds to a solid state of the argon matrix (as previously shown in section 5.2). During the dynamics the Lindemann coefficient slowly increases to a "plateau" with the value of $\Delta_L = 0.15$ which corresponds to the beginning of the solid-liquid transition. The Lindemann coefficient then continues to increase to values of $\Delta_L > 0.15$, and reaches values of $\Delta_L = 0.20$ and 0.25 after 10 and 16 ps of dynamics. Both the Ar-Ar radial distribution function and the Lindemann coefficient show that after the initial vibrational excitation of the two combined modes of FA, part of the energy of the formic acid is given to the argon atoms, thus provoking the melting of the matrix.

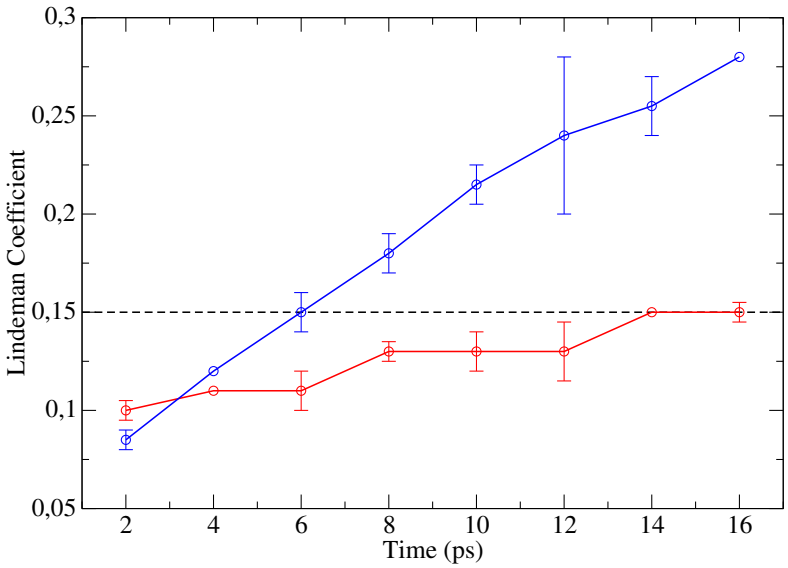

Figure 5.13: Evolution with time of the cumulative Lindemann coefficient for case 1 (i.e. without isomerisation) in red line and case 2 and 3 (i.e. with one/several isomerisation) in blue line. The solid-liquid transition is represented by black dotted line.

5.7 Quantifying vibrational energy relaxation

We will now follow vibrational quantum numbers of different modes of the FA host molecule using the methods reported in chapter 4, in order to quantify the vibrational energy relaxation. We have used two approaches to follow the evolution of the quantum number n_i of one given mode over time as described in chapter 4. These methods are: the "amplitude" method and the "mVDOS" method. The vibrational energy relaxation from the formic acid can be followed in time by these two methods, following the evolution with time of the quantum number n_i in the modes initially vibrationally excited (O-H stretching and C-O-H wagging). Applying the "amplitude" method, figure 5.14 shows the evolution with time of the O-H distance of the Formic Acid (case 1) at four different important points of the dynamics.

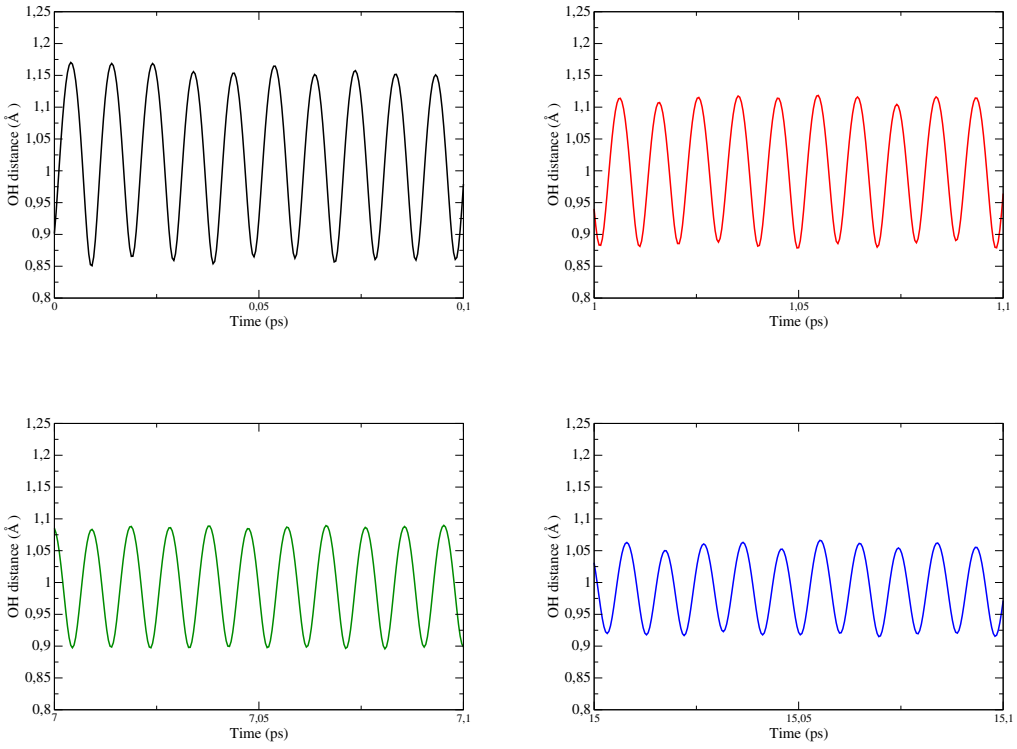

Figure 5.14: Evolution with time of the O-H distance of the Formic Acid (in the case 1) at t=0 ps (in black), t=1 ps (in red), t=7 ps (in green) and t=15 ps (in blue) of the dynamics.

Each value of the amplitude is obtained as the average over 10 oscillations (100 fs), as it has been described in chapter 4. We discuss below the variation in amplitude from the value at the equilibrium geometry (d_{OH}=0.99 Å). One can see that the variation in amplitude of the O-H distance decreases as time proceeds from 0.15 Å (at t=0 ps), 0.11 Å (at t=1 ps), 0.9 Å (at t=7 ps) and 0.6 Å (at t=15 ps). I remind here that one can easily recover the quantum number n_i of the O-H stretching motion from the amplitude of the O-H distance with the formulas of chapter 4 : $A'_i = \frac{A_i}{\mu_i} = \frac{(2E_i)^{(1/2)}}{\omega_i \sqrt{\mu_i}}$ and $E_i = (n_i + \frac{1}{2})\hbar\omega_i$. We thus recover the quantum number n_i of the O-H stretching mode : n_i=1 at t=0 ps, n_i=0.8 at t=1 ps, n_i=0.3 at t=7 ps and n_i=-0.2 at t=15 ps. We will discuss later this negative value.

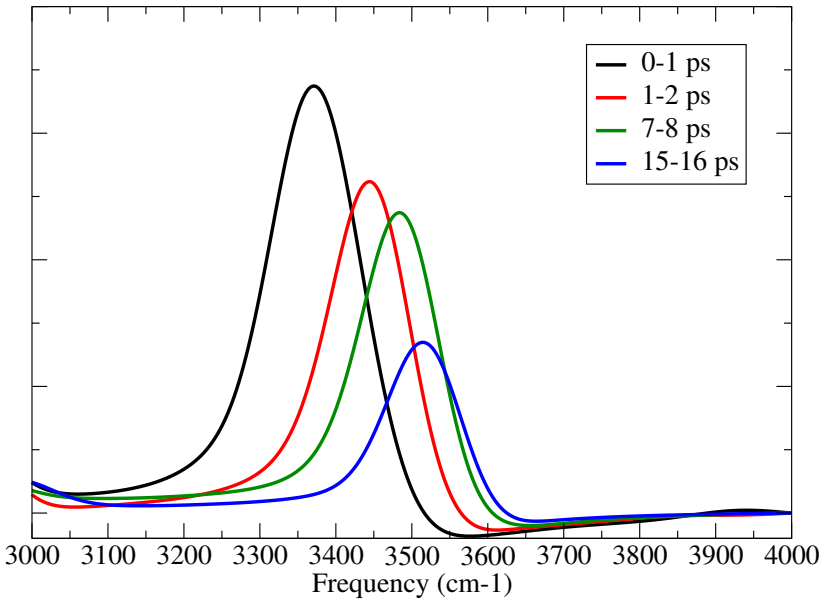

Figure 5.15: Evolution with time of the mVDOS spectra (in the region of the O-H stretching) at different time-scale of the dynamics: 0-1 ps (in black), 1-2 ps (in red), 7-8 ps (in green) and 15-16 ps (in blue).

As explained in chapter 4, even if the time window of calculation between the "amplitude" and "mVDOS" methods are different, we want to compare these values to the "mVDOS" method. The results obtained with the mVDOS method are shown in figure 5.15. We should

note that before looking at the n_i quantum number extracted from this method, the position of the ν(OH) band is blue-shifted during the dynamics from 3370 cm^{-1} over the first picosecond of dynamics (in black), to 3445 cm^{-1} over the second picosecond (in red), to 3485 cm^{-1} over 7-8 ps (in green) and to 3516 cm^{-1} at the end of the 16 ps dynamics (in blue). At the same time, one can see a decreasing of the integral of the band as time proceeds. As we have already seen in chapter 4, the integral can be directly related to the energy of the corresponding vibrational mode and to its vibrational quantum number. The quantum number n_i of the O-H stretching mode thus decreases along the dynamics. Figure 5.16 shows the evolution in time of the quantum number n_i of the O-H stretching motion calculated with the mVDOS method, as an average over the different cases investigated here i.e. without, with one or with several isomerisations of FA during time (cases 1, 2 and 3).

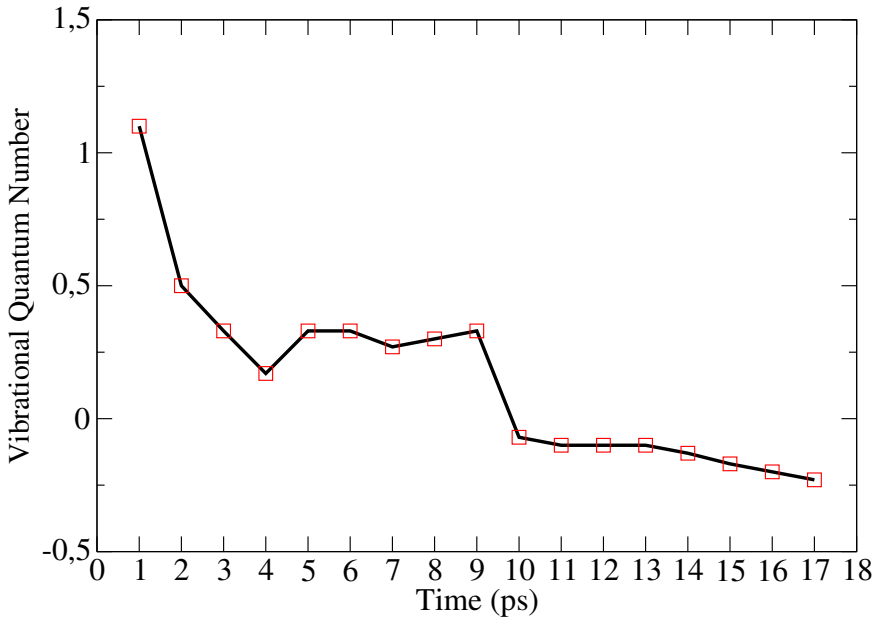

Figure 5.16: Evolution with time of the quantum number n_i of the O-H stretching for an average of 6 trajectories (2 trajectories of case 1, 2 trajectories of case 2 and 2 trajectories of case 3).

Before commenting the plot, one can see that the numbers given by the "mVDOS" method

are very similar to the one given by "amplitude" motion, written just above. Figure 5.16 clearly shows three different time-scales for the evolution of the quantum number for the O-H stretching motion: the value of the quantum number decreases very fast in less than 2 ps, from $n = 1$ to $n = 0.5$, it then takes 8 ps to decrease further from $n = 0.5$ to $n = 0$. It is important to remind here that the isomerization occurs (when it occurs) in less than 2 picoseconds (cases 2 and 3). We can notice that after 9 ps, the quantum number n_i becomes negative. The energy in the corresponding mode is thus below the zero-point energy. As already mentioned, this effect is possible in our dynamics since the nuclei are treated classically [7, 10, 9]. We would expect that one logical explanation for these three time-scales for energy relaxation can be due to the intramolecular (fast energy relaxation) and intermolecular (longer time-scale energy relaxation) vibrational relaxations.

As a check on intra/inter molecular relaxation, we plot in figure 5.17, the evolution of the amplitude of the C-H stretching motion of the FA molecule. In figure 5.17, the variation of amplitude of the C-H distance is initially (over 100 fs) equal to 0.07 which corresponds to $n = 0$. After one picosecond of dynamics, the variation in the amplitude of the C-H motion increases to 0.12 which corresponds to $n = 1$ in that mode, and then decreases again to $n = 0$ after 6 ps of dynamics. After 10 ps the quantum number n_i becomes negative and is equal to $n = -0.3$.

Figure 5.18 shows the same analysis but using the mVDOS method as presented for both C-H and O-H stretching in figure 5.18. The stationary frequencies are respectively located at 2850 cm^{-1} and 3450 cm^{-1}.
The bands in the region 2800-3000 cm^{-1} correspond to the evolution of the C-H stretching motion: over the first picosecond (in black) the frequency of the C-H stretching is 2845 cm^{-1} and the integral of the band gives a quantum number n_i equal to 0.5. Over the second picosecond (in red), the band is slightly red-shifted to 2835 cm^{-1} and the intensity of the band increases whereas the width of the band remains the same. The associated quantum number increases to $n_i = 1$. After 8 picoseconds (in green), the frequency of the C-H motion is 2850 cm^{-1} which corresponds to the stationary frequency of the C-H stretching. The intensity of the band decreases and the quantum number is now equal to 0. At the same time, the intensity of the O-H stretching motion decreases as time proceeds with a blue-shift of the band from 3350 cm^{-1} (after 1 ps), to 3420 cm^{-1} (after 2 ps), to 3450 cm^{-1} (after 8 ps). The stationary frequency of the O-H stretching is reached after 8 ps. The corresponding quantum number

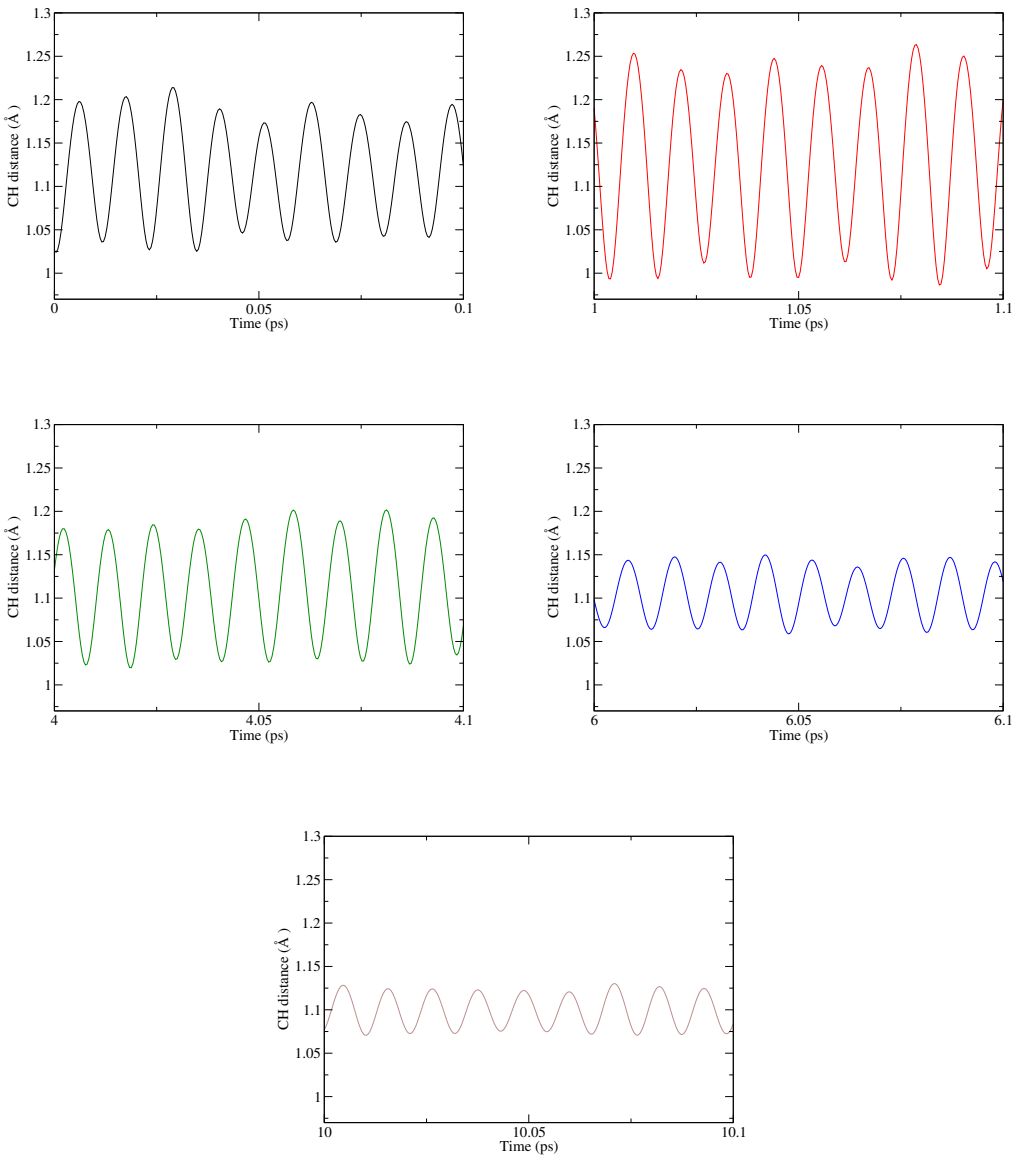

Figure 5.17: Evolution with time of the amplitude of the C-H stretching motion at t=0 (in black), t=1 ps (in red), t=4 ps (in green) , t=6 ps (in blue) and t=10 ps (in brown) , calculated on 100 fs.

decreases from $n = 1$ to $n = 0$ over the same time-scale. From these results, one can say that intramolecular relaxation occurs during the two first picoseconds of dynamics: the energy contained in the O-H stretching is in particular redistributed to the C-H stretching motion.

We have followed here the C-H stretching motion as an exemple for intramolecular transfers. We can easily follow the quantum number n_i of the high frequency modes (such as stretching modes or some bending). Low frequency modes are very difficult to follow in time for both "mVDOS" and "amplitude" method because of modes coupling: the O-H wagging is strongly coupled with the C-O-H bending due to the geometry of the molecule and the small number of degrees of freedom of the Formic Acid. We will try to overcome this problem by increasing the size of the molecule (i.e. the number of degree of freedom) as can been seen in chapter 6.

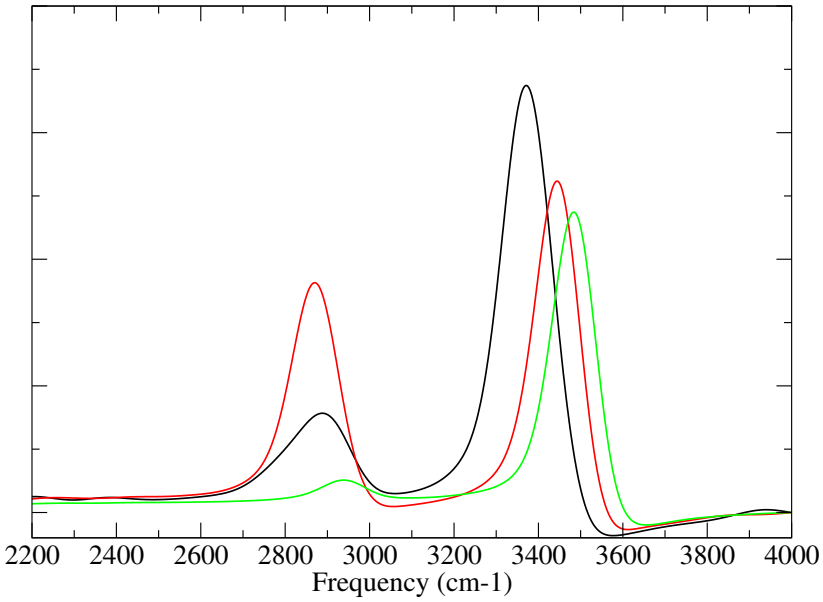

Figure 5.18: mVDOS spectra of the Formic Acid after 1 ps (in black), 2 ps (in red) and 8 ps (in green). Each spectra has been calculated on 1 ps.

5.8 Relaxation to thermal equilibrium

At the beginning of our dynamics the system is out of equilibrium since the host Formic Acid molecule is initially vibrationally excited. From this, it is crucial to know the timescale to reach a thermal equilibrium. We investigate this issue from the point of view of kinetic energy (or temperature). Kinetic energy and temperature are related through equation 5.3, where 3N-6 is the total number of degrees of freedom of the system composed of N atoms (removing translation and rotation of the whole system).

$$E_{kin} = \frac{(3N-6)k_B T}{2} \tag{5.3}$$

We have previously shown (in section 5.7) that after 8-10 ps of the dynamics, most of the energy initially contained in formic acid is redistributed to the argon through intermolecular vibrational relaxation. This energy transfer leads to the melting of the argon matrix. Here, using the evolution with time of the kinetic energy of the argon matrix (in black in Fig 5.19) compared with the kinetic energy of the FA solute molecule (in red in Fig 5.19), we want to investigate if the system thermalizes over the DFT-MD simulation time-scale. At this end we have prolongated our trajectories up to 35 or 40 ps. Figure 5.19 represents the evolution with time of the temperature of the FA molecule and the argons for three different trajectories chosen in cases 1, 2 and 3.

These three plots nicely show that after 24 ps of dynamics (following the FA vibrational excitation), the temperature of the formic acid and the argon are close, within temperature fluctuations of each part of the system. Indeed, the average temperature on the equilibrium part of the formic acid is 270 K± 150 K and the average temperature on the equilibrium part of the argon matrix is 250 K± 30 K. We thus can say that the system is indeed very close to thermal equilibrium within this 40 ps time-scale. This is a pretty short amount of time, which is very nice for DFT-MD simulations, where simulation time is always a crucial issue.

In this chapter, we have shown that the vibrational excitation of the host Formic Acid molecule in an argon matrix can involves the *trans-cis* isomerisation of the FA (with a quantum yield very close to the experimental data of Pr. Markku Rasanen) but also the deformation of the argon matrix. We have followed in time the quantum number n_i in the O-H and C-H stretching modes of the Formic Acid molecule with the "mVDOS" and "amplitude" methods.

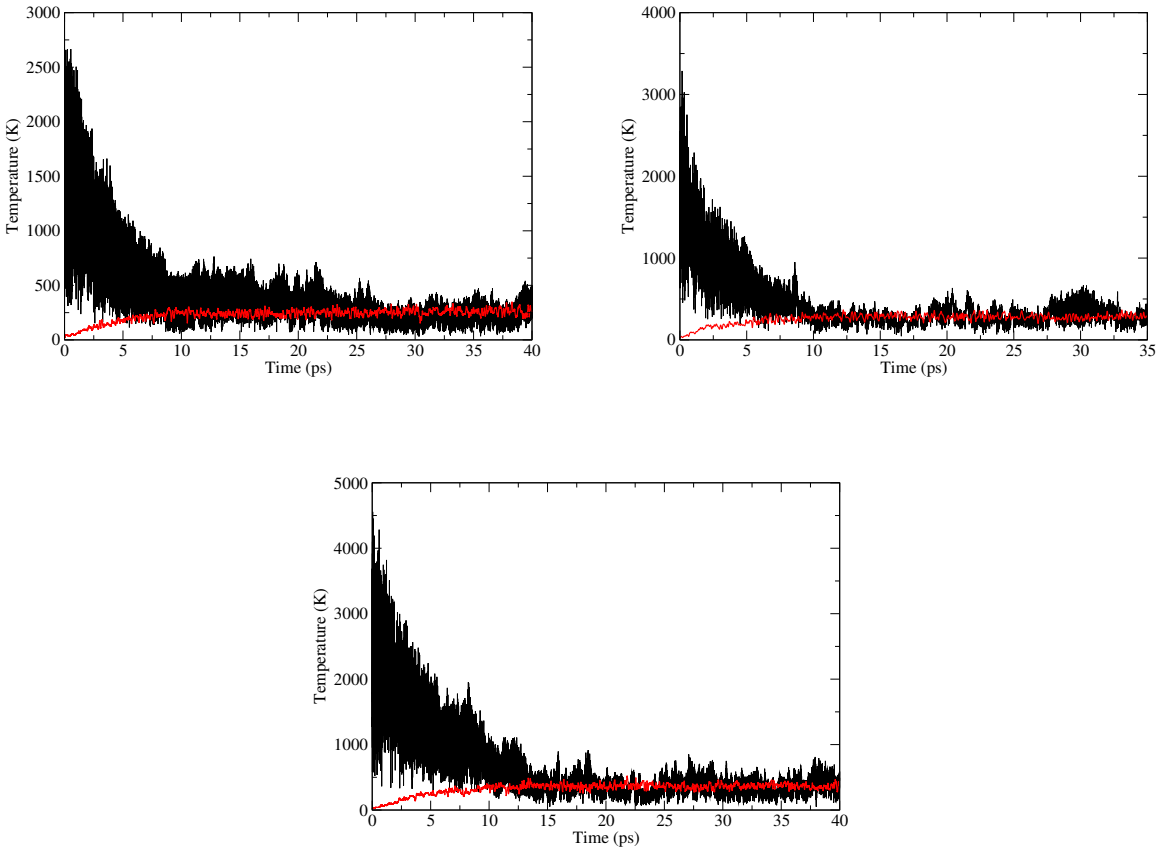

Figure 5.19: Evolution with time of the Temperature of the Formic Acid (in red) and the argon (in black) for three different trajectories of the FA molecule initially vibrationally excited with $n = 1$. On the top left , the conformer stays in the Trans conformation, on the top right the conformer isomerizes to a Cis structure and on the bottom, several Trans/Cis isomerisations occurs during the simulation time-scale.

In next chapter, we will be interested in the second prototypical example: the gas phase illustrated with the $(Cl^{-}...NMA)Ar$ clusters.

Chapter 6

Vibrational dynamics of $(Cl^- \cdots NMA)Ar$ clusters

6.1 Modelling IR-PD processes and experiments

Linear absorption Infrared spectroscopy (IR) has been successfully applied for decades on all kinds of molecular systems in the liquid phase, solid phase and in matrices. The past two decades has seen the development of new vibrational spectroscopy methods, and in particular gas phase spectroscopy has been "revolutionized" during the past two decades with the development of action spectroscopy. Up to the development of action spectroscopy, one of the only ways to probe the vibrational spectroscopy of gas phase molecules was by means of low-temperature matrix experiments, where the gas phase molecule of interest was embedded into an inert matrix (most of the time composed of rare gas atoms like Ar, Xe, or nitrogen N_2), and then was probed by IR absorption. Not all molecules are easy to include in such a matrix, it also becomes more and more difficult to insert clusters into matrices, and furthermore the final experiments have to be conducted at low temperatures (for the matrix to be kept, typically about 10 K) which can impede a full comprehension of the vibrational signatures at more relevant temperatures.

Action spectroscopy means that the absorption of one or several photons by the molecular system investigated will lead to an action, typically the fragmentation of the system, of one sort or another (see below for IR-PD of interest to us). This action of fragmentation will be

recorded for a given wave-length of the absorbed photon(s), and will be repeated for wave-lengths in a given domain.

Why do we need this action/fragmentation to occur in order to record a vibrational spectrum ? The main reason is that the production of molecules in the gas phase and their interrogation by lasers in the gas phase is a difficult task, due to the low quantity of molecules present in space in the gas phase (by construction). The efficiency of absorption is thus very low and the resulting linear IR absorption spectrum would be extremely noisy (at the best), or completely inexistant (at the worst). On the contrary, recording the consequence (action) of the absorption by means of fragmentation is providing an efficient way to produce vibrational spectra in the gas phase. The final vibrational action spectrum records the efficiency of the absorption at a given wave-length for the action/fragmentation of the gas phase molecule of interest. The vertical axis in the action spectra is thus the fragment ion yield recorded as a function of the IR vibrational excitation energy. It is not a linear IR absorption, so that intensities between linear IR absorption and action spectroscopy are usually not comparable; band-positions and band-shapes are comparable though.

Action spectroscopy in the gas phase relies on:

1) Molecules, clusters and any molecular assemblies have to be produced in the gas phase. This is done by Mass Spectrometry experiments, typically using ESI (ElectroSpray Ionisation) or MALDI (Matrix-Assisted Laser Desorption/Ionisation) techniques, that will not be described here. These techniques are used in IR-MPD (InfraRed Multi-Photon Dissociation) action spectroscopy developped by Maitre *et al.* [111] on the CLIO set-up at the University Paris Sud Orsay in France, and developed by Oomens and von Helden [112] on the FELIX set-up in The Netherlands (set-up now located at the University of Radbout in The Netherlands). In IR-PD (InfraRed Photon Dissociation or InfraRed Pre-Dissociation) experiments, this initial stage of production is usually different.

In the IR-PD experiments from the group of Prof J. Lisy (University of Urbana-Champaign, USA) that are of interest to us in the present dissertation, clusters are investigated and they are produced through collisional processes that are schematically illustrated in figure 6.1. In these experiments, clusters composed of metal ions (typically Na^+, Li^+, Cl^-) and solvent molecules (typically water, methanol, and possibly a mixture of both) are produced in the gas phase. Briefly, a mixture of argon clusters (size unknown, but very large clusters are produced) with the solvent molecules is produced in a supersonic expansion, i.e. at very low temperatures

of the order 10-20 K. The resulting mixed neutral cluster Ar-solvent (mostly comprised of Ar) is entrained towards a collision chamber where impacts with the metal ions occur, thus creating cluster ions. Excess energy in these nascent cluster ions (arising from the ion impact and solvation processes) is dissipated by argon evaporation until the cluster ions reach a quasi-stable state (i.e. have a lifetime sufficient to traverse the experimental apparatus). Electrostatic lenses and an octupole ion guide are used to guide these cluster ions into a detection chamber housing three quadrupoles. The first quadrupole mass filter is used to mass-select a parent cluster ion of interest from among the stable ions produced in the source chamber. In the second quadrupole, the parent ions interact with a single 10 ns pulse, from a gently focused tunable mid-IR laser. Resonant photon absorption provides sufficient energy for the parent cluster to dissociate, creating a fragment ion. The third quadrupole mass filter is tuned to select the fragment ion to be interrogated by IR absorption. What is commonly done in the experiments of Prof Lisy's group is to select cluster ions of interest (for instance Cl^-...NMA, where NMA=N-Methyl-Acetamide molecule) in interaction with one argon atom or a few argon atoms. This step of formation of the ionic clusters by collisions has been modeled in the group recently [113] by AIMD.

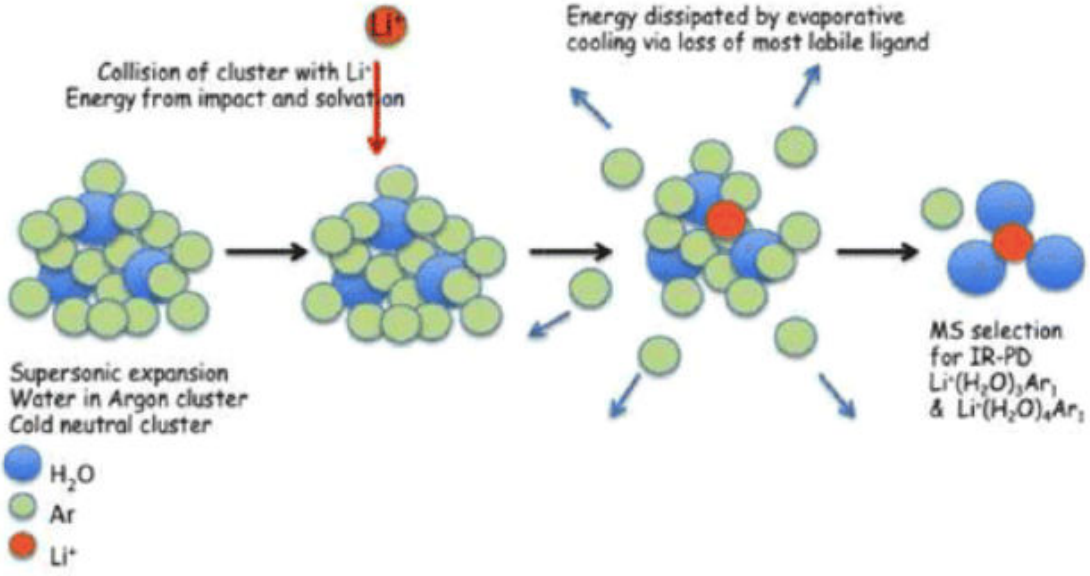

Figure 6.1: Principle of the IR-PD experiments of the group of J. Lisy in the USA.

2) What is then measured is the loss of argon (i.e. argon channel), i.e. meaning what is

recorded is the departure of one argon ore more argon atoms from the ion cluster subsequent to the absorption of one photon in the 3000-4000 cm^{-1} range. The action spectroscopy is here the result of the loss of argon, as illustrated in Figure 6.2. The experiment from the Lisy's group are also called argon-tagging action spectroscopy, as one argon is tagged to the cluster vibrationally probed, and the departure/loss of this argon is recorded as the action.

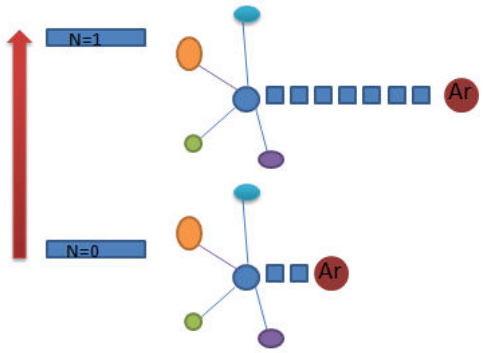

Figure 6.2: Argon tagging principle in the IR-PD experiments of the group of J. Lisy in the USA.

The second step in action spectroscopy, and especially in IR-MPD and IR-PD experiments, is the absorption process of one photon (IR-PD) or several photons (IR-MPD) leading to the recorded action (loss of the tagged argon in IR-PD, fragmentation into chemical pieces in IR-MPD). Internal vibrational energy relaxation (IVR) is the key process following the IR absorption, i.e. energy absorbed by one mode at a given wave-length will be released within the system, through internal and/or external relaxation, and will ultimately possibly lead to the loss of the argon atom in IR-PD.
The unknowns there are the processes of IVR: how the absorbing mode is coupled to other vibrational modes in order to release part of the excess vibrational energy absorbed in the first place, what is the competition between internal energy relaxation (i.e. through intramolecular modes of the absorbing molecule) and intermolecular energy relaxation (i.e. through intermolecular mode couplings), why are certain absorptions more efficient than others (i.e. the balance in the intra/inter-molecular transfers), and can we somehow simulate the final IR-PD/IR-MPD spectrum by means of molecular dynamics simulations, and can we also understand the relation between the intensity in action spectra (i.e. efficiency of fragmentation) and the intensity in the linear absorption spectra.

These are roughly the questions we would like to address with DFT-based molecular dynamics simulations performed in this work. This was somehow ambitious/challenging questions on which we unfortunately have not been successful enough. We initially thought that timescale affordable in AIMD would be the issue, we discovered that other issues were at play against us. As already mentioned at the end of the previous section, here possibly comes again the issue of zero-point energy leakage (ZPE leakage). Indeed, here in the modeling of IR-PD mechanisms and processes, energy flows are by construction at the heart of the processes. Here again, one has to ask what consequences of introducing ZPE in the vibrational modes of the molecular system at the initial start of the dynamics, i.e. introducing the quantum nature of the nuclei while the dynamics treat the nuclei as classical nuclei, has on the final properties investigated.

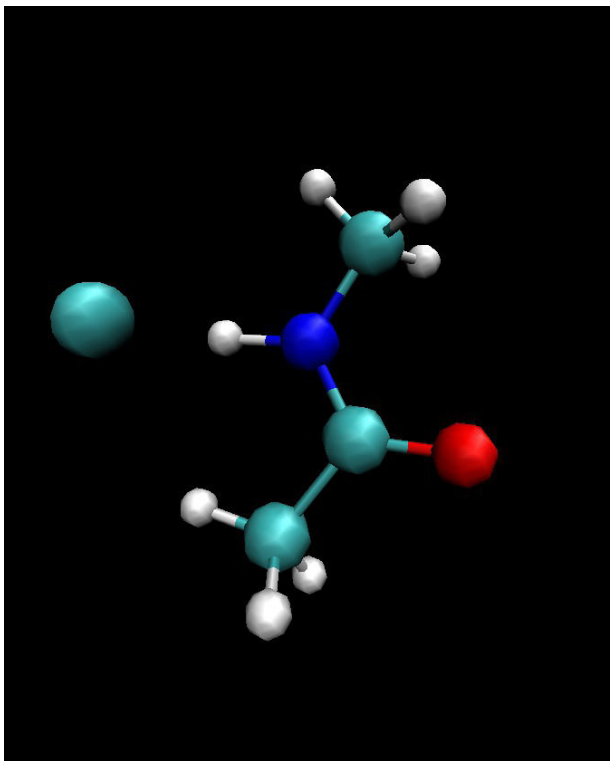

Figure 6.3: Snapshot of a geometry optimised structure of ($Cl^{-}...NMA$). This structure is responsible for the experimental IR-PD signatures as demonstrated in ref. [2] by Gaigeot and Lisy.

In this section, we report our preliminary trajectories for the introduction of the zero-point

vibrational energy (ZPE) ($n = 0$) and vibrational absorption (transition $n = 0 \rightarrow n = 1$) in ($Cl^- \cdots NMA$)Ar clusters (NMA=N-Methyl-Acetamide) of interest in collaboration with the group of Prof Lisy at the University of Urbana-Champaign, USA.

Of course, the ZPE should be introduced in all vibrational modes, as should be required by quantum mechanics. For reasons related to temperature (it will be discussed later) of the molecular systems (and definition of temperatures), we first investigated conditions where only part of the ZPE is included. Also for reasons related to temperature (and too high values of this classical temperature), we furthermore mix classical sampling and Wigner sampling for the initial conditions of the trajectories. Typically, the crucial mode we are interested in is the N-H mode of NMA in the ($Cl^- \cdots NMA$)Ar cluster. This N-H stretch is thus treated "quantum mechanically" through the Wigner distribution sampling, while the other modes are introduced through the classical sampling.

6.2 Geometry Optimisation

Before describing AIMD trajectories, let me describe the optimized geometries of $(Cl^-...NMA)Ar$ clusters. The structure of $(Cl^-...NMA)$ is known from ref [2]. 2 conformations of $(Cl^-...NMA)Ar$ have been optimized at the BLYP-D2/aug-CC-pVTZ level of theory (with Gaussian 09). At the start of the optimisation process the argon atom has been put around the $Cl^-...NMA$ in different spatial positions. We obtain 2 optimized structures illustrated in figure 6.4. In the first structure the argon atom is located in the plane of the $(Cl^-...NMA)$ cluster (this structure will be called "in-plane" afterwards). In fact three other structures have been optimized with the argon atoms "in plane" with same energies (argon can be found at different positions around the $(Cl^-...NMA)$ complex, i.e close to the CH_3, to Cl^-, to $C = O$) but we will illustrate only one case with the argon "in plane". In the second structure the argon atom is located out of the plane of the cluster (this structure will be called "out of plane" afterwards). These two structures are only separated by 0.3 kcal/mol (the "out of plane" is the more stable structure).

The BLYP+D2 approach has been previously used in similar systems by Gaigeot et al. [2]. The two structures illustrated in figure 6.4 will be used as starting conformations for our dynamics simulating IRPD processes.

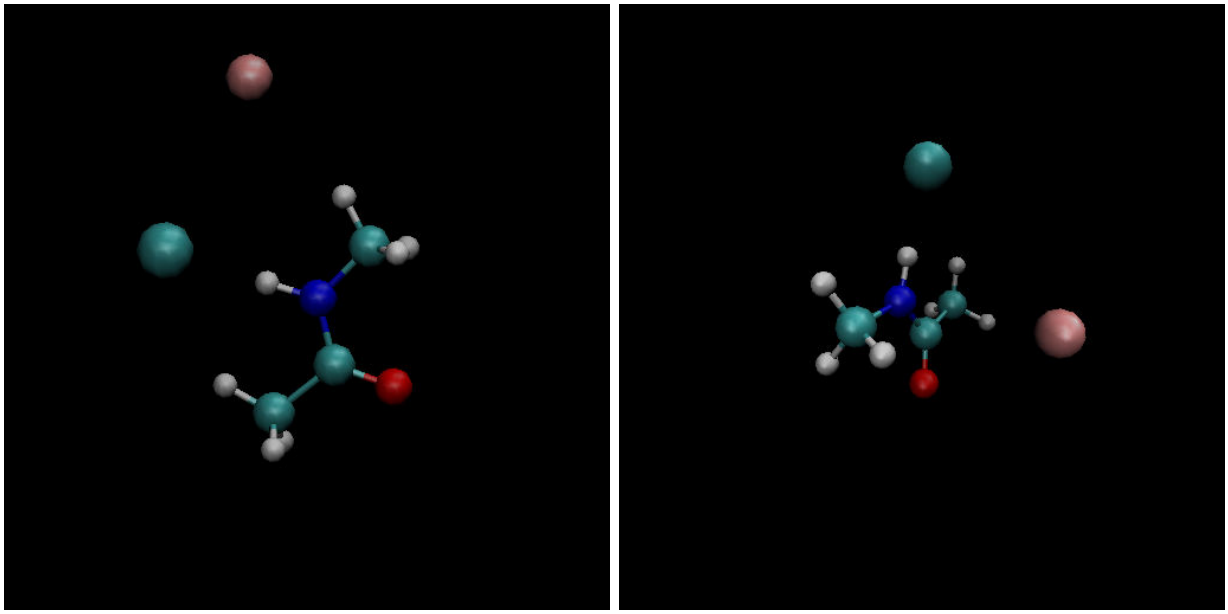

Figure 6.4: 2 conformations of the $(Cl^{-}...NMA)Ar$ cluster after geometry optimisation. Argon is in pink, Cl^{-} is in green. On the left, the argon atom is in the same plane as the $(Cl^{-}...NMA)$ cluster. On the right, the argon atom is located out of the plane.

6.3 Dynamics without vibrational excitation

One worry of the dynamics we have in mind is the stability (or binding) of the argon atom to the $(Cl^{-}...NMA)$ at finite temperature. As reference trajectories for testing the stability of the Argon within the $(Cl^{-}...NMA)Ar$ complex at finite temperature, we have first performed "traditional" Born-Oppenheimer molecular dynamics simulations (i.e. without vibrational excitation) where a Boltzmann distribution for initial velocities has been used, and the initial positions of the atoms come from the optimized structures.
We have decided to present here the results obtained for the "in plane" and "out-of-plane" initial structures (at t=0). I remind here that the size of the box is 20 Å . The argon atom will be considered as evaporated from the $Cl^{-}...NMA$ cluster at a "cut-off" distance of 7 Å from the center of mass of the $Cl^{-}...NMA$ (the center of mass of the $Cl^{-}...NMA$ cluster is located on the nitrogen atom).

We present in figure 6.5, the results obtained from some of our trajectories for the evolution

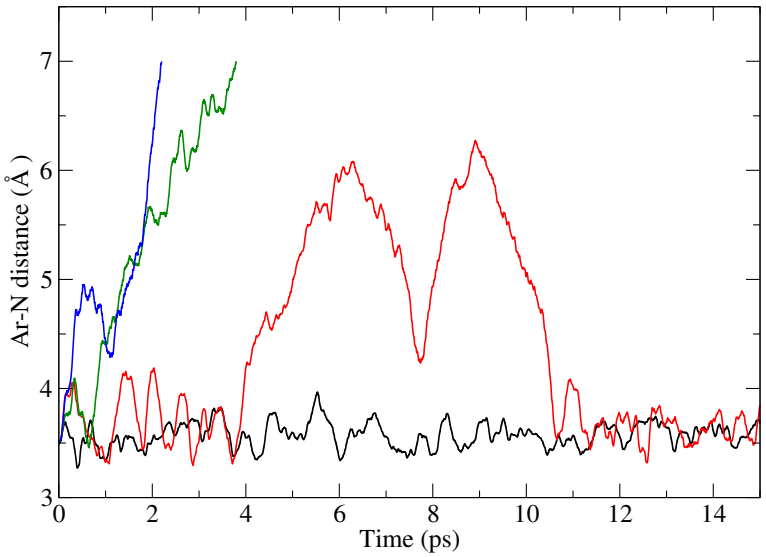

Figure 6.5: Evolution with time of the distance between the argon atom and the nitrogen atom of the $Cl^{-}...NMA$ cluster at four different temperatures: 30 K (in black), 75 K (in red), 90 K (in blue) and 150 K (in green).

with time of the distance between the argon atom and the center of mass of $(Cl^{-}...NMA)$ at 4 different temperatures: 30 K (in black), 75 K (in red), 90 K (in blue) and 150 K (in green) where the Ar is initially located out of the plane of the cluster. The results are the same when the Ar is initially located in the plane of the cluster. We can see that for the lowest temperature (30 K, in black curve) the argon atom stays around the $Cl^{-}...NMA$ cluster (during 14 ps), the distance between the argon and the nitrogen atoms is oscillating between 3.2 and 3.9 Å . The argon atom stays very close from its initial position ($d_{N-Ar}(0) = 3.5$ Å). The evolution of this distance at 75 K (in red curve), shows three different behaviors over the 14 ps of dynamics. During four picoseconds, the argon stays in its initial position ($\approx$ 3.3 and 4.1 Å). Then, during the following 6 ps, the argon atom turns (out of the plane) around the $(Cl^{-}...NMA)$ cluster and is seen coming back to its initial position (after 10 ps). The temperature is not sufficient to evaporate the argon atom from the cluster. The trajectories at 90 K and 150 K, respectively in green and blue curves, clearly show that the argon atom is evaporating from the $(Cl^{-}...NMA)$ very shortly after start of dynamics. Indeed, the Ar-N distance increases quickly toward the "cut-off" distance of 7 Å .

In this section, we have shown that Born-Oppenheimer molecular dynamics without excitation at temperature higher than 80 K lead to the evaporation of the argon atom from the $(Cl^{-}...NMA)$ cluster. This temperature is reminiscent to the one we have found for the melting of the matrix in chapter 5. This is a low temperature in a way, and the obvious worry is that any vibrational excitation put in the $(Cl^{-}...NMA)$, at least at high frequency will lead to the departure of Ar, but this departure is only due to the temperature in the system, not because of specific vibrational redistributions.

6.4 Dynamics with vibrational excitation (n=1)

Now we turn to the study of dynamics after vibrational excitation (n=1) in the N-H stretching mode of $(Cl^{-}...NMA)$. 15 independent trajectories of 14 ps each with this initial vibrational excitation have been performed. 8 trajectories were started using the geometry of $(Cl^{-}...NMA)Ar$ with the argon atom located in the plane of $(Cl^{-}...NMA)$ as in fig 6.4 left, 7 from the geometry where Ar is located out of the plane, as in fig 6.4 right. Initial conditions are prepared using the semi-classical sampling, as described in chapter 3. Positions Q_i are selected within the Wigner quantum distribution. Velocities followed equation 3.31. Figure 6.6 presents results obtained for one chosen trajectory with the argon atom initially located "out of plane". This trajectory is representative of all trajectories. The average temperature in the cluster is found at 350 K. Snapshots are taken each picosecond of the dynamics. We observe that the argon atom evaporates from the cluster.

Here, these trajectories show that we are capable of vibrationally excite one mode and follow in time the evaporation of argon, in a time scale compatible with DFT-MD. But, it is impossible to say if the initial vibrational excitation is the only thing responsible for the loss of the argon atom. Indeed, as we have shown in section 6.3, if the temperature is greater than 80 K, the argon atom is therefore systematically evaporating from the $(Cl^{-}...NMA)$ cluster.

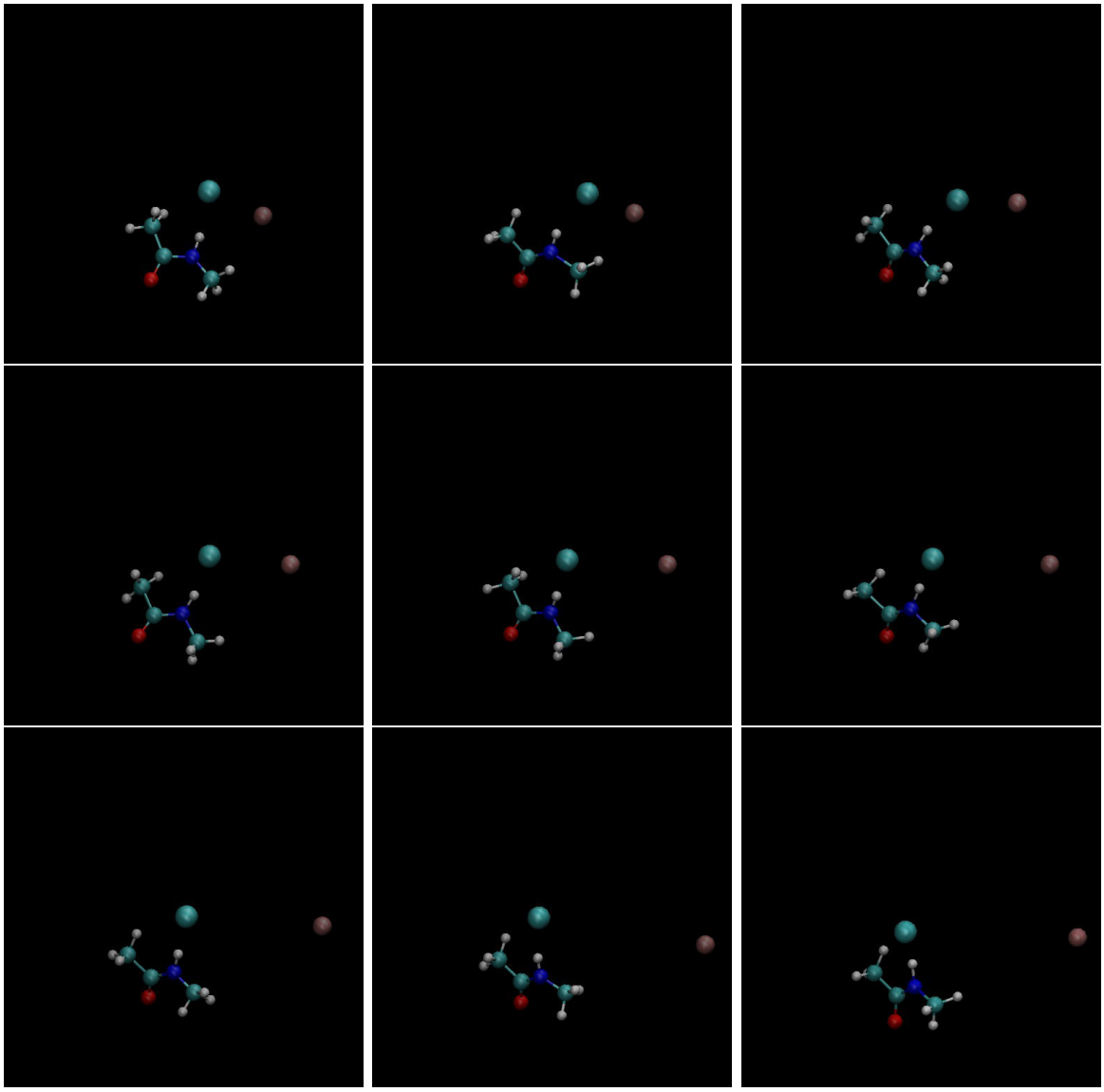

Figure 6.6: Dynamics of loss of the argon atom in $(Cl^{-}...NMA)Ar$ cluster by DFT-MD following an initial vibrational excitation in the N-H stretching mode. Snapshots are taken each picosecond of the dynamics.

6.5 Vibrational quantum number evolution in modes

We now turn to the following of vibrational quantum numbers in the $(Cl^{-}...NMA)$ cluster using the methods reported in chapter 4, in order to quantify the vibrational energy relaxation.

These methods are here again, the "amplitude" and the "mVDOS" methods. The vibrational energy relaxation form the $(Cl^{-}...NMA)$ can be followed in time by these two methods, following the evolution of the quantum number n_i in the modes vibrationally excited. We have excited a high frequency mode, the N-H stretching mode. Applying the "amplitude" method, figure 6.7 shows the evolution with time of the N-H distance in the $(Cl^{-}...NMA)$ cluster, at four different times along the dynamics.

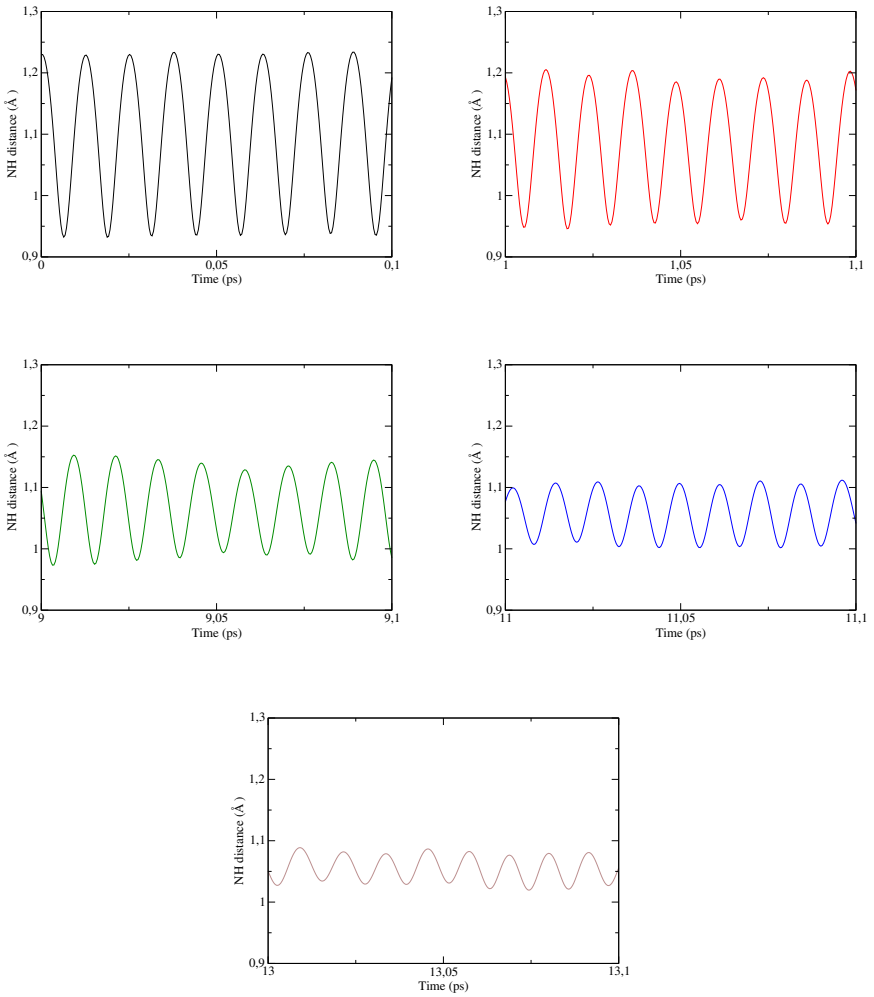

Figure 6.7: Evolution with time of the N-H distance of the $(Cl^{-}...NMA)$ cluster at t=0 ps (in black), t=1 ps (in red), t=9 ps (in green), t=11 ps (in blue) and t=13 ps (in brown) of the dynamics.

We discuss below the variation in amplitude from the value at the equilibrium geometry

(d_{NH}=1.08 Å). One can see that the variation in amplitude of the N-H distance decreases as time proceeds from 0.14 Å (at t=0 ps), 0.12 Å (at t=1 ps), 0.09 Å (at t=9 ps), 0.05 Å (at t=11 ps) and 0.03 Å (at t=13 ps). We recover the quantum number of the N-H stretching mode: n_i=1.2 at t=0 ps, n_i=1 at t=1 ps, n_i=0.5 at t=9 ps, n_i=-0.2 at t=11 ps and n_i=-0.4 at t=13 ps. We find here again negative values for the quantum number n_i of the N-H stretching motion. These values are the consequence of the ZPE leakage since the energy of this high frequency mode is below the zero point energy at the end of the dynamics.
As previously done in chapter 5, we want to compare these values to the "mVDOS" method. The results obtained with the "mVDOS" method are shown in figure 6.8.

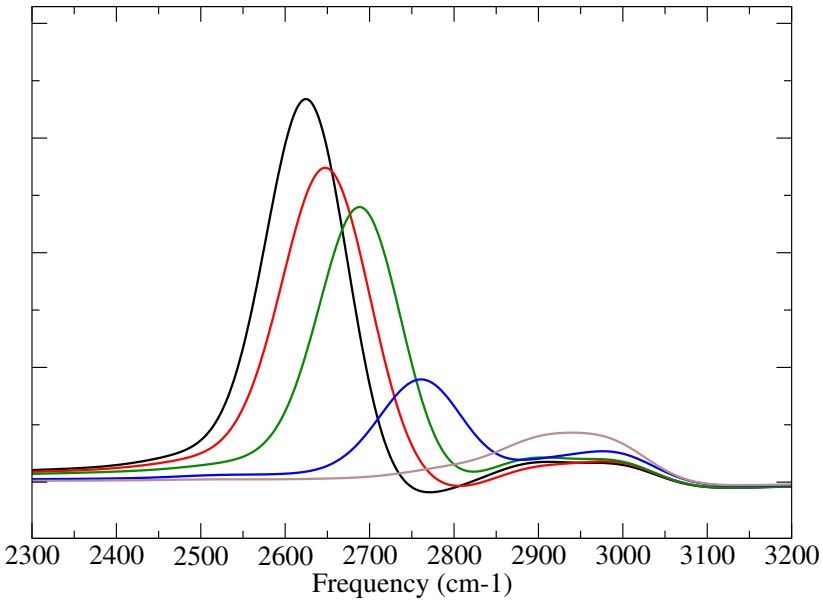

Figure 6.8: Evolution with time of the mVDOS spectra (in the region of the N-H stretching) at different time-scale of the dynamics: 0-1 ps (in black), 1-2 ps (in red), 8-9 ps (in green), 11-12 ps (in blue) and 13-14 ps (in brown).

First of all, we should note that the position of the ν(NH) band is blue-shifted during the dynamics from 2625 cm^{-1} over the first picosecond of dynamics (in black), to 2650 cm^{-1} over the second picosecond (in red), to 2688 cm^{-1} over the 8-9 picosecond (in green), to 2761 cm^{-1}

(in blue) and to 2945 cm^{-1} at the end of the 14 ps dynamics (in brown). At the same time, we can see a decreasing of the integral of the band as time proceeds. The quantum number n_i of the N-H stretching mode thus decreases along the dynamics. Table 6.1 shows the evolution in time of the quantum number n_i of the N-H stretching motion calculated with the mVDOS method.

Time window (ps)	0-1	1-2	2-3	3-4	4-5	5-6	6-7
$\nu(NH)$	1.2	1	1.1	1	1.2	0.9	1.1
Time window (ps)	7-8	8-9	9-10	10-11	11-12	12-13	13-14
$\nu(NH)$	1	0.6	0.5	0.2	0	-0.2	-0.4

Table 6.1: Evolution in time of the quantum number n_i of the N-H stretching motion calculated with the mVDOS method.

Table 6.1 clearly shows two different time-scales for the evolution of the quantum number for the N-H stretching motion: the value of the quantum number stays very close from the initial value $\approx n_i = 1.2$ during 7 picoseconds of dynamics, then decreases quickly further from $n = 0.5$ to negative values in the second part of the dynamics. We should expect that the energy initially contained in the N-H stretching is redistributed via intramolecular vibrational relaxation to other modes of the molecules.
As a check on intramolecular relaxation we plot in figure 6.9, the evolution of the mVDOS spectra of one low frequency mode: the N-H wagging.

At the beginning of the simulation, there is no peak located in the region of the N-H wagging motion (750-900 cm^{-1}), this corresponds to our initial preparation in which there is no energy in this particular vibrational mode. The first band appears after 8 ps of dynamics (in green). Then we can clearly distinguish peaks in blue and in brown, taken respectively at times 11 and 13 ps of the dynamics. The corresponding quantum numbers are n_i=0.3 at t=8 ps, n_i=0.9 at t=11 ps, and n_i=0.9 at t=13 ps. We observe a clear energy redistribution from the high frequency mode (N-H stretching) toward this low frequency mode. Contrary to the Formic Acid molecule embedded in the matrix, we can follow in time the evolution of low frequency modes with the mVDOS method. This is due to the increase number of degrees of freedom in the $(Cl^-...NMA)$ cluster.

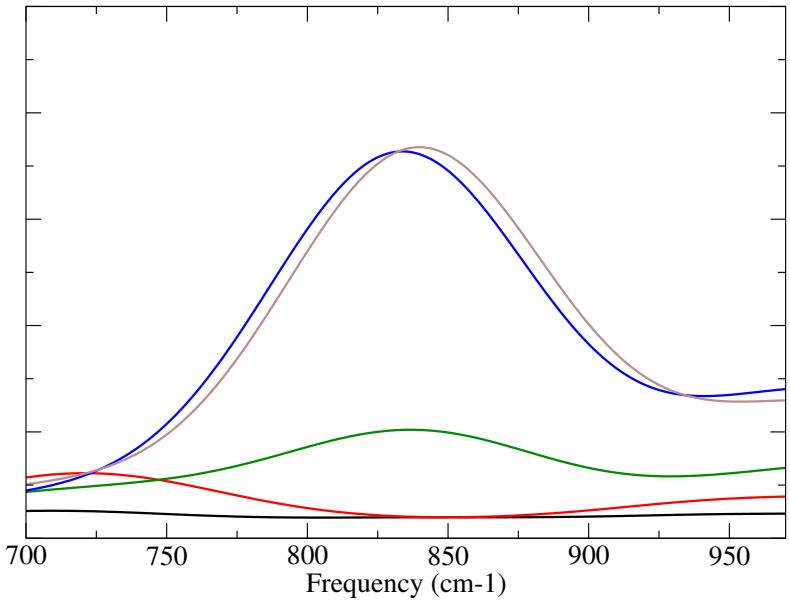

Figure 6.9: Evolution with time of the mVDOS spectra (in the region of the N-H wagging: 750-900 cm^{-1}) at different time-scale of the dynamics: 0-1 ps (in black), 1-2 ps (in red), 8-9 ps (in green), 11-12 ps (in blue) and 13-14 ps (in brown).

In this chapter, we have shown that we can vibrationally excite one normal mode and follow the departure of the argon atom from the $(Cl^{-}...NMA)$ cluster. But our dynamics of excitation have a temperature higher than the temperature of evaporation of the Ar. That's why it is difficult to say if the loss of the argon is due to our initial vibrational preparation. Nevertheless, this system allows us to follow the quantum number evolution in time (as for Formic Acid in the previous chapter) and show specifically that there is energy transfers from high to low frequency modes. Low frequency modes are much well defined than for the previous small molecule Formic Acid.

Chapter 7

General conclusions

In the present thesis we showed that for two prototypical examples in condensed and gas phase, we can follow and quantify the vibrational energy in normal modes after vibrational excitation. This work has been done in the condensed phase with the host Formic Acid immersed in an argon matrix and in the gas phase with $(Cl^{-}...NMA)Ar$ clusters. After the preparation of initial conditions using the semi-classical Wigner sampling, several DFT-MD trajectories have been performed to analyse the Intra/Inter vibrational energy relaxation. Two theoretical alternative models have been used to follow the evolution with time of the quantum number n_i of each mode: a new method based on the study of vibrational density of states (VDOS) compared with a more traditional method based on the study of the amplitude of a specific motion (i.e. distance or angle) of the molecule. Both methods reveal similar results.
In the condensed phase, the quantum yield of the $trans - cis$ isomerisation process of the Formic Acid molecule has been compared to the experimental data. We have shown that the vibrational excitation of two combination modes involves in some cases the isomerisation of the Formic Acid molecule. This initial vibrational excitation of the Formic Acid has also an impact on the surrounding matrix: the energy initially contained into the FA is redistributed to the matrix that leads to the deformation and the melting (i.e. solid-liquid transition) of the argon matrix within our DFT-MD simulation time-scale.
In the gas phase, we have shown that vibrational excitation of the N-H stretching motion of the $(Cl^{-}...NMA)$ involves the systematic loss of the argon atom. Nevertheless, we can not clearly define if this evaporation of the argon is due to the vibrational excitation and energy redistribution or the effects of temperature. Finally, the two models have shown that in both

condensed or gas phase environment, after the vibrational excitation $n = 1$ of a normal mode at t=0 of the dynamics, this normal mode comes back in its ground state $n = 0$ and then it often takes negative values of n_i. The negative values can be explained with the Zero Point Energy (ZPE) leakage: vibrational energy flows freely between all or a subset of the modes and, hence, does not preserve any ZPE constraint (i.e. some high-frequency modes thus loose energy below their ZPE while low-frequency modes gain energy).

In future works for condensed phase, it can be interesting to study the isomerisation process for other carboxylic acids after the vibrational excitation in high-overtone $n_i = 2, 3, 4...$ in larger matrices (i.e. increasing the number of argon atoms of the matrix). Indeed, Jan Lundell et al. [114], have shown high-overtone inducing chemistry of oxalic acid (OA) isolated in a low-temperature argon matrix using Raman spectroscopy.
Dr. Daria Galimberti is now working in the group on the study of the dynamics of $Li^+Ar_6CH_4$ clusters in the gas phase after initial vibrational excitation ($n = 1$) in C-H stretching motion and the following of vibrational quantum number and energy redistribution in intra/inter molecular modes, using the developed methods.

Bibliography

[1] M.-P. Gaigeot, M. Martinez, and R. Vuilleumier. *Mol. Phys.*, 105:2857–2878, 2007.

[2] J. P. Beck, M.-P. Gaigeot, and J. M. Lisy. *Phys. Chem. Chem. Phys.*, 15:16736–16745, 2013.

[3] M.-P. Gaigeot and M. Sprik. *J. Phys. Chem. B*, 107:10344–10358, 2003.

[4] M. Sulpizi, M.P. Gaigeot, and M. Sprick. *J. Chem. Theory. Comput*, 8:1037–1047, 2012.

[5] Joyce Noah-Vanhoucke, Jared D. Smith, and Phillip L. Geissler. *The Journal of Physical Chemistry B*, 113(13):4065–4074, 2009.

[6] M. Sulpizi, M.P. Salanne, M. Gaigeot, and M. Sprick. *J. Phys. Chem. Lett*, 4:83, 2013.

[7] G.H. Peslherbe, H.Wang, and W.L. Hase. *J. Chem. Phys.*, 100:1179, 1993.

[8] X. Zhang, J.L. Rheinecker, and J.M. Bowman. *J. Chem. Phys.*, 122:114313, 2005.

[9] J.M. Bowman, B. Gazdy, and Q. Sun. *J. Chem. Phys.*, 91:2859–2862, 2003.

[10] W. Miller, W.L. Hase, and C. Darling. *J. Phys. Chem.*, 91:2863.

[11] Z. Xie and J.M. Bowman. *Chem. Phys. Lett.*, 429:355–359, 2006.

[12] D.L. Bunker. *Methods Comput Phys*, 10:287, 1971.

[13] D.L. Bunker and W.L. Hase. *J. Chem. Phys.*, 59:4621, 1973.

[14] J. Mikosch, S. Trippel, C. Eichhorn, R. Otto, U. Lourderaj, J. Zhang, W.L. Hase, M. Weidemuller, and R. Wester. *Science*, 319:183, 2008.

[15] D. Lu and W.L. Hase. *J. Phys. Chem*, 92:3217, 1988.

[16] D. Lu and W.L. Hase. *J. Phys. Chem*, 91:7490, 1989.

[17] J.S. Hutchinson, W.P. Reinhardt, and J.T. Hynes. *J. Chem. Phys.*, 79:4247, 1983.

[18] K.N. Swamy and W.L. Hase. *J. Chem. Phys.*, 82:123, 1985.

[19] G. Czakó and J.M. Bowman. *J. Chem. Phys.*, 131:244302, 2009.

[20] G. Czakó and J.M. Bowman. *Proc. Nat. Acad. Sciences*, 109:7997–8001, 2012.

[21] R. Liu, M. Yang, G. Czakó, J.M. Bowman, J. Li, and H. Guo. *J. Phys. Chem. Lett.*, 3:3776–3780, 2012.

[22] G. Czakó, R. Liu, M. Yang, J.M. Bowman, and H. Guo. *J. Phys. Chem.*, 139:6409–6420, 2013.

[23] N.M. Kidwell, H. Li, X. Whang, J.M. Bowman, and M.I. Lester. *Nature Chemistry*, 8:509–514, 2016.

[24] M. Born and R. Oppenheimer. *Ann. Physik*, 110:457, 1927.

[25] U. Manthe and H. Koppel. *J. Chem. Phys*, 93:1658, 1990.

[26] Dominik Marx and Jurg Hutter. *Ab Initio Molecular Dynamics - Basic theory and Advanced Methods*. Cambridge University Press, 2009.

[27] P. Hohenberg and W. Kohn. Inhomogeneous electron gas. *Phys. Rev.*, 136(3B):864–871, 1964.

[28] W. Kohn and L.K Sham. Self-consistent equations including exchange and correlation effects. *Phys. Rev.*, 140(4A):1133–1138, 1965.

[29] A.D. Becke. Density-functional exchange-energy approximation with correct asymptotic behavior. *Phys. Rev. A*, 38(6):3098–3100, 1988.

[30] C. Lee, W. Yang, and R.G. Parr. Development of the Colle-Salvetti correlation-energy formula into a functional of the electron density. *Phys. Rev. B*, 37(2):785–789, 1988.

[31] S. Grimme, J. Antony, S. Ehrlich, and H. Krieg. *J. Chem. Phys.*, 132:154104, 2010.

[32] Stefan Grimme. *J. Comput. Chem.*, 27(15):1787–1799, 2006.

[33] Stefan Grimme. *WIREs Comput. Mol. Sci.*, 1:211–228, 2011.

[34] Stefan Grimme, J. Antony, S. Ehrlich, and H. Krieg. *J. Chem. Phys.*, 132:154104, 2010.

[35] H. Hellmann. *EinfÂ¨uhrung in die Quantenchemie (Deuticke, Leipzig, Germany).*

[36] R. P. Feynman. *Phys. Rev.*, 56:340, 1939.

[37] Cp2k developers group. http://cp2k.berlios.de/, 2015.

[38] The CPMD consortium. CPMD version 3.13.2.

[39] Joost VandeVondele, Urban Borstnik, and Jurg Hutter. *Journal of Chemical Theory and Computation*, 8(10):3565–3573, 2012.

[40] Joost VandeVondele, Matthias Krack, Fawzi Mohamed, Michele Parrinello, Thomas Chassaing, and Jurg Hutter. *Comput. Phys. Comm.*, 167(2):103 – 128, 2005.

[41] S. Goedecker, M. Teter, and J. Hutter. *Phys. Rev. B*, 54:1703–1710, Jul 1996.

[42] C. Hartwigsen, S. Goedecker, and J. Hutter. *Phys. Rev. B*, 58:3641, 1998.

[43] Joost VandeVondele and Jurg Hutter. *J. Chem. Phys.*, 127(11):114105–114113, 2007.

[44] Glenn J. Martyna, Michael L. Klein, and Mark Tuckerman. *The Journal of Chemical Physics*, 97(4):2635–2643, 1992.

[45] E. Wigner. *Phys. Rev*, 40:749, 1932.

[46] L. Sun and W.L. Hase. *J. Chem. Phys.*, 133, 2010.

[47] M. Shmilovits-Ofir and R.B. Gerber. *J. Am. Chem. Soc.*, 133:16510.

[48] G.H. Peslherbe, H.Wang, and W.L. Hase. *Monte Carlo Methods in Chemical Physcis.* Wiley Sons, 1999.

[49] A. Bastida, M.A. Soler, J. Zuniga, A. Requena, A. Kalstein, and S. Fernandez-Alberti. *J. Chem. Phys*, 132:224501, 2010.

[50] A. Kalstein, S. Fernandez-Alberti, A. Bastida, M.A. Soler, M.H. Farag, J. Zuniga, and A. Requena. *Theor. Chem. Acc*, 128:769–782, 2011.

[51] M.H. Farag, A. Bastida, M.F. Ruiz-López, G. Monard, and F. Ingrosso. *J. Chem. Phys. B.*, 118:6186–6197, 2014.

[52] D. McQuarrie. *Statistical mechanicals.* Harper-Collins Publishers, 1976.

[53] R. Kubo, M. Teda, and N. Hashitsume. *Statistical physics II-nonequilibrium statistical mechanics 2 edn.* Springer Heideberg, 1985.

[54] R. Iftimie and M. Tuckerman. *J. Chem. Phys.*, 122:214508, 2005.

[55] H. Ahlborn, B. Space, and P. B. Moore. *J. Chem. Phys.*, 112.

[56] J. Borysow, M. Moraldi, and L. Frommhold. *Mol. Phys.*, 56, 1985.

[57] R. Ramirez, T. Lopez-Ciudad, P. Kumar, and D. Marx. *J. Chem. Phys*, 121:3973, 2004.

[58] C.P. Lawrence and J.L. Skinner. *Proc. Nat. Acad. Sci.*, 102:6720, 2005.

[59] H. Kim and P.J. Rossky. *J. Chem. Phys*, 125:074107, 2006.

[60] C. Marinica, G. Grégoire, C. Desfrancois, J.-P. Schermann, D. Borgis, and M.-P. Gaigeot. *J. Chem. Phys. A*, 110:8802–8810, 2006.

[61] A. Cimas, T.D. Vaden, TSJA. De Boer, L.C. Snoek, and M.-P. Gaigeot. *J. Chem. Theory Comput*, 5:1068, 2009.

[62] A. Sediki, L. C. Snoek, and M.-P. Gaigeot. *Int. J. Mass Spectrom.*, 308:281–288, 2011.

[63] Bovi. D, Mezzetti. A, R. Vuilleumier, M.-P. Gaigeot, B. Chazallon, R. Spezia, and L. Guidoni. *Phys. Chem. Chem. Phys*, 13:20954, 2011.

[64] M.-P. Gaigeot, M. Sprik, and M. Sulpizi. *J. Phys. Condens. Matter*, 24:124106, 2012.

[65] M. Martinez, M.-P. Gaigeot, D. Borgis, and R. Vuilleumier. *J. Chem. Phys*, 125:144106, 2006.

[66] M. Nonella, G. Mathias, and P. Tavan. *J. Phys. Chem. A*, 107:8638, 2003.

[67] G. Mathias, S.D. Ivanov, A. Witt, M.D. Baer, and D. Marx. *J. Chem. Theory Comput*, 8:224, 2012.

[68] J.B. Huff, B. Askew, R.J. Duff, and J. Rebek. *J. Am. Chem. Soc.*, 110:5908, 1988.

[69] B.M Tadayoni, K. Parris, and J. Rebek. *J. Am. Chem. Soc.*, 111:4503, 1989.

[70] T.A. Montzka, S. Swaminathan, and R.A. Firestone. *J. Phys. Chem*, 98:13171, 1994.

[71] C.R. Cantor and P.R. Schimmel. *Biophysical chemistry*. W.H. Freeman: San Francisco, 1980.

[72] S.Y Liu, D.M. Mehringer, and L.E. Snyder. *Astrophys. J.*, 552:654, 2001.

[73] D.M. Mehringer, L.E. Snyder, and Y.T. Miao. *Astrophys. J.*, 480:71, 1997.

[74] L.E. Snyder, F.J. Lovas, J.M. Hollis, D.N. Friedel, P.R. Jewell, A. Remijan, V.V. Ilyushin, E.A. Alekseev, and S.F. Dyubko. *Astrophys. J.*, 619:914, 2005.

[75] M. Pettersson, J. Lundell, L. Khriachtchev, and M. Rasanen. 119:11715, 1997.

[76] E.M.S. Macoas, L. Khriachtchev, R. Fausto, and M. Rasanen. 108:3380, 2004.

[77] K. Marushkievich, L. Khriachtchev, and M. Rasanen. 126:241102, 2007.

[78] A. Sharma, I. Reva, and R. Fausto. 131:8752, 2009.

[79] J. Nieminem, M. Rasanen, and J. Murto. *J. Phys. Chem.*, 96:5303, 1992.

[80] I.D. Reva, S.G Stepanian, L. Adamowicz, and R. Fausto. *J. Phys. Chem. A*, 105:4773, 2001.

[81] E.M.S. Macoas, R. Fausto, J. Lundell, M. Petterson, L. Khriachtchev, and M. Rasanen. *J. Phys. Chem. A*, 104:11725, 2000.

[82] E.M.S. Macoas, R. Fausto, J. Lundell, M. Petterson, L. Khriachtchev, and M. Rasanen. *J. Phys. Chem. A*, 105:3922, 2001.

[83] E.M.S. Macoas, R. Fausto, M. Petterson, L. Khriachtchev, and M. Rasanen. *J. Phys. Chem. A*, 104:6956, 2000.

[84] K.B. Wiberg and K.E. Laidig. *J. Am. Chem. Soc.*, 109:5935, 1987.

[85] J.J.C Teixeira-Dias and R. Fausto. *J. Mol. Struct.*, 144:199, 1986.

[86] J.H. Lii. *J. Phys. Chem. A.*, 106:8667, 2002.

[87] N.L. Allinger and S.H.M. Chang. *Tetrahedron*, 33:1561, 1977.

[88] J.D. Goddard, Y. Yamaguchi, and H.F. Schaefer. *J. Chem. Phys.*, 96:1158, 1992.

[89] M.L. Senent. *Mol. Phys.*, 99:1311, 2001.

[90] I. Hisatsun and J. Heicklen. *Can. J. Spectrosc.*, 18:135, 1973.

[91] W.H. Hocking. *Z Naturforsch A*, 31:1113, 1976.

[92] E. Bjarnov and W.H. Hocking. *Z Naturforsch A*, 33:610, 1978.

[93] E. Whittle, D.A. Dows, and G.C. Pimentel. 22:1943, 1954.

[94] R. Fausto. *Low temperature molecular spectroscopy.* Kluwer Academic Publishers, Dordrecht, 1996.

[95] L. Andrews and M. Moskovits. *Chemistry and physics of matrix-isolated species.* Elsevier Science Pub. Co., Amsterdam, 1989.

[96] R.N. Perutz. *Chem. Rev*, 85:77, 1985.

[97] A.J. Barnes. *J. Mol. Struct*, 113:161, 1984.

[98] M. Tasumi and M. Nakata. *J. Mol. Struct*, 126:111, 1985.

[99] M.J. Almond. *Annu. Rep. Prog. Chem. Sec. C*, 93:3, 1997.

[100] P. Klaeboe and C.J. Nielsen. *Analyst*, 117:335, 1992.

[101] I.R. Dunkin. *Matrix-Isolation Techniques: A Pratical Approach.* Oxford University Press, Oxford, 1998.

[102] L. Khriachtchev, J. Lundell, E. Isoniemi, and M. Rasanen. *J. Chem. Phys*, 113:4265, 2000.

[103] C. Crépin, P. de Pujo, B. Bouvier, V. Brenner, and Ph. Millié. *Chem. Phys.*, 272:243–258, 2001.

[104] E.M.S. Macoas, L. Khriachtchev, M. Petterson, J. Juselius, R. Fausto, and M. Rasanen. *J. Chem. Phys*, 119:11765–11772, 2003.

[105] O. A. Vydrov and T. V. Voorhis. *J. Chem. Phys*, 133, 2010.

[106] F.A. Lindemann. *Physik. Z*, 11:609–612, 1910.

[107] Y. Zhou, D. Vitkup, and M. Karplus. *J. Mol. Biol.*, 285:1371–1375, 1999.

[108] J.H. Bilgram. *Phys. Rep.*, 153:1–89, 1987.

[109] H. Lowen. *Phys. Rep.*, 237:249–324, 1994.

[110] J.E. Bertie and K.H. Michaelian. *J. Chem. Phys*, 76:886, 1982.

[111] J. Lemaire, P. Boissel, M. Heninger, G. Mauclaire, G. Bellec, H. Mestdagh, A. Simon, S. Le Caer, J.M. Ortega, F. Glotin, and P. Maitre. *Phys. Rev. Lett.*, 89:273002.

[112] J. Oomens, B.G. Sartakov, G. Meijer, and G. Von Helden. *Int. J. Mass Spectrom.*, 254:1.

[113] V. Brites, A. Cimas, R. Spezia, N. Sieffert, J.M. Lisy, and M-P. Gaigeot. *J. Chem. Theory Comput.*, 11:871.

[114] A. Olbert-Majkut, J. Lundell, and M. Wierzejewska. 118:350, 2014.

ACKNOWLEDGEMENTS

A l'issue de la rédaction de ce manuscrit, je suis convaincu que la thèse est loin d'être un travail solitaire. Je n'aurais jamais pu réaliser ce travail doctoral sans le soutien de grand nombre de personnes dont la générosité, la bonne humeur m'ont permis de progresser dans ma vie de jeune chercheur.

En premier lieu, je tiens à remercier ma directrice de thèse, madame Marie-Pierre Gaigeot, et de mon co-directeur de thèse, monsieur Riccardo Spezia, pour la confiance qu'ils m'ont accordé en acceptant d'encadrer cette thèse, pour leurs multiples conseils et pour toutes les heures consacrées. De plus, je suis impressionné par leur patience à mon égard depuis mon premier stage ici en 2008… (Et oui.. déjà).

Ensuite, je souhaite remercier les personnes qui m'ont bien accueillies au laboratoire et grâce auxquelles j'ai trouvé ces quatre années agréables : Basil, Fausto (tous les deux partis trop tôt), Ana, Alvaro, Vincent, Marco et tous les italiens, Jean-Philippe et Morgane qui m'a rendu plus pieux. Sans oublier les meilleurs pour la fin : Yannick et Jéjé, qui représentent dignement le groupe culinaire des Mardi midi. En énumérant cela je n'oublie pas le personnel de la cantine qui m'a toujours généreusement servi.

Je souhaite aussi remercier mes collaborateurs étrangers le Professeur Jim Lisy ainsi que Haochen qui m'ont très bien accueilli à Urbana Champaign et m'ont fait découvrir les joies des expériences.

Je souhaite également remercier les autres personnes du LAMBE qui m'ont aidé pour mon année d'ATER ou autre : Manue, Caroline, William, sans oublier Ketty.

Je souhaite remercier le RER D, qui a été mon grand allié pendant ces 4 années et avec qui j'ai passé beaucoup de temps (et de sueur…)

D'un point de vue plus personnel, je souhaiterais remercier mes 3 amis « fantastiques » : Elie Le Viet, Payraud le Fou et Francky la Flèche ainsi que toute la PDF-family qui m'ont permis de passer des moments inoubliables pendant toutes ces années.

Enfin, et bien évidemment, je souhaiterai remercier mes parents qui m'ont toujours soutenu au cours de ma vie et particulièrement pendant cette thèse. Car, oui, être un « Tanguy » ça a aussi ses avantages quand la bonne humeur et la bonne entente est de mise. Même si les mots « barbares » de mon titre de thèse les faisaient souvent rire, ils m'ont toujours encouragé à continuer et à travailler le mieux que je pouvais.

Titre : Excitation vibrationnelle de molécules en phase gazeuse et en insérées en matrices par simulations de dynamiques moléculaires *ab initio.*

Mots clés : Excitation Vibrationnelle ; dynamique moléculaire *ab initio* ; DFT ; matrices ; nombre quantique vibrationnel

Résumé : Dans cette thèse nous avons travaillé sur deux systèmes prototypiques: en phase gazeuse et en phase condensée, pour suivre et quantifier l'énergie vibrationnelle dans des modes normaux après excitation vibrationnelle initiale. Pour la phase condensée, ce travail prend en compte l'immersion d'une molécule hôte: l'acide formique immergé dans une matrice d'argon et pour la phase gazeuse avec un cluster de (Cl ... N-Methyl Acétamide..Ar).
Après la préparation des conditions initiales utilisant un échantillonnage semi-classique de Wigner, plusieurs trajectoires DFT-MD ont été exécutées pour analyser la relaxation vibrationnelle intra et intermoléculaire. Deux méthodes théoriques ont été utilisées pour suivre l'évolution avec le temps du nombre quantique vibrationnel: une nouvelle méthode basée sur l'étude des spectres d'état vibrationnels (VDOS) comparé avec une méthode plus traditionnelle basée sur l'étude de l'amplitude d'un mouvement spécifique de la molécule (c'est-à-dire distance ou angle).
Dans la phase condensée, le rendement quantique du processus d'isomérisation de la molécule d'acide formique a été comparé aux données expérimentales. Nous avons montré que l'excitation vibrationnelle combinée de deux modes implique dans quelques cas l'isomérisation de la molécule d'acide formique. Cette excitation vibrationnelle initiale de l'acide formique a aussi un impact sur la matrice environnante: l'énergie initialement contenue dans l'AF est redistribuée à la matrice, ce qui mène à la déformation et la fonte (transition solide-liquide) de la matrice d'argon. En ce qui concerne la phase gazeuse, nous avons montré que l'excitation vibrationnelle de l'étirement du mouvement N-H du (Cl... NMA) implique la perte (évaporation) systématique de l'atome d'argon. Finalement, les deux modèles (phase gaz ou condensée) ont montré qu'après une excitation vibrationnelle initiale (n=1) d'un mode normal à t=0 de la dynamique, ce mode normal revient au cours de la dynamique dans son état fondamental (n=0).

Title : Vibrational exciation of molecules in the gas phase or embedded in matrices by *ab initio* molecular dynamics.

Key words: Vibrational excitation ; ab initio molecular dynamics ; DFT ; matrices ; vibrational quantum number

Abstract : In the thesis we have studied two prototypical systems in both condensed and gas phase, to follow and quantify the vibrational energy flow through normal modes after vibrational excitation. For the condensed phase, we considered a host Formic Acid immersed in an argon matrix, while for the gas phase we have studied the N-Methyl Acetamid... Cl.. Ar cluster. After the preparation of initial conditions using a semi-classical Wigner sampling, several DFT-MD trajectories have been performed to analyse the Intra/Inter vibrational energy relaxation. Two theoretical methods have been used to follow the evolution with time of the vibrational quantum
In the condensed phase, the quantum yield of the trans/cis isomerisation process of the Formic Acid molecule has been compared to the experimental data. We have shown that the vibrational excitation of two combination modes involves in some cases the isomerisation of the Formic Acid molecule. This initial vibrational excitation of the Formic Acid has also an impact on the surrounding matrix: the energy initially contained into the FA is redistributed to the matrix leading to the deformation and the melting (solid-liquid transition) of the argon matrix. In the gas phase, we have shown that

numbers: a new method based on the study of vibrational density of states (VDOS) compared with a more traditional method based on the study of the amplitude of a specific motion of the molecule (i.e. distance or angle). Both methods reveal similar results.

vibrational excitation of the N-H stretching motion of the (Cl...NMA) involves the systematic loss of the argon atom. Finally, the two models have shown that in both condensed or gas phase environment, after the vibrational excitation (n=1) of a normal mode at t=0 of the dynamics, this normal mode comes back in its ground state (n=0).